Functional oxide thin films for micromechanical and bioelectronic devices

Dissertation
der Mathematisch-Naturwissenschaftlichen Fakultät
der Eberhard Karls Universität Tübingen
zur Erlangung des Grades eines
Doktors der Naturwissenschaften
(Dr. rer. nat.)

vorgelegt von
Maximilian Thomas Becker
aus Tübingen

Tübingen
2021

Gedruckt mit Genehmigung der Mathematisch-Naturwissenschaftlichen Fakultät der Eberhard Karls Universität Tübingen.

Tag der mündl. Qualifikation:	20.07.2021
Dekan:	Prof. Dr. Thilo Stehle
1. Berichterstatter:	Prof. Dr. Dieter Kölle
2. Berichterstatter:	Prof. Dr. Günther Zeck

Abstract

The present cumulative thesis discusses the challenging and exciting way to utilize the outstanding physical properties of functional oxide materials for the development of new applications and devices, with a focus on the integration of lead-free ferroelectric thin films into bioelectronics. The cumulative thesis comprises four publications – Publication I - IV – and is organized as follows.

The first part (Publication I + II) is devoted to the pulsed laser deposition (PLD) of lead-free $0.5(Ba_{0.7}Ca_{0.3})TiO_3$-$0.5Ba(Zr_{0.2}Ti_{0.8})O_3$ (BCZT) ferroelectric thin films on different substrates and their detailed electrical characterization and analysis by impedance spectroscopy. For the deconvolution of measured impedance spectra by equivalent-circuit fitting, a new equivalent-circuit element based on the theory of interface pinning in random systems – the domain wall pinning element – is introduced which models the impedance of a ferroelectric including the contribution from domain-wall-motion in the subswitching regime. This approach is applied to impedance spectra collected on polycrystalline and epitaxial BCZT thin film capacitor stacks, and the domain-wall-motion induced field- and frequency-dependent dielectric response of the BCZT films is extracted by domain wall pinning element modeling and equivalent-circuit fitting. Moreover, an extended Rayleigh analysis is presented which allows one to quantify the coupling strength between dielectric nonlinearity and frequency dispersion and the identification of different domain-wall-motion regimes in the BCZT films. The corresponding domain-wall dynamics in the BCZT thin films is discussed in detail and a schematic diagram of the different domain-wall-motion regimes is presented. The results from the extended Rayleigh analysis – obtained on epitaxial and polycrystalline BCZT films – indicate, that the presence of grain boundaries in BCZT reduces the coupling strength between dielectric nonlinearity and frequency dispersion and suppresses the motion of internal domain-wall segments in addition to the suppression of the irreversible center-of-mass motion of the domain walls.

In the second part (Publication III), microelectrodes based on conductive sputtered IrO_2 films (SIROFs) – which are utilized to provide electro–neural interfaces for subretinal stimulation in the state-of-the-art retinal prosthesis "Retina Implant Alpha AMS" – are analyzed in detail by electrochemical impedance spectroscopy (EIS) and subsequent equivalent-circuit analysis. The supercapacitive behavior of the investigated SIROF-microelectrodes is modeled by a pseudocapacitance C_p in parallel to the capacitance of the electrochemical double layer C_DL, and both capacitances are represented by a constant phase element (CPE) in the equivalent-circuit model. By fitting

the measured EIS data with the equivalent-circuit model, C_{p} and C_{DL} are quantified from the obtained CPE fit parameters, and the resulting supercapacitive behavior is in agreement with cyclic voltammetry measurements. The results indicate, that the pseudocapacitance C_{p} due to quasi-continuous reversible reduction and oxidation between Ir^{3+}/ Ir^{4+} valence states is the dominant contribution to the supercapacitance and to the charge injection capacity (CIC) of the investigated SIROF-microelectrodes.

Finally, in the third part (Publication IV), a new approach for bioelectronic interfacing of electrogenic cells or tissue is introduced, which utilizes a conductive microelectrode coated with an insulating ferroelectric layer for extracellular electrical stimulation. It is shown, that the ferroelectric polarization current contributes to the extracellular stimulation current provided by the ferroelectric microelectrode. The switching regime of a ferroelectric microelectrode in an electrolyte–ferroelectric–conductor configuration is analyzed based on the traditional Kolmogorov-Avrami-Ishibashi (KAI)-model and the time-dependent stimulation current in response to an applied voltage step is simulated for a generic microelectrode geometry. It is shown that, depending on the remanent polarization P_{r} of the utilized ferroelectric, the polarization current in the switching regime can increase the CIC by up to two orders of magnitude as compared to the commonly used extracellular capacitive stimulation with microelectrodes coated with an insulating dielectric layer. The results pave the way for extracellular electrical stimulation with small microelectrodes ($\sim 30\ \mu$m in diameter) without toxic electrochemical effects, which is crucial for implantable neuroprosthetic devices such as high-resolution retinal-implants or brain-machine interfaces.

Kurzfassung

Die vorliegende kumulative Dissertation diskutiert den herausfordernden und spannenden Weg, die herausragenden physikalischen Eigenschaften von funktionalen Oxidmaterialien für die Entwicklung neuer Anwendungen und Bauelemente zu nutzen, wobei der Schwerpunkt die Integration von bleifreien ferroelektrischen Dünnschichten in die Bioelektronik bildet. Die kumulative Dissertation umfasst vier Publikationen – Publikation I - IV – und ist wie folgt gegliedert.

Der erste Teil (Publikation I + II) widmet sich der gepulsten Laserablation (PLD) von bleifreien $0.5(Ba_{0.7}Ca_{0.3})TiO_3$-$0.5Ba(Zr_{0.2}Ti_{0.8})O_3$ (BCZT) ferroelektrischen Dünnschichten auf verschiedenen Substraten und ihrer detaillierten elektrischen Charakterisierung und Analyse mittels Impedanzspektroskopie. Für die Entfaltung der gemessenen Impedanzspektren durch fitten der Daten mit einem Ersatzschaltkreis-Modell wird ein neues Ersatzschaltbild-Element – das Domänenwand-Pinning-Element – eingeführt, welches auf der Theorie des Grenzflächen-Pinnings in zufälligen Systemen basiert und das die Impedanz eines Ferroelektrikums einschließlich des Beitrags der Domänenwand-Bewegung im "Sub-Switching"-Regime modelliert. Dieser Ansatz wird auf Impedanzspektren angewandt, welche an polykristallinen und epitaktischen BCZT-Dünnschicht-Kondensatoren gemessen wurden, und die durch Domänenwand-Bewegung induzierte feld- und frequenzabhängige dielektrische Antwort der BCZT-Filme wird durch Domänenwand-Pinning-Element-Modellierung und fitten der Daten mit einem Ersatzschaltkreis-Modell extrahiert. Darüber hinaus wird eine erweiterte Rayleigh-Analyse vorgestellt, welche es erlaubt, die Kopplungsstärke zwischen dielektrischer Nichtlinearität und Frequenzdispersion zu quantifizieren und unterschiedliche Regimes der Domänenwandbewegung in den BCZT-Filmen zu identifizieren. Die entsprechende Domänenwand-Dynamik in den BCZT-Dünnschichten wird detailliert diskutiert und ein schematisches Diagramm der unterschiedlichen Regimes der Domänenwandbewegung wird vorgestellt. Die Ergebnisse der erweiterten Rayleigh-Analyse, welche an epitaktischen und polykristallinen BCZT-Filmen gewonnen wurden, zeigen, dass das Vorhandensein von Korngrenzen in BCZT die Kopplungsstärke zwischen dielektrischer Nichtlinearität und Frequenzdispersion reduziert und die Bewegung der internen Domänenwandsegmente unterdrückt, wobei ebenfalls die irreversible Schwerpunktsbewegung der Domänenwände unterdrückt ist.

Im zweiten Teil (Publikation III) werden Mikroelektroden auf der Basis von leitfähigen gesputterten IrO_2-Filmen (SIROFs) - die als elektro-neurale Schnittstellen für die subretinale Stimulation in der modernen Netzhautprothese "Retina Implant Alpha AMS" eingesetzt werden - mittels elektroche-

mischer Impedanzspektroskopie (EIS) und anschließendem fitten der Daten mit einem Ersatzschaltkreis-Modell detailliert analysiert. Das superkapazitive Verhalten der untersuchten SIROF-Mikroelektroden wird durch eine Pseudokapazität C_p parallel zur Kapazität der elektrochemischen Doppelschicht C_DL modelliert, und beide Kapazitäten werden durch ein Constant phase element (CPE) im Ersatzschaltbild dargestellt. Durch fitten der gemessenen EIS-Daten mit dem Ersatzschaltbild-Modell werden C_p und C_DL aus den erhaltenen CPE-Fit-Parametern quantifiziert, und das resultierende superkapazitive Verhalten ist in Übereinstimmung mit zyklischen Voltammetrie Messungen. Die Ergebnisse zeigen, dass die Pseudokapazität C_p aufgrund quasi-kontinuierlicher reversibler Reduktion und Oxidation zwischen Ir^{3+}/ Ir^{4+}-Valenzzuständen den dominanten Beitrag zur Superkapazität und zur Ladungsinjektionskapazität (CIC) der untersuchten SIROF-Mikroelektroden darstellt.

Im dritten Teil (Publikation IV) wird schließlich ein neuer Ansatz für die bioelektronische Kopplung elektrogener Zellen oder Gewebe vorgestellt, bei dem eine leitfähige Mikroelektrode, welche mit einer isolierenden ferroelektrischen Schicht beschichtet ist, zur extrazellulären elektrischen Stimulation verwendet wird. Es wird gezeigt, dass der ferroelektrische Polarisationsstrom zum extrazellulären Stimulationsstrom beiträgt, welcher von der ferroelektrischen Mikroelektrode generiert wird. Das Schaltverhalten einer ferroelektrischen Mikroelektrode in einer Elektrolyt-Ferroelektrikum-Leiter-Konfiguration wird auf der Grundlage des traditionellen Kolmogorov-Avrami-Ishibashi (KAI)-Modells analysiert, und der zeitabhängige Stimulationsstrom als Reaktion auf eine angelegte Spannungsstufe wird für eine generische Mikroelektroden-Geometrie simuliert. Es wird gezeigt, dass in Abhängigkeit von der remanenten Polarisation P_r des verwendeten Ferroelektrikums, der Polarisationsstrom beim Umschalten der ferroelektrischen Polarisation, die CIC um bis zu zwei Größenordnungen im Vergleich zur üblicherweise verwendeten extrazellulären kapazitiven Stimulation mit Mikroelektroden, welche mit einer isolierenden dielektrischen Schicht beschichtet sind, erhöhen kann. Die Ergebnisse ebnen den Weg für die extrazelluläre elektrische Stimulation mit kleinen Mikroelektroden ($\sim 30\ \mu$m im Durchmesser) ohne schädliche elektrochemische Effekte, was für implantierbare Neuroprothesen wie hochauflösende Retina-Implantate oder Gehirn-Maschine-Schnittstellen äußerst wichtig ist.

Contents

List of publications ix

List of abbreviations xi

1 Introduction 1

1.1 Motivation . . . 1

1.2 Functional oxide materials . . . 5

1.2.1 Lead-free ferroelectrics . . . 5

1.2.2 Conductive oxides for electro–neural interfaces . . . 8

2 Summary of publications and contributions 11

2.1 Publication I . . . 11

2.2 Publication II . . . 17

2.3 Publication III . . . 21

2.4 Publication IV . . . 24

3 Summary and outlook 27

Bibliography 31

Appended publications 37

List of publications

Appended publications

Publication I

M. Becker, C. J. Burkhardt, R. Kleiner, and D. Koelle
"Impedance spectroscopy of ferroelectrics: The domain wall pinning element"
arXiv:2008.04786v2 [cond-mat.mtrl-sci] (2021)

Publication II

M. Becker, C. J. Burkhardt, B. Schröppel, R. Kleiner, and D. Koelle
"Rayleigh analysis and dielectric dispersion in polycrystalline $0.5(Ba_{0.7}Ca_{0.3})TiO_3$–$0.5Ba(Zr_{0.2}Ti_{0.8})O_3$ ferroelectric thin films by domain-wall pinning element modeling"
J. Appl. Phys. **128**, 154103 (2020)

Publication III

J. Haas, R. Rudorf, **M. Becker**, R. Daschner, A. Drzyzga, C. Burkhardt, and A. Stett
"Sputtered Iridium Oxide as Electrode Material for Subretinal Stimulation"
Sens. Mater. **32**, 2903 (2020)

Publication IV

Maximilian T. Becker
"Charge injection capacity of ferroelectric microelectrodes for bioelectronic applications"
AIP Advances **11**, 065106 (2021)

Publications not included in this thesis

Publication V

B. Müller, M. Karrer, F. Limberger, **M. Becker**, B. Schröppel, C. J. Burkhardt, R. Kleiner, E. Goldobin, and D. Koelle
"Josephson Junctions and SQUIDs Created by Focused Helium-Ion-Beam Irradiation of $YBa_2Cu_3O_7$"
Phys. Rev. Applied **11**, 044082 (2019)

Publication VI

O. Salomon, W. Hempel, O. Kiowski, E. Lotter, W. Witte, A. Ferati, A. Schneikart, G. Kaune, R. Schäffler, **M. Becker**, B. Schröppel, R. V. Lorbada, D. Mücke, and T. Walter
"Influence of Molybdenum Back Contact on the PID Effect for Cu(In,Ga)Se_2 Solar Cells"
Coatings **9**, 794 (2019)

Publication VII (Patent application)

M. Becker and C. J. Burkhardt
"Piezoelektrisches Membran-Mikroelektroden Array"
Submitted to Deutsches Patent- und Markenamt DPMA (2020)
Reference number: 10 2020 126 759.2
Inventor share: 90 %

Publication VIII (Patent application)

M. Becker and C. J. Burkhardt
"Ferroelektrischer Biochip"
Submitted to Deutsches Patent- und Markenamt DPMA (2020)
Reference number: 10 2020 132 756.0
Inventor share: 90 %

List of abbreviations

BCZT $0.5(Ba_{0.7}Ca_{0.3})TiO_3$-$0.5Ba(Zr_{0.2}Ti_{0.8})O_3$

CIC Charge injection capacitiy

CMOS Complementary metal-oxide-semiconductor

CPE Constant phase element

CV Cyclic voltammetry

EIS Electrochemical impedance spectroscopy

FeFET Ferroelectric field-effect transistor

MOSFET Metal-oxide-semiconductor field-effect transistor

PLD Pulsed laser deposition

SIROFs Sputtered IrO_2 films

STEM Scanning transmission electron microscopy

XRD X-ray diffraction

Chapter 1

Introduction

1.1 Motivation

The invention of the transistor goes back to Julius Edgar Lilienfeld, who formulated the basic concept in 1925 (US patent granted in 1930 [1]). In 1947, the first working transistor was built by John Bardeen, Walter Brattain and William Shockley at Bell Laboratories, for which they were awarded with the Nobel prize in physics in 1956. Three years later, the metal-oxide-semiconductor field-effect transistor (MOSFET) was invented, which made it possible to fabricate high density integrated circuits (ICs). The industrial production of ICs – for example by complementary metal-oxide-semiconductor (CMOS) technology – revolutionized the world economy and marked the onset of the information age with the daily use of personal computers, smartphones and the internet. The rapid technical development within the information age is accompanied by Moore's law, which states that the number of transistors on ICs doubles every two years[2, 3].

However, novel devices such as electrical active neuroprostheses, biosensors, nanogenerators and other microelectromechanical systems (MEMS) are characterized by new functionalities, which cannot be achieved by simply integrating more transisors on a chip. Explicit examples are high-resolution retinal implants [4, 5], brain-machine interfaces [6], wearable sensor arrays for *in situ* perspiration analysis [7] or piezolectric nanoribbons for monitoring cellular deformations [8]. Since the functionalities of such devices do not necessarily scale according to Moore's law, they are categorized by the term "more than Moore", which corresponds to a paradigm shift in the semiconductor industry: Rather than making the chips better and letting the applications follow, it will start with applications and work downwards to see what chips are needed to support them [9].

A possibility to create new applications and/or devices with new functionalities in the sense of a more than Moore strategy, is to utilize the physical effects occurring in the wide class of functional oxide materials, e.g., ferroelectricity, piezoelectricity, superconductivity and magnetism. In this thesis, the main focus will be on functional oxides with ferroelectric properties and their integration into (novel) micromechanical and bioelectronic devices. Here, the successful integration of ferroelectric oxides often requires the fabrication of high-quality thin films with tailored properties and thicknesses down to $\sim$ 5 nm, e.g., by (advanced) pulsed laser deposition (PLD) [10]. This is a challenging task, since the physical properties of ferroelectric thin films are influenced by strain, defects, chemical composition and crystallographic orientation, which need to be controlled by the thin film deposition parameters. Therefore, in order to optimize the physical properties of ferroelectric thin films for their specific target application, it is necessary to establish a link between deposition parameters and film properties.

A key material property of ferroelectric films is their dielectric response, and the real and imaginary parts of complex relative permittivity $\varepsilon_r = \varepsilon_r' - i\varepsilon_r''$ are included in various existing figures of merit (FOMs) for MEMS and (bio-) sensor applications which act as a benchmark for device performance. For example, the corresponding FOM for thin film energy harvesting devices contains ε_r' and is given by [11, 12]

$$\mathrm{FOM}_{\mathrm{EH}} = \frac{e_{31,\mathrm{f}}^2}{\varepsilon_0 \varepsilon_r'} \quad , \tag{1.1}$$

where $e_{31,\mathrm{f}}$ denotes the effective transversal piezoelectric coefficient and ε_0 the vacuum permittivity. Moreover, the FOM for the intrinsic signal-to-noise ratio of piezoelectric sensors

$$\mathrm{FOM}_{\mathrm{SNR}} = \frac{e_{31,\mathrm{f}}}{\sqrt{\varepsilon_0 \varepsilon_r''}} \quad , \tag{1.2}$$

includes the imaginary part ε_r'' of the complex relative permittivity [11]. Additionally, the dielectric loss $\tan\delta = \varepsilon_r''/\varepsilon_r'$ is a central material property for energy storage applications based on thin film relaxor-ferroelectrics. [13].

In general, the complex dynamics of domain wall displacement in ferroelectrics at subswitching conditions results in a dependence of the complex permittivity on the amplitude E_0 and frequency f of an applied ac electric field [14, 15]. Thus, the knowledge of the dielectric response $\varepsilon_r(E_0, f)$ of ferroelectric films is crucial for device modeling and FOM enhancements, which is especially true for lead-free $BaTiO_3$-based ferroelectrics, which are promising alternative materials to replace $PbZr_xTi_{1-x}O_3$ (PZT) in MEMS devices;

however their FOMs for various MEMS applications are still inferior to the corresponding FOMs for PZT thin films [16].

In thin film devices containing a ferroelectric placed between two metallic electrodes, the dielectric properties can exhibit strong frequency dispersion depending on the resistivity of both, the ferroelectric film and the electrode layers [17], thus masking the true dielectric dispersion of the ferroelectric. The latter is caused by pinning of domain walls on randomly distributed defects occuring in the ferroelectric layer inside the heterostructure [18, 19]. Moreover, the interfaces to the electrodes play a more crucial role in thin films as compared to thick ceramic samples [20, 21], i.e., interfaces can lead to extrinsic dielectric relaxation processes [22], additionally masking the contributions from the ferroelectric.

In this thesis, a new equivalent-circuit element with impedance Z_{DW} will be introduced, which is based on the theory of interface pinning in random systems [18] and models the frequency-dependent impedance response of a ferroelectric including the domain-wall-motion induced contribution. Moreover, a method to extract the domain-wall-motion induced amplitude- and frequency-dependent dielectric response $\varepsilon_r(E_0, f)$ in thin film ferroelectrics from impedance spectroscopy measurements is presented. Additionally, an extended Rayleigh analysis will be introduced, which allows one to quantify the coupling strength between dielectric nonlinearity and frequency dispersion and to identify different domain-wall-motion regimes in ferroelectrics. The method is demonstrated by applying it to thin film capacitor stacks containing the lead-free ferroelectric $0.5(Ba_{0.7}Ca_{0.3})TiO_3$–$0.5Ba(Zr_{0.2}Ti_{0.8})O_3$ (BCZT) [23], which is a promising candidate to replace the (toxic) standard material $PbZr_xTi_{1-x}O_3$ (PZT) in MEMS and biosensor applications.

Another class of functional oxide materials investigated in this work are conductive IrO_2 thin films, which are high-end electrode materials to provide electro–neural interfaces for extracellular electrical stimulation and recording , e.g., in neuroprosthetic devices. Here, microelectrodes are required to provide a high charge injection capacity (CIC) for efficient extracellular electrical stimulation. Thus, the knowledge of different charge injection mechanism and their relative contributions to the CIC is crucial for the optimization of process parameters for the fabrication of microlectrodes based on IrO_2 thin films. In this thesis, sputtered iridium oxide films (SIROFs) utilized for subretinal electrical stimulation with the state-of-the-art retinal prosthesis "Retina Implant Alpha AMS" are characterized in detail by electrochemical impedance spectroscopy (EIS) and equivalent-circuit fitting to reveal different charge injection mechanisms and to assess the stimulation efficiency of the SIROF-microelectrodes.

Finally, a new approach for bioelectronic interfacing of electrogenic cells

or tissue is introduced, which utilizes a conductive microelectrode insulated with a ferroelectric layer for extracellular electrical stimulation of electrogenic cells or tissue. Here, the switching regime of a ferroelectric microelectrode in an electrolyte–ferroelectric–conductor configuration is analyzed based on the traditional Kolmogorov-Avrami-Ishibashi (KAI)-model and the time-dependent stimulation current in response to an applied voltage step is simulated for a generic microelectrode geometry. It will be shown in this thesis, that the extracellular stimulation current provided by the ferroelectric microelectrode and can increase the CIC by up to two orders of magnitude as compared to the commonly used extracellular capacitive stimulation with microelectrodes coated with an insulating dielectric and paves the way for (new) bioelectronic devices with ferroelectric–neural interfaces for extracellular electrical stimulation and recording.

Before the results of this thesis will be discussed in more detail in chapter 2, we will provide a brief introduction of the investigated material classes in the next section.

1.2 Functional oxide materials

This section comprises a brief (non-exhaustive) introduction into basic physical properties of the two different classes of functional oxides materials investigated in this work, in order to provide basic knowledge for the publications discussed in chapter 2. Throughout the whole section, we make the assumption that every vector quantity $\mathbf{V}$ is fully described by a single component V and all other components vanish unless otherwise stated.

1.2.1 Lead-free ferroelectrics

Ferroelectric materials are characterized by the existence of a spontaneous ferroelectric polarization $\mathbf{P}^{(\mathrm{FE})}$, which can be reoriented by an applied electric field $\mathbf{E}$ [24]. The finite value of the ferroelectric polarization at zero electric field is called the remanent polarization P_{r}. By applying an electric field above the coervice field E_{C} of the ferroelectric, the remanent polarization can be switched between the bistable states $\pm P_{\mathrm{r}}$, which is the basis for nonvolatile ferroelectric memory applications [25].

Materials with ferroelectric properties also exhibit dielectric properties and in linear approximation, the dielectric polarization $\mathbf{P}^{(\mathrm{DE})}$ is given by

$$\mathbf{P}^{(\mathrm{DE})}(\mathbf{E}) = \varepsilon_0(\varepsilon_r - 1)\mathbf{E} \quad , \tag{1.3}$$

with the vacuum permittivity ε_0. Thus, the total electric polarization of a ferroelectric is $\mathbf{P} = \mathbf{P}^{(\mathrm{DE})} + \mathbf{P}^{(\mathrm{FE})}$. As a consequence, the electric displacement field $\mathbf{D} = \varepsilon_0\mathbf{E} + \mathbf{P}$ of a ferroelectric material is then given by

$$\mathbf{D}^{(\mathrm{FE})}(\mathbf{E}) = \varepsilon_0\varepsilon_r\mathbf{E} + \mathbf{P}^{(\mathrm{FE})}(\mathbf{E}) \quad . \tag{1.4}$$

In the switching regime $E > E_{\mathrm{C}}$, Eq. (1.4) is the foundation of the occurrence of the ferroelectric hysteresis loop, i.e. the nonlinear and hysteretic D vs E relationship [26]. A schematic sketch of a ferroelectric thin film parallel-plate capacitor stack with plate distance d is shown in Fig. 1.1 (a), where the remanent polarization of the ferroelectric is in the state $+P_{\mathrm{r}}$. The nonlinear and hysteretic relationship D vs E depicted in Fig. 1.1(b) is plotted with the model described in Ref. [28] by taking the ferroelectric properties of a 9.5-nm-thick $Hf_{0.5}Zr_{0.5}O_2$ layer described in Ref. [27] as model parameters. Experimentally, the D vs E hysteresis loop of a parallel-plate ferroelectric capacitor in response to an applied bipolar voltage signal $U(t)$ – which generates an electric field $E(t) = U(t)/d$ – can be measured, e.g., by the virtual ground method or by utilizing a Sawyer-Tower circuit [24].

In addition, we note that there exist also ab-inito methods to calculate material properties of ferroelectrics. Here, the state-of-the-art method is the

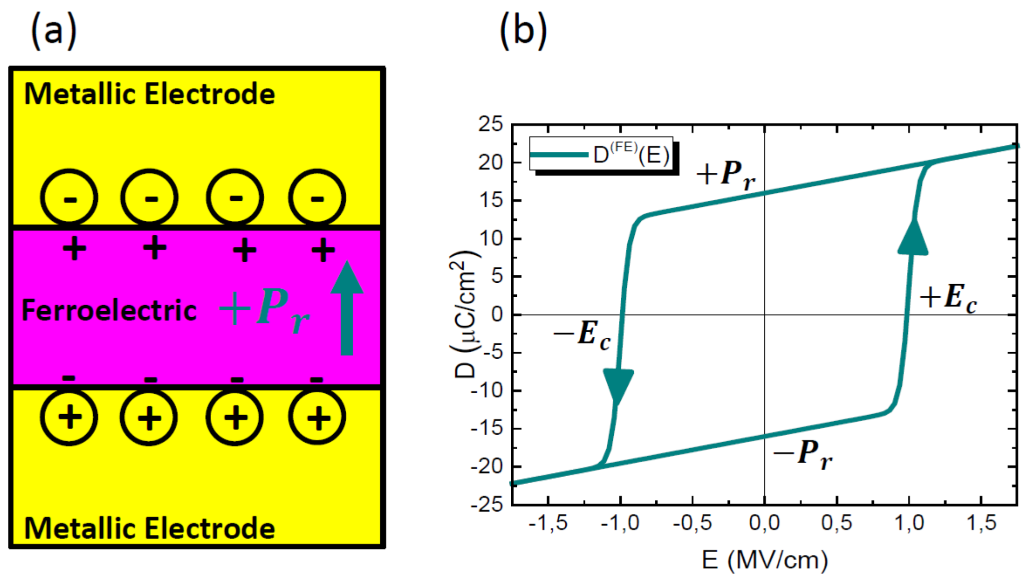

Figure 1.1: (a) Schematic sketch of metal–ferroelectric–metal configuration in the polarization state $+P_{\mathrm{r}}$. In equilibrium, free charges in the metallic electrodes screen the bound polarization charges of the ferroelectric layer. (b) Nonlinear and hysteretic relationship D vs E for a ferroelectric material with $\varepsilon_r = 40$, $P_{\mathrm{r}} = 16\ \mu\mathrm{C/cm}^2$ and $E_{\mathrm{C}} = 1$ MV/cm, e.g., $\mathrm{Hf}_{0.5}\mathrm{Zr}_{0.5}\mathrm{O}_2$ [27] .

so-called "modern theory of polarization" , which allows one to calculate the electric polarization $\mathbf{P}$ of a given crystal structure and subsequently, material properties such as the spontaneous ferroelectric polarization, piezoelectric coefficients, Born effective charges or the dielectric permittivity can be obtained which are either finite differences or derivatives of the electric polarization $\mathbf{P}$ [29, 30]. An alternative approach for calculating the properties of bulk ferroelectrics might be based on the recently introduced theory of local fields in crystalline dielectrics [31]. This theory provides an explicit expression to calculate the electric polarization $\mathbf{P}$ of a crystal from the knowledge of the microscopic polarizabilities of the lattice sites, which might be useful to design (new) ferroelectric materials with, e.g., giant piezoelectric coefficients and/or enhanced remanent polarization P_{r}.

Since the operating range of many MEMS devices based on ferroelectric thin films is below the coercive field of the utilized ferroelectric [32], we will focus in the following on the subswitching regime $E < E_{\mathrm{C}}$. Here, the complex dynamics of domain wall displacement can be considered as a superposition of center-of-mass motion and relaxational motion of internal modes (segments) [19]. This results in a dependence of the relative permittivity ε_r on the amplitude E_0 and frequency f of an applied ac electric field

[14, 15]. For the frequency dependence of permittivity, theory predicts for domain wall pinning processes in random systems a logarithmic dependence of permittivity on frequency f, which is due to the relaxational contribution of domain wall segments [18, 19]. The pinning of domain wall segments results in a distribution of relaxation times in the ferroelectric. In many ferroelectrics - including relaxors - it was found that the logarithmic frequency dependence of the complex relative permittivity can be well approximated by the following expression, which is valid for ferroelectric systems with a broad distribution of relaxation times [15, 33–35]

$$\begin{aligned} \varepsilon_r'(f) &= \varepsilon_{r,0}' + \Delta\varepsilon_r' \ln\left(\frac{1\,\mathrm{Hz}}{2\pi f}\right) \quad , \\ \varepsilon_r''(f) &= \varepsilon_{r,0}'' \quad , \end{aligned} \tag{1.5}$$

where $\varepsilon_{r,0}'$ and $\varepsilon_{r,0}''$ denote static contributions to the permittivity, and $\Delta\varepsilon_r'$ is the logarithmic dispersion strength.

Regarding the field dependence of permittivity, the linear dependence of permittivity on the field amplitude E_0 above a specific threshold field E_T and below the coercive field E_C is described by the Rayleigh law and the corresponding Rayleigh behavior in ferroelectric materials, which originates from the irreversible center-of-mass motion of ferroelectric domain walls [32, 36–38]. The Rayleigh law for the real and imaginary parts of the complex relative permittivity $\varepsilon_r = \varepsilon_r' - i\varepsilon_r''$ is given by [20, 32]

$$\begin{aligned} \varepsilon_r'(E_0) &= \varepsilon_{r,\mathrm{in}}' + \alpha' E_0 \quad , \\ \varepsilon_r''(E_0) &= \varepsilon_{r,\mathrm{in}}'' + \alpha'' E_0 \quad . \end{aligned} \tag{1.6}$$

Here $\varepsilon_{r,\mathrm{in}}'$ and $\varepsilon_{r,\mathrm{in}}''$ are real and imaginary parts of the reversible (initial) Rayleigh parameter $\varepsilon_{r,\mathrm{in}}$ due to lattice and reversible domain wall contributions, α' denotes the irreversible Rayleigh parameter (Rayleigh constant) and $\alpha'' = \frac{4}{3\pi}\alpha'$. In the following, a general linear field dependene of $\varepsilon_r'(E_0)$ and $\varepsilon_r''(E_0)$ with positive slope will be denoted as "Rayleigh-like behavior" and results in a nonlinear and hysteretic dielectric polarization, which is also referred to as dielectric nonlinearity [38]. In that sense, the Rayleigh law is a special case of Rayleigh-like behavior with the additional requirement $\alpha'' = \frac{4}{3\pi}\alpha'$. The irreversible domain wall contribution to the real part of the permittivity is given by $\alpha' E_0$. It turns out, that α' is a direct and quantitative measure for the mobility of domain walls, and it is dependent on the concentration of pinning centers, film thickness and the density of domain walls [38]. However, the Rayleigh law Eq. (1.6) is rate-independent and no frequency dependence of material properties can be derived from it

[15, 34, 38]. Additionally, it should be noted that a unified theory which describes the field and frequency behavior of material properties, e.g., the complex relative permittivity $\varepsilon_r(E_0, f)$ of ferroelectrics, with the same set of equations is not available.

Regarding possible ferroelectric materials for applications in MEMS and biosensor devices, great progress has been achieved in the field of lead-free ferroelectrics inpired by legal restrictions to replace lead by nontoxic materials [16]. Here, a promising lead-free material for the replacement of toxic PZT is the solid-solution BCZT, which exhibits outstanding properties prepared as bulk ceramic sample [23]. However, BCZT thin film samples and films based on similar $BaTiO_3$ solid-solutions are far less investigated and there is still a huge lack of experience in thin film growth and electrical characterization of BCZT compared to PZT. In this thesis, a method will be presented which allows one to extract $\varepsilon_r(E_0, f)$ from impedance spectroscopy measurements and this method will be demonstrated by applying it to capacitor stacks containing polycrystalline or epitaxial BCZT thin films grown by PLD on different substrates.

1.2.2 Conductive oxides for electro–neural interfaces

Extracellular electrical stimulation of neurons and recording of neural activity are the basic principles for many *in vivo* applications such as implantable neuroprosthetic devices [39]. Among them are cochlear implants, retinal implants, deep brain stimulation for the treatment of Parkinsons's disease and brain-machine interfaces [4–6, 40, 41]. Moreover, extracellullar electrical stimulation and recording are also key elements for *in vitro* applications, e.g., drug testing and the study of neural networks by microelectrode arrays (MEAs) [42, 43].

Typically, electrically active implants and MEAs utilize conductive (metallic) microelelectrodes with diameter < 100 μm to provide the electro–neural interface for extracellular recording and stimulation [39]. Electrical stimulation is achieved by the flow of ionic current between a microelectrode in close proximity to the target excitable cell or tissue and a counter electrode immersed in the electrolyte, which contains the cell or tissue [39]. The ionic current flow in proximity to the cell or tissue causes a depolarization of the cell membrane, which evokes an action potential above a specific threshold. For efficient extracellular electrical stimulation, the utilized microelectrodes are required to provide a high charge injection capacity (CIC), which is defined as the amount of injected charge density across the electrode–elelctrolyte interface during the leading stimulation phase of an extracellular current [39]. Exemplary materials for the fabrication of conductive microelectrodes are

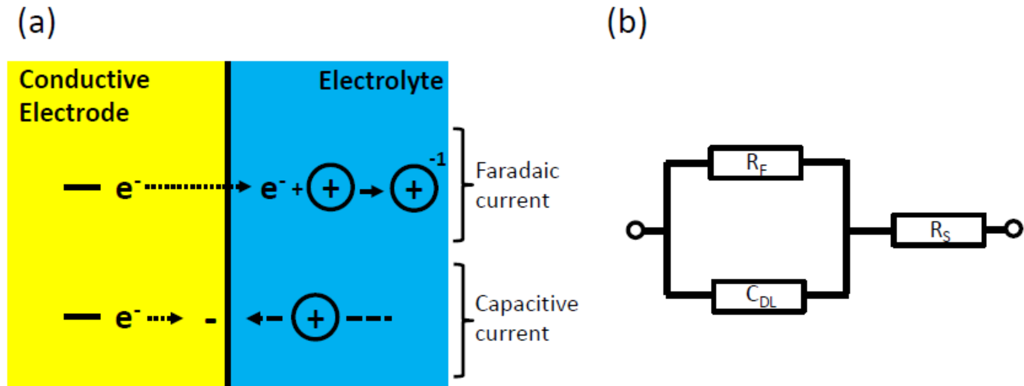

Figure 1.2: (a) Schematic sketch of the conductive electrode–electrolyte interface with capacitive and Faradaic charge injection mechanisms. (b) Simple equivalent-circuit model of an conductive electrode–electrolyte interface. The Ohmic resistance R_{F} models Faradaic charge injection and the capacitance C_{DL} represents the electrochemical double-layer. The serial Ohmic resistor R_{s} models the resistance of the electrodes and the electrolyte.

Pt for high-density MEA applications [43] and IrO_2 which is utilized, e.g., in state-of-the-art retinal prostheses [5] and which can provide a CIC in the range of 1 - 5 mC/cm^2 [39, 44].

For conductive microelectrodes, charge injection into an adjacent electrolyte – which contains the target excitable cell or tissue – can occur by two different charge transport mechanisms, i.e. by capacitive currents and Faradaic currents. A schematic sketch of the conductive electrode–electrolyte interface is depicted in Fig. 1.2 (a). Here, Faradaic charge injection corresponds to a direct electrochemical charge transfer across the electrode–electrolyte interface by reversible and irreversible chemical reactions, whereas capacitive currents across the electrode–electrolyte interface occur due to the charging and discharging of the electrochemical double-layer which is formed at the interface due to electrical polarization of the microelectrode. A simple equivalent-circuit model for the conductive electrode–electrolyte interface is shown in Fig. 1.2 (b), where the Ohmic resistor R_{F} models Faradaic charge injection, the capacitance C_{DL} represents the electrochemical double-layer and R_{s} models the Ohmic resistance of the electrodes and the electrolyte.

Experimentally, electrode–electrolyte interfaces of microelectrodes can be investigated by electrochemical impedance spectroscopy (EIS). By fitting measured EIS data to an appropriate equivalent-circuit model, the Faradaic and capacitive contributions to the CIC provided by the microelectrode can be quantified. Here, Faradaic charge injection has the disadvantage that the underlying chemical reaction at the electrode–electrolyte interface can be irreversible which results in corrosion of electrodes and cell or tissue damage [45].

Such irreversible electrochemical processes affect detrimentally the safety and long-term-stability of implantable neuroprosthetic devices and hence significantly reduce their treatment outcome. Obviously, electrochemical degradation processes are also adverse effects for *in vitro* applications.

A possible solution to prevent toxic electrochemical effects is the utilization of microelectrodes coated with a (thin) dielectric material. This approach was crucial for the first realization of a silicon–neuron junction, where *p*-doped areas of the utilized silicon chip were covered with a 10-nm-thick dielectric layer of SiO_2 to prevent Faradaic currents and to stimulate the attached neuron by purely capacitive currents across the dielectric–electrolyte interface [46]. Modern capacitive biochips for extracellular electrical stimulation are fabricated in complementary metal-oxide-semiconductor (CMOS) technology and include field-effect transistors to record electrical signals from individual neurons [47], which enables the bidirectional communication between neurons and active silicon chips [48]. However, despite extensive research for dielectric coatings to enhance the purely capacitive stimulation with microelectrodes, their CIC is still in the range of $\sim$ 1 - 5 μC/cm^2 [48–52], which is approximately three orders of magnitude lower than the CIC of generic conductive microelectrodes. Since the stimulation-threshold for the injected charge density depends on the geometric area of the microelectrode [53], the CIC of capacitive microelectrodes is too low to achieve extracellular stimulation with small microelectrodes (diameter $\sim$ 30 μm) which requires a CIC in the range of 0.1 - 0.9 mC/cm^2 [53], although a tight tissue–electrode contact can lower the stimulation-threshold [51]. As a consequence, capacitive microelectrodes are not utilized for *in vivo* applications such as implantable neuroprosthetic devices although the absence of toxic electrochemical effects is highly desired in active electrical implants. In the next chapter of this thesis, a solution to this long-stand problem will be introduced.

Chapter 2

Summary of publications and contributions

This chapter is divided into four sections, where each section contains a summary and a statement of author contributions to one of the appended publications I - IV. A significant part of this chapter contains modified text passages and figures from the appended publications.

2.1 Publication I

The basic idea of this publication is to use impedance spectroscopy to analyze the contribution of domain-wall-motion to the dielectric response of a ferroelectric material. In an impedance spectroscopy experiment, the complex impedance $Z = Z' - iZ''$ is measured as a function of frequency f of an applied ac electric field with amplitude E_0, typically in the range of $f = 10 - 10^6$ Hz. Measured impedance $Z(f)$ data can be converted into complex relative permittivity $\varepsilon_r(f)$ data by [54]

$$\varepsilon_r(f) \quad = \quad \frac{1}{i2\pi f C_0 Z(f)} \quad , \tag{2.1}$$

where C_0 denotes the geometrical capacitance. However, the measured impedance contains not only contributions from the investigated material. In fact, the measured impedance contains also contributions from, e.g., contacts, (imperfect) electrodes and/or interfaces to the electrodes, and hence, the simple conversion of impedance data into permittivity data by Eq. (2.1) is not adequate to extract the dielectric dispersion $\varepsilon_r(f)$ of the investigated material over the measured frequency-range, which is especially true for thin film samples. Thus, deconvolution of measured impedance spectra is required, which corresponds to the discrimination of different contributions to

the impedance, originating from electronically different components of the analyzed sample. To achieve this for ferroelectrics, a new equivalent-circuit element is needed which models the impedance of a ferroelectric including the contribution from domain wall pinning in a random energy landscape. In the publication, a new equivalent-circuit element is derived as follows. Inverting Eq. (2.1) and separating real and imaginary parts, yields

$$Z(f) = \frac{\varepsilon_r''(f) - i\varepsilon_r'(f)}{2\pi f C_0 \left\{\varepsilon_r'(f)^2 + \varepsilon_r''(f)^2\right\}} \quad . \tag{2.2}$$

By inserting the logarithmic frequency dependence Eq. (1.5) into Eq. (2.2), we obtain the equivalent-circuit element Z_{DW}, which models the impedance of a ferroelectric including the contribution due to domain wall pinning in a random energy landscape

$$Z_{\mathrm{DW}}(f) = \frac{\varepsilon_{r,0}'' - i\left[\varepsilon_{r,0}' + \Delta\varepsilon_r' \ln\left(\frac{1\,\mathrm{Hz}}{2\pi f}\right)\right]}{2\pi f C_0 \left\{\left[\varepsilon_{r,0}' + \Delta\varepsilon_r' \ln\left(\frac{1\,\mathrm{Hz}}{2\pi f}\right)\right]^2 + \varepsilon_{r,0}''^2\right\}} \quad , \tag{2.3}$$

with $\varepsilon_{r,0}'$, $\varepsilon_{r,0}''$ and $\Delta\varepsilon_r'$ as free parameters. Consequently, Z_{DW} will be called the "domain wall pinning element" in the following. Impedance spectroscopy allows one to extract the fit parameters $\varepsilon_{r,0}'$, $\varepsilon_{r,0}''$ and $\Delta\varepsilon_r'$ by fitting the measured impedance over the full frequency range to the impedance of an appropriate equivalent-circuit model of the capacitor stack, including the ferroelectric.

In publication I, this is done for different excitation field amplitudes E_0 on capacitor stacks, containing ferroelectric $0.5(\mathrm{Ba}_{0.7}\mathrm{Ca}_{0.3})\mathrm{TiO}_3$–$0.5\mathrm{Ba}(\mathrm{Zr}_{0.2}\mathrm{Ti}_{0.8})\mathrm{O}_3$ (BCZT) thin films, epitaxially grown by pulsed laser deposition on Nb-doped SrTiO_3 (Nb:STO) single crystal substrates and covered with circular Au electrodes. Results of the fits to the measured impedance are depicted in Fig. 2.1(a), and the equivalent circuit depicted in Fig. 2.1(b) was used to fit the collected impedance spectra. Here the series resistance R_0 corresponds to the resistance of the cables, measurement probes and the electrodes. The R_1C_1-Element represents the electrode-BCZT interfaces. The resistance R_2 and Z_{DW} model the ferroelectric film inside the capacitor stack. R_2 is attributed to losses due to possible leakage currents, whereas the losses due to domain wall motion are contained in Z_{DW}. Additionally, the dispersion parameters are contained in the domain wall pinning element. The element L_0 models the inductance of the cables used.

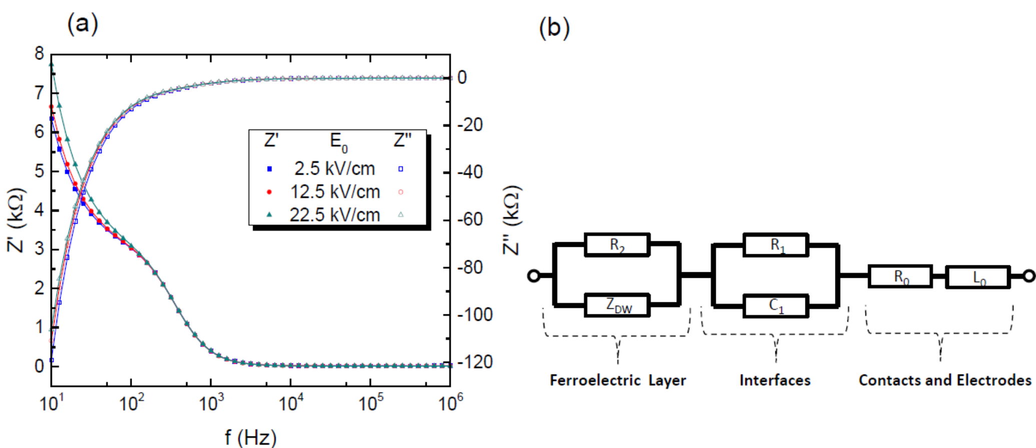

Figure 2.1: (a) Bode plots $Z'(f)$ and $Z''(f)$ obtained by impedance spectroscopy (symbols) for different E_0 on epitaxial BCZT thin film capacitor. The equivalent circuit in (b) was used to fit the data (solid lines). Figure modified from appended publication I.

From the obtained fit parameters, the complex relative permittivity $\varepsilon_r(f)$ of the BCZT film can be calculated according to Eq. (1.5) for each field amplitude E_0. Fig. 2.2(a) shows a cross-sectional scanning transmission electron microscopy (STEM) image of the epitaxial Nb:STO/BCZT interface viewed along the [010] zone axis. Here, the STEM analysis revealed the occurrence of edge-type misfit dislocations at the epitaxial Nb:STO/BCZT interface, characterized by the Burgers vector $\mathbf{b} = a[100]$, where a denotes the lattice constant along the [100] direction within the BCZT unit cell. These misfit dislocations act as possible domain wall pinning centers, which was already observed in similar epitaxial PZT heterostructures [55]. In Fig. 2.2(b), the extracted complex relative permittivity $\varepsilon_r(f)$ of the BCZT film (i.e., without contributions from the electrodes and ferroelectric/electrode interfaces) from the equivalent-circuit fits is depicted (for a selection of three different E_0). We clearly observe that the dielectric dispersion $\varepsilon_r(f)$ depends on the field amplitude E_0, which indicates that dielectric nonlinearity and frequency dispersion are coupled in the BCZT films. From the equivalent-circuit fits, the field dependence of the dispersion parameters $\varepsilon'_{r,0}(E_0)$, $\varepsilon''_{r,0}(E_0)$ and $\Delta\varepsilon'_r(E_0)$ can be extracted and the results are depicted in Fig. 2.3(a).

In publication I, it is then shown that the field dependence of the dispersion parameters can be written in the following form

$$\begin{aligned} \varepsilon'_{r,0}(E_0) &= \varepsilon'_{r,\mathrm{in},0} + \alpha'_0 E_0 \quad , \\ \varepsilon''_{r,0}(E_0) &= \varepsilon''_{r,\mathrm{in}} + \alpha'' E_0 \quad , \\ \Delta\varepsilon'_r(E_0) &= \Delta\varepsilon'_{r,\mathrm{in}} + \Delta\alpha' E_0 \quad . \end{aligned} \tag{2.4}$$

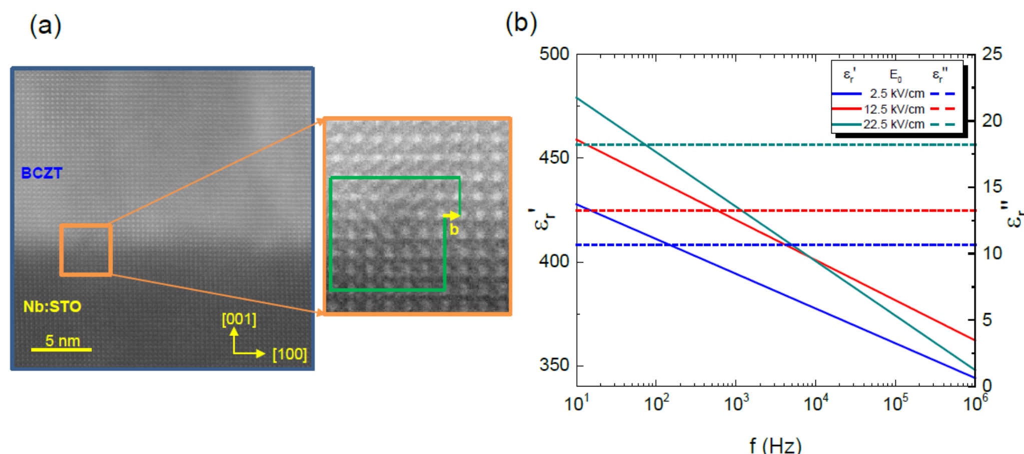

Figure 2.2: (a) Cross-section STEM image of Nb:STO/BCZT interface viewed along the [010] zone axis. The enlarged section shows an edge-type misfit dislocation with Burgers vector $\mathbf{b} = a[100]$. (b) Extracted complex relative permittivity $\varepsilon_r(f)$ of the BCZT film for a selection of three different excitation field amplitudes E_0. Figure modified from appended publication I.

Here, the coefficients $\varepsilon'_{r,\text{in},0}$, $\varepsilon''_{r,\text{in}}$, α'_0, α'' denote static contributions to the complex reversible (initial) Rayleigh parameter $\varepsilon_{r,\text{in}} = \varepsilon'_{r,\text{in}}(f) - i\varepsilon''_{r,\text{in}}$ and the complex irreversible Rayleigh parameter $\alpha = \alpha'(f) - i\alpha''$ [20, 32, 38], and $\Delta\varepsilon'_{r,\text{in}}$, $\Delta\alpha'$ describe the logarithmic frequency dispersion strength of the Rayleigh parameters, given by

$$\begin{aligned}\varepsilon'_{r,\text{in}}(f) &= \varepsilon'_{r,\text{in},0} + \Delta\varepsilon'_{r,\text{in}} \ln\left(\frac{1\,\text{Hz}}{2\pi f}\right) \quad , \\ \alpha'(f) &= \alpha'_0 + \Delta\alpha' \ln\left(\frac{1\,\text{Hz}}{2\pi f}\right) \quad . \end{aligned} \tag{2.5}$$

In publication I, it is shown that $\Delta\alpha'$ corresponds to the coupling strength between the logarithmic frequency dispersion and linear field dependence of permittivity. Subsequently, linear fits according to Eq. (2.4) were carried out in the range $6.25\,\text{kV/cm} \leq E_0 \leq 16.25\,\text{kV/cm}$, as indicated by the vertical dashed lines in Fig. 2.3(a). The starting point for the linear fits at $E_0 = 6.25\,\text{kV/cm} \equiv E_\text{T}$ was determined by the criterion that all subsequent data points are required to have a higher value compared to their left neighbor. The endpoint for the linear fits was then chosen by the longest fitting range for which every linear fit has a correlation factor $R^2 \geq 0.980$, which is fulfilled for $E_0 = 16.25\,\text{kV/cm} \equiv E_\text{PS}$. At higher fields, all three curves in Fig. 2.3(a), show an upward curvature which we attribute to the partial switching of domains [32]. For the linear fits, the estimated standard errors from the

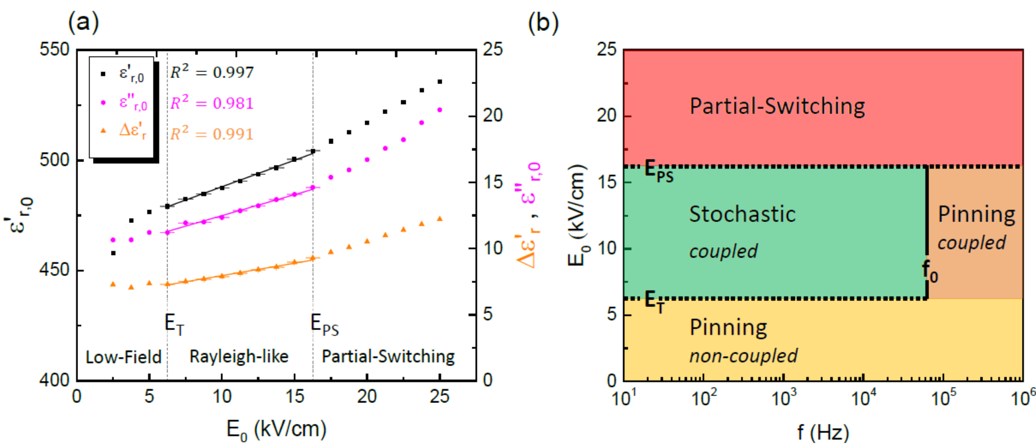

Figure 2.3: (a) Field dependence of the dispersion parameters $\varepsilon'_{r,0}(E_0)$, $\varepsilon''_{r,0}(E_0)$ and $\Delta\varepsilon'_r(E_0)$ of the BCZT film. The solid lines are linear fits in the region between the two vertical dashed lines, which mark the threshold field E_{T} and the partial switching field E_{PS}.

previous equivalent-circuit fitting procedure were taken into account, which is also indicated by the error bars within the fitting range [c.f. Fig. 2.3(a)].

Altogether, the extended Rayleigh analysis carried out in detail in publication I yields the schematic diagram depicted in Fig. 2.3(b) for the different domain wall motion regimes in the epitaxial BCZT thin film. Note, that the diagram constructed in Fig. 2.3(b) is not a generic diagram for any epitaxial BCZT film. In fact, it is a schematic diagram of different domain-wall motion regimes, which can now be identified within the framework of the extended Rayleigh analysis.

At low field amplitudes $0 < E_0 < E_{\mathrm{T}}$, the center-of-mass of the domain walls cannot overcome the potential well of the random energy landscape, however, domain wall segments can jump between metastable states with close energies, which corresponds to the non-coupled pinning regime. This observation has similarities to what has been found theoretically for disordered ferromagnets [56]. By increasing the field amplitude above the threshold field E_{T}, the center-of-mass of the domain walls can additionally jump between different potential minima, resulting in a coexistence of irreversible center-of-mass motion and relaxational motion of internal modes in the stochastic regime. Note that this coexistence is not simply additive, due to the coupling of dielectric nonlinearity and frequency dispersion. As a consequence of coupling, the irreversible Rayleigh parameter becomes zero at $f_0 \sim 63$ kHz and changes to negative values in the pinned coupling regime. Note that in this coupled-pinning regime, domain wall segments can still jump between metastable states, which is indicated by the logarithmic fre-

quency dispersion observed in this regime. The domain wall dynamics in the coupled-pinning regime is not fully understood and remains as a task of a unified theory of dielectric nonlinearity and frequency dispersion, which is not yet available.

Author contributions to Publication I

I developed the scientific idea of the publication and I planned and carried out all experiments except for TEM sample preparation which was organized by C. Burkhardt. I fabricated the 200-nm-thick epitaxial BCZT thin films on (100)-oriented Nb-doped $SrTiO_3$ single crystal substrates by means of PLD and performed the subsequent microstructural analysis by x-ray diffraction (XRD) and scanning transmission electron microscopy (STEM). For electrical measurements, I fabricated BCZT capacitor stacks by electron beam evaporation of circular Au electrodes on top of the films. I carried out the impedance spectroscopy measurements and wrote a custom-made Wolfram Mathematica script for equivalent-circuit fitting and data analysis. Finally, I wrote the manuscript, with input from the other coauthors.

2.2 Publication II

This publication utilizes the domain wall pinning element Z_{DW} to extract the field- and frequency-dependent dielectric response of polycrystalline BCZT thin film capacitor stacks grown by PLD on platinized Si substrates. The main scientific goal of this publication is to reveal how the presence of grain boundaries in BCZT influences the domain-wall-motion dynamics in BCZT. This is done, by comparing the results of the extended Rayleigh analyis performed on a polycrystalline BCZT capacitor stack with the results from the epitaxial BCZT thin film capacitor stack analyzed in Publication I.

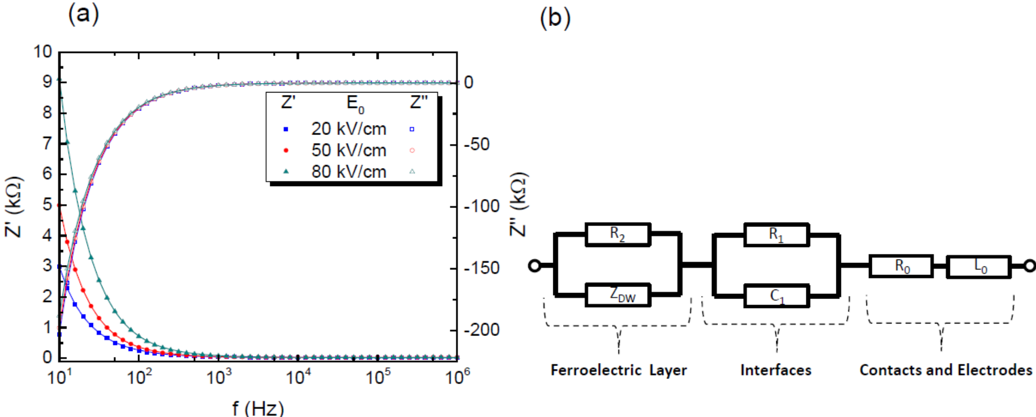

Figure 2.4: (a) Bode plots $Z'(f)$ and $Z''(f)$ obtained by impedance spectroscopy (symbols) for different E_0 on polycrystalline BCZT thin film capacitor. The equivalent circuit in (b) was used to fit the data (solid lines). Figure modified from appended publication II. ©AIP Publishing.

For this purpose, impedance spectra from 10 Hz to 1 MHz were collected at different excitation field amplitudes E_0 on a capacitor stack containing a 200-nm-thick polycrystalline BCZT thin film. Following the procedure described in Publication I, the measured impedance spectra were deconvoluted by domain wall pinning element modeling and equivalent-circuit fitting. Results of the fits can be seen in the Bode plot [57] shown in Fig. 2.4(a), where the real and the imaginary parts of the impedance $Z = Z' - iZ''$ are plotted vs frequency (for three selected values of E_0). In all cases, the fits with the equivalent-circuit model depicted in Fig. 2.4(b) are in good agreement with the measured data, indicating that the equivalent circuit used is a suitable model for the capacitor stacks. Moreover, we observe columnar growth of the grains from the cross-sectional STEM image depicted in Fig. 2.5(a), which extend throughout the whole film thickness i.e. there are no grain boundaries and grains connected in series, and hence their contribution cannot be sep-

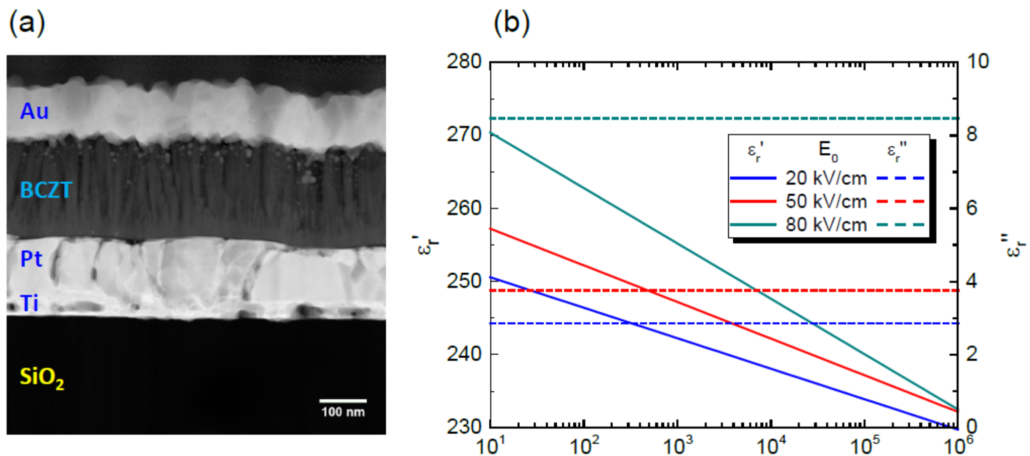

Figure 2.5: (a) Cross-section STEM image of polycrystalline thin film capacitor stack. The columnar grains in the BCZT film extend throughout the whole film thickness. (b) Extracted complex relative permittivity $\varepsilon_r(f)$ of the BCZT film for a selection of three different excitation field amplitudes E_0. Figure modified from appended publication II. ©AIP Publishing.

arated by impedance spectroscopy [20], which justifies modelling the BCZT layer as an R_2 - Z_{DW} parallel circuit.

Subsequently, the complex relative permittivity $\varepsilon_r(f)$ of the BCZT film was calculated from the obtained fit parameters according to Eq. (1.5) for each field amplitude E_0. The results for a selection of three different excitation-field amplitudes are depicted in Fig. 2.5(b). Additionally, the field dependence of the dispersion parameters $\varepsilon'_{r,0}(E_0)$, $\varepsilon''_{r,0}(E_0)$ and $\Delta\varepsilon'_r(E_0)$ can be investigated from the obtained fit parameters, and the results are shown in Fig. 2.6(a). All dispersion parameters exhibit a linear dependence (with positive slope) on the excitation field amplitude E_0 within the threshold field E_{T} and the partial switching field E_{PS}.

Following the extended data analysis introduced in Publication I, the curves are fitted within the range 45 kV/cm $\leq E_0 \leq$ 70 kV/cm as indicated by the dashed vertical lines [c.f. Fig. 2.6(a)] to the linear equations

$$\begin{aligned} \varepsilon'_{r,0}(E_0) &= \varepsilon'_{r,\mathrm{in},0} + \alpha'_0 E_0 \quad , \\ \varepsilon''_{r,0}(E_0) &= \varepsilon''_{r,\mathrm{in}} + \alpha'' E_0 \quad , \\ \Delta\varepsilon'_r(E_0) &= \Delta\varepsilon'_{r,\mathrm{in}} + \Delta\alpha' E_0 \quad . \end{aligned} \tag{2.6}$$

Finally, the analysis presented in publication II yields the schematic diagram depicted in Fig. 2.6(b) for the different domain-wall-motion regimes in the polycrystalline BCZT thin film. At field amplitudes $0 < E_0 < E_{\mathrm{T}}$, the center of mass of the domain walls is pinned in a potential well of the

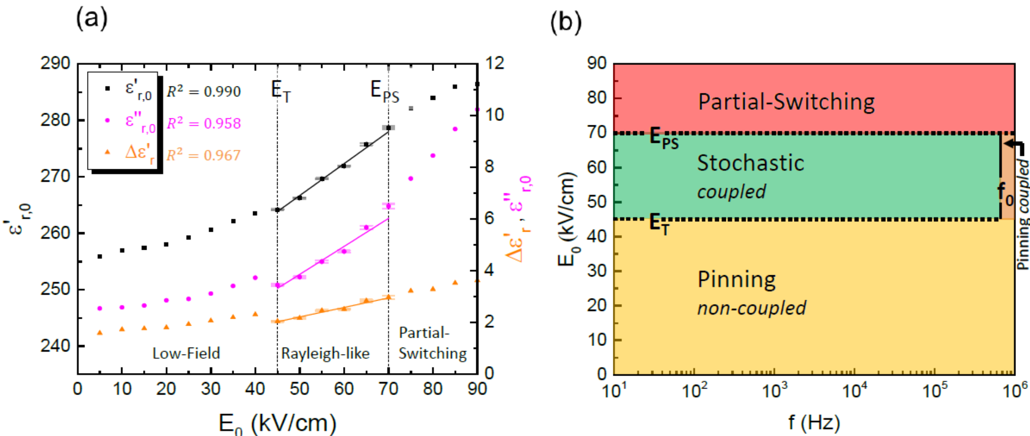

Figure 2.6: (a) Field dependence of the dispersion parameters $\varepsilon'_{r,0}(E_0)$, $\varepsilon''_{r,0}(E_0)$ and $\Delta\varepsilon'_r(E_0)$. The solid lines are linear fits in the region between the two vertical dashed lines, which mark the threshold field E_T and the partial switching field E_PS. (b) Schematic diagram of the different domain-wall-motion regimes of the polycrystalline BCZT thin film. Figure modified from appended publication II. ©AIP Publishing.

random energy landscape, however domain-wall segments can jump between metastable states with close energies, which corresponds to the non-coupled pinning regime (see Publication I). By increasing the field amplitude above the threshold field $E_\mathrm{T} = 45$ kV/cm, the center of mass of the domain walls can overcome the potential well and move irreversibly via hopping between different potential minima, resulting in a coexistence of irreversible center-of-mass motion and relaxational motion of internal domain-wall segments in the stochastic regime (see Publication I). Note that the threshold field E_T in the polycrystalline thin film is significantly higher as compared to what has been reported for an epitaxial BCZT film of the same thickness (see Publication I), which we attribute to the higher density of defects present in the polycrystalline film [58]. For field amplitudes above $E_\mathrm{PS} = 70$ kV/cm, partial switching of the domains occurs. The irreversible Rayleigh parameter $\alpha'(f)$ becomes zero and changes to negative values at $f_0 \sim 682$ kHz, which originates from the coupling between dielectric nonlinearity and frequency dispersion (see Publication I). This indicates a transition to the coupled pinning regime, where the center of mass of the domain walls cannot follow the fast driving field [19, 59] but domain wall segments can still jump between metastable states [19]. However the comprehensive domain-wall dynamics in the coupled pinning regime – which includes a negative irreversible Rayleigh parameter $\alpha'(f)$ – is not precisely known, and more experimental and theoretical work is needed for an improved understanding. The results of this publication indicate that the presence of grain boundaries does not only re-

duce the value of the Rayleigh constant but also weakens the relaxational motion of internal domain-wall segments and the coupling strength between dielectric nonlinearity and frequency dispersion.

Author contributions to Publication II

I developed the scientific idea of the publication and I planned and conducted all experiments except for TEM sample preparation, which was done by B. Schröppel. I fabricated the 200-nm-thick polycrytalline BCZT thin films by means of PLD on platinized Si substrates and performed their subsequent microstructural analysis by x-ray diffraction (XRD) and scanning transmission electron microscopy (STEM). For electrical measurements, I fabricated BCZT capacitor stacks by electron beam evaporation of circular Au electrodes on top of the films. I carried out the impedance spectroscopy measurements and wrote a custom-made Wolfram Mathematica script for equivalent-circuit fitting and data analysis. Finally, I wrote the manuscript, with input from the other coauthors.

2.3 Publication III

This publication discusses in detail the fabrication process of conductive microelectrodes based on sputtered iridium oxide films (SIROFs) for subretinal electrical stimulation with the state-of-the-art retinal prosthesis “Retina Implant Alpha AMS” and the comprehensive electrical characterization of the microelectrodes by cyclic voltammetry (CV), electrochemical impedance spectroscopy (EIS) and voltage transient measurements. The focus of the electrical measurements is to assess the stimulation efficiency of the SIROF microelectrodes and to reveal and quantify the contributions from different charge injection mechanisms to the CIC.

A characteristic feature of IrO_2-based electrodes is the ocurrence of a fast and reversible Faradaic process involving reduction and oxidation of Ir^{3+}/ Ir^{4+} confined to the surface of the electrode [44, 60, 61]. The quasi-continuous oxidation states of IrO_2-based electrodes enable the reversible storage of a large amount of charge, which is known as pseudocapacitance C_p [61]. As a consequence, the simple equivalent-circuit model of an electrode–electrolyte interface depicted in Fig. 1.2 is insufficient to describe the properties of SIROF-microelectrodes, and an adequate model has to incorporate their pseudocapacitive behavior, which can be described by a constant phase element (CPE) with impedance [57]

$$Z_\mathrm{CPE}(f) = \frac{1}{Q(i2\pi f)^n} \quad , \tag{2.7}$$

where the capacitance-like constant Q and the phenomenological exponent n are free parameters. Moreover, in most cases, the double-layer capacitance C_DL also exhibtis a non-ideal capacitive behavior which is better described by a CPE instead of an ideal capacitor. Due to different time constants for the charging and discharging of C_DL and C_p respectively, they can be discriminated by EIS measurements and appropriate equivalent-circuit fitting. Together, the double-layer capacitance C_DL and the pseudocapacitance are often called the supercapacitance [61]. Fig. 2.7(a) shows EIS data collected on a 650-nm-thick circular SIROF-microelectrode (30 μm in diameter). Here, the solid and the dashed line represent fits to the equivalent-circuit model depicted in Fig. 2.7(b), which are in good agreement with the measured EIS data over the full frequency range. The circuit is a complete model of the electrode-electrolyte interface [61] and includes the double-layer capacitance C_DL, the pseudocapacitance C_p, the Faradaic leakage resistance R_F, the charge transfer resistance R_CT, the Warburg impedance Z_W and the serial resistance R_s. Additionally, a parallel stray capacitance C_stray was included, which is well-known to exist in three-electrode EIS measurements [62]. In

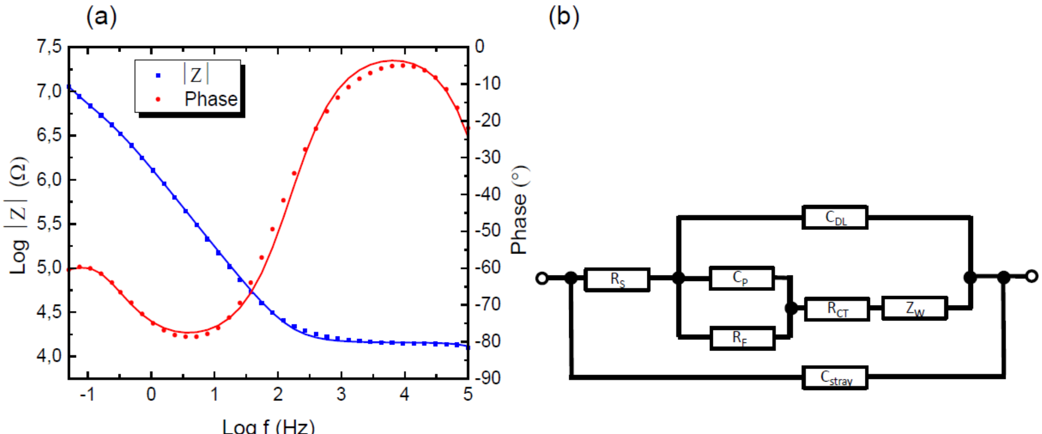

Figure 2.7: (a) Measured impedance modulus $|Z|$ and phase angle obtained by electrochemical impedance spectroscopy (symbols) and the corresponding equivalent-circuit fits (solid lines) (b) Utilized equivalent-circuit model for fitting the EIS data. Figure modified from appended publication III; licensed under a Creative Commons Attribution (CC BY 4.0) license.

the EIS data, C_{stray} causes the phase drop at high frequencies $\sim$ 10 kHz - 100 kHz. The Warburg impedance Z_{W} accounts for mass-transfer limitation by diffusion. Similar to what has been found for other SIROF-microelectrodes, we utilized the Warburg element for finite-length diffusion with reflecting boundary, given by [60]

$$Z_{\text{W}}(f) = R_D \frac{\coth\left(\sqrt{i2\pi f T_D}\right)}{\sqrt{i2\pi f T_D}} \quad , \tag{2.8}$$

with the diffusion resistance R_D and the diffusion time constant T_D as free parameters.

From the equivalent-circuit fits, the double-layer capacitance C_{DL} and the pseudo-capacitance C_{p} are estimated from the obtained fit parameters of the corresponding CPEs by using the procedure described in Ref. [63] which yields $C_{\text{DL}} \approx 71$ nF and $C_{\text{p}} \approx 208$ nF. The resulting supercapacitance corresponds to the sum $C_{\text{DL}} + C_{\text{p}}$, which is dominated by the reversible Faradaic process of quasi-continuous reversible reduction and oxidation between $\text{Ir}^{3+}/\ \text{Ir}^{4+}$ valence states. By normalizing the supercapacitance to the geometric area of the circular SIROF-microelectrode, the specific supercapacitance has a value of $C_{\text{s}}^{(\text{sup})} = 39.4\ \text{mF}/\text{cm}^2$. The supercapacitive current flow at a sweep-rate of 0.1 V/s yields 3.94 mA/cm^2, which is in agreement with the measured CV data in the publication and indicates, that the reversible Faradaic process involving reduction and oxidation of $\text{Ir}^{3+}/\ \text{Ir}^{4+}$ is the dominant contribution to the CIC of the investigated SIROF-microelectrode.

Author contributions to Publication III

This publication was done in collaboration with the Retina Implant AG. I conducted the data analysis of the measured impedance spectra on the SIROF-microelectrodes. For this purpose, I wrote a custom-made Wolfram Mathematica script to fit the impedance data to an appropriate equivalent-circuit model. In the publication, I wrote the section about EIS which contains results of the fitting procedure and a detailed physical interpretation and discussion of the obtained results, including a comparison with the data obtained by CV measurements.

2.4 Publication IV

The underlying idea of this publication is to solve the long-standing problem of low CIC provided by microelectrodes coated with an insulating dielectric layer, which are commonly utilized for extracellular capacitive stimulation [46]. In publication IV, a new approach for bioelectronic interfacing of electrogenic cells or tissue is introduced, which utilizes a conductive microelectrode coated with an insulating ferroelectric layer. It is shown that the extracellular stimulation current density J_{stim} provided by the ferroelectric microelectrode is given by

$$J_{\mathrm{stim}} \;=\; C_s \frac{\partial}{\partial t} U(t) + \frac{\partial}{\partial t} P^{(\mathrm{FE})}(U(t)) \quad , \tag{2.9}$$

with the specific capacitance C_s and the ferroelectric polarization current $\partial P^{(\mathrm{FE})}/\partial t$, which acts as an additional contribution compared to the stimulation current provided by the common extracellular capacitive stimulation. Depending on the applied electric field strength $E(t) = U(t)/d$, two different regimes of the ferroelectric polarization current can be identified, which are separated by the coercive field E_{C} of the ferroelectric, i.e.

$$\frac{\partial}{\partial t} P^{(\mathrm{FE})}(E(t)) \;\equiv\; \begin{cases} J^{(\mathrm{SSW})}(t) & E < E_{\mathrm{C}} \\ J^{(\mathrm{SW})}(t) & E > E_{\mathrm{C}} \end{cases} \quad , \tag{2.10}$$

where $J^{(\mathrm{SSW})}(t)$ corresponds to the subswitching regime and $J^{(\mathrm{SW})}(t)$ to the switching regime of the ferroelectric. At subswitching fields, the ferroelectric displacement current density Eq. (2.9) in response to a harmonic ac electric field can contain higher harmonics due to the contribution from irreversible domain wall motion contained in $J^{(\mathrm{SSW})}(t)$ [64], which might be interesting for extracellular stimulation with low-frequency sinusoidal voltage signals [65]. Note, that the subswitching regime $E < E_{\mathrm{C}}$ of a ferroelectric can be analyzed in detail by domain wall pinning element modeling in combination with the extended Rayleigh analysis as described in Publication I + II.

However, the focus in the publication is on the ferroelectric switching regime $E > E_{\mathrm{C}}$. The corresponding switching kinetics is a very complex problem and there exist several models to explain the time-dependence of ferroelectric polarization reversal [66]. The traditional approach to explain the switching kinetics is the Kolmogorov-Avrami-Ishibashi (KAI)-model [67–69], which is based on the classical statistical theory of nucleation and predicts for the time-dependent change in ferroelectric polarization $\Delta P^{(\mathrm{FE})}(t)$ during switching between the bistable states $\pm P_{\mathrm{r}}$, the relationship [66]

$$\Delta P^{(\mathrm{FE})}(t) \;=\; 2P_{\mathrm{r}} \left\{1 - \exp[-(t/t_0)^n]\right\} \quad , \tag{2.11}$$

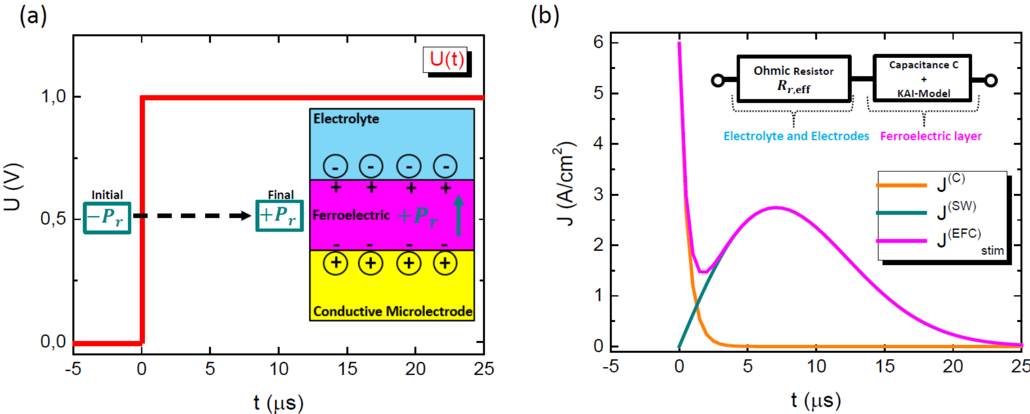

Figure 2.8: Voltage step with height $U_0 = 1$ V applied to the EFC configuration [cf. inset], to switch the remanent polarization from the initial state -P_r to the final state $+P_\mathrm{r}$. (b) Simulated extracellular current response during polarization reversal of the EFC configuration according to Eq. (2.14). Figure modified from appended publication IV; licensed under a Creative Commons Attribution (CC BY 4.0) license.

with the effective dimension n and the characteristic switching time t_0 as free parameters. For thin films, the effective dimension is $n = 2$ [66] and the time-dependence of the magnitude of the corresponding switching current density $J^{(\mathrm{SW})}(t)$ is then given by

$$|J^{(\mathrm{SW})}(t)| = 4P_\mathrm{r}(t/t_0^2)\exp[-(t/t_0)^2] \quad . \tag{2.12}$$

In publication IV, the time-dependent stimulation current density provided by a parallel-plate electrolyte–ferroelectric–conductor (EFC) configuration in the switching regime is then investigated. The EFC configuration is modeled by an equivalent-circuit, consisting of an Ohmic resistance – which represents the electrolyte and the electrodes – in series to a capacitance C in combination with the KAI-model, which models the ferroelectric layer of the EFC configuration. The Ohmic resistance can be approximated by the effective resistance $R_{r,\mathrm{eff}}$ for a circular microelectrode with radius r and an adjacent electrolyte with specific resistance ρ according to [61]

$$R_{r,\mathrm{eff}} = \frac{\rho}{\pi r} \quad . \tag{2.13}$$

The stimulation current density $J_\mathrm{stim}^\mathrm{EFC}(t)$ provided by the EFC configuration in response to an applied voltage step with height U_0, which induces polarization reversal from the initial state -P_r to the final state $+P_\mathrm{r}$ is then given

by

$$J_{\text{stim}}^{\text{EFC}}(t) = \frac{U_0}{r\rho} \exp[\frac{-t}{R_{r,\text{eff}}C}] + 4P_{\text{r}}(t/t_0^2) \exp[-(t/t_0)^2] \quad , \tag{2.14}$$

where the first term in Eq. (2.14) is the capacitive transient $J^{(\text{C})}(t)$.

The simulated stimulation current density in response to the applied voltage step with height $U_0 = 1$ V depicted in Fig. 2.8(a) is shown in Fig. 2.8(b), where the ferroelectric material properties correspond to a 9.5-nm-thick $Hf_{0.5}Zr_{0.5}O_2$ layer [27]. Here, the capacitive transient $J^{(\text{C})}(t)$ is superimposed by the bell-shaped switching current density $J^{(\text{SW})}(t)$, and the resulting CIC for complete switching during the stimulation time (i.e. $T_{\text{stim}} > t_0$) is given by [70]

$$\text{CIC} = C_s U_0 + 2P_{\text{r}} \quad , \tag{2.15}$$

which exhibits the additional contribution $2P_{\text{r}}$ compared to the CIC of microelectrodes with dielectric coating for extracellular capacitive stimulation [46]. Note that repetetive stimulation with a CIC according to Eq. (2.15) requires a subsequent voltage pulse of opposite polarity to reorient the remanent polarization P_{r} back to its initial state. This is not necessary for antiferroelectric materials or ferroelectrics in the paraelectric phase, where the remanent polarization is zero and which might be interesting alternatives for stimulation with solely unipolar voltage signals.

An interesting CMOS compatible material class for the fabrication of ferroelectric microelectrodes is $Al_{1-x}Sc_xN$, which exhibit ferroelectric properties with P_{r} up to 110 μC/cm^2 [71] resulting in a CIC above 200 μC/cm^2, which is in the range of previously reported stimulation-thresholds for small conductive microelectrodes (30 μm in diameter) [53] and which is approximately two orders of magnitude above the CIC of state-of-the-art capacitive microelectrodes [48–52]. Note, that the CIC of ferroelectric microelectrodes might be further increased by the fabrication of 3D structures [25].

The results pave the way to utilize ferroelectrics for long-term stable bioelectronic interfacing of electrogenic cells or tissue.

Author contributions to publication IV

I am the only author of this publication.

Chapter 3

Summary and outlook

In summary, this thesis provides solutions for two major problems. The first problem is the extraction of the domain-wall-motion induced amplitude- and frequency-dependent dielectric response $\varepsilon_r(E_0, f)$ in thin film ferroelectrics, embedded in a heterostructure e.g. a thin-film capacitor stack. Here, the introduced domain wall pinning element Z_{DW} allows one to extract $\varepsilon_r(E_0, f)$ from impedance spectroscopy measurements at different E_0 and subsequent equivalent-circuit fitting, which can be utilized to establish a link between thin film deposition parameters and film properties, in order to "tailor" ferroelectric films for their specific target application. Moreover, an extended Rayleigh analysis is presented in this thesis, which enables the quantification of the coupling strength between dielectric nonlinearity and frequency-dispersion in ferroelectric films and the identification of different domain-wall-motion regimes. In this thesis, this new approach is demonstrated by applying it to epitaxial and polycrystalline films of the promising lead-free ferroelectric BCZT grown by PLD on different substrates. However, it is clear that the presented approach is not restricted to the application to BCZT thin films alone. In fact, it is intended to serve as a guideline for future work on ferroelectric materials, which includes to reveal the effect of temperature and phase transitions [72], external bias fields [38], dopants [35], nanopatterning (without removal of material) by ion-bombardement [73–75] and substrate clamping [59] on domain wall dynamics and related material properties. This may provide new insights for the emerging field of domain boundary engineering [76] and is also of practical importance for many (new) applications in the sense of a More than Moore strategy. In this context, it is important to mention that the discovery of ferroelectricity in HfO_2-based thin films represents a real breakthrough due to the full CMOS compatibility of this material class and outstanding ferroelectric properties at the nanoscale [27, 77]. Thus, this material class is predestined for the fabrication of ferroelectric field-effect

transistors (FeFETs) for non-volatile memory applications [25] and/or for the integration into (novel) bioelectronic devices, which brings us to the second major problem treated in this thesis.

The second problem is the low CIC provided by microelectrodes coated with an insulating dielectric layer, which are utilized for extracellular capacitive stimulation in bioelectronic applications. Here, it is shown that a microelectrode coated with an insulating ferroelectric layer exhibits the ferroelectric polarization current as an additional contribution to the extracelluar stimulation current. Depending on the remanent polarization P_{r} of the ferroelectric, the polarization current in the switching regime can increase the CIC by up to two orders of magnitude as compared to the commonly used extracellular capacitive stimulation. Moreover, this approach also yields an addtional contribution to the stimulation current in the subswitching regime, where the polarization current originating from irreversible motion of ferroelectric domain walls can give rise to higher harmonics in the stimulation current [64] and might be interesting for extracellular stimulation with low-frequency sinusoidal voltage signals [65]. The subswitching regime of a ferroelectric layer can be analyzed by the domain wall pinning element in combination with the extended Rayleigh analysis introduced in this thesis. Irrespective of the ferroelectric operating regime, the presented approach paves the way to utilize ferroelectrics for bioelectronic interfacing of electrogenic cells or tissue. The resulting ferroelectric–neural interface is a promising approach for extracellular electrical stimulation without toxic electrochemical effects, which is crucial for implantable neuroprosthetic devices. Clearly, substantial work on ferroelectric–neural interfaces is needed to optimize thin film deposition parameters and to develop stimulus protocols for specific neuronal classes and for different ferroelectric materials with different remanent polarization and switching kinetics. Additional possibilities for future studies on ferroelectric–neural interfaces are extracellular electrical recordings by utilizing the ferroelectric layer as gate oxide of a FeFET, which polarization state is sensitive to extracellular potentials generated by adjacent neurons. This might result in the coupling of artificial neurons based on FeFETs [78] with biological neurons for future neuromorphic computing applications.

Moreover, the work on this thesis resulted in the invention of a piezoelectric membrane-microelectrode array (Publication VII) – a device for simultaneous electromechanical recording and stimulation of biological cells and tissue – and a ferroelectric biochip (Publication VIII), which is based on extracellular electrical stimulation by ferroelectric displacement current as introduced in Publication IV. The piezoelectric membrane-microelectrode array can be utilized, e.g., to study the excitation–contraction coupling in heart cells (cardiomyocytes) for *in vitro* drug testing and the ferroelectric

biochip can be utilized to provide bioelectronic interfaces in neuroprosthetic devices. Since both devices are based on ferroelectric films, impedance spectroscoy and domain wall pinning element modeling are useful methods to establish a link between thin film deposition parameters and film properties in order to optimize, e.g., the FOM Eq. (1.2) for the intrinsic signal-to-noise ratio of the invented piezoelectric membrane-microelectrode array.

In conclusion, this thesis is a first step towards the integration of thin-film ferroelectic oxides into bioelectronic devices such as high-resolution retinal implants or brain-machine interfaces and bridges the gap between the fields of oxide nanoelectronics and bioelectronics. In order to achieve further progress, the scientific communities of both fields need to bring together their expertise.

Danksagung

Ich möchte mich an dieser Stelle bei allen Menschen bedanken, welche mich während meiner Zeit als Doktorand begleitet und unterstützt haben. Innerhalb der letzten vier Jahre hatte ich das Glück, zahlreiche neue Leute kennenlernen zu dürfen und neue Freundschaften zu schließen, wodurch eine außergewöhnliche Zeit enstanden ist. Insgesamt sind es zu viele Menschen um alle namentlich zu nennen. Nicht unerwähnt bleiben sollen jedoch die folgenden Personen, welche ganz entscheidend zum Entstehen dieser Arbeit beigetragen haben.

Daher geht mein erster Dank an Prof. Dr. Dieter Kölle für die hervorragende wissenschafltiche Betreuung meiner Dissertation. Die gemeinsame Arbeit hat eine Menge Spaß gemacht und ich habe unheimlich viel von ihm gelernt. Danke Dieter!

Ebenfalls danken möchte ich Prof. Dr. Günther Zeck für viele interessante Gespräche und seine Bereitschaft das Zweitgutachten der vorliegenden Arbeit zu übernehmen.

Ein ganz besonderer Dank geht an Dr. Claus. J. Burkhardt für die tolle Unterstützung während meiner Promotion. Von den vielen gemeinsamen Diskussionen habe ich sehr profitiert und durch seinen Einsatz ist das Entstehen dieser Arbeit überhaupt erst möglich geworden. Danke Claus!

Zudem möchte ich mich bei Prof. Dr. Reinhold Kleiner für viele wichtige und hilfreiche Vorschläge bedanken, welche während unserer (Online-) Meetings entstanden sind.

Ein weiterer Dank geht an Dr. Markus Turad für seinen unermüdlichen Einsatz rund um alle möglichen Anlagen, Geräte und Techniken innerhalb und außerhalb des Reinraums.

Zum Schluss möchte ich mich bei meiner Familie bedanken. Hier möchte ich insbesondere meine Eltern hervorheben, deren bedingungslose Unterstützung mir immer bewusst war und mir ein sorgenfreies Studium inklusive Promotion ermöglicht hat, und denen daher diese Arbeit gewidmet ist.

Bibliography

[1] J. E. Lilienfeld, US Patent 1,745,175 (1930).

[2] G. E. Moore, Electronics **38**, 114 (1965).

[3] G. E. Moore, IEDM Tech. Digest , 11 (1975).

[4] E. Zrenner, K. U. Bartz-Schmidt, H. Benav, D. Besch, A. Bruckmann, V.-P. Gabel, F. Gekeler, U. Greppmaier, A. Harscher, S. Kibbel, J. Koch, A. Kusnyerik, T. Peters, K. Stingl, H. Sachs, A. Stett, P. Szurman, B. Wilhelm, and R. Wilke, Proc. R. Soc. B **278**, 1489 (2011).

[5] K. Mathieson, J. Loudin, G. Goetz, P. Huie, L. Wang, T. I. Kamins, L. Galambos, R. Smith, J. S. Harris, A. Sher, and D. Palanker, Nature Photonics **6**, 391 (2012).

[6] E. Musk, Neuralink, J. Med. Internet Res. **21**, 16194 (2019).

[7] W. Gao, S. Emaminejad, H. Y. Y. Nyein, S. Challa, K. Chen, A. Peck, H. M. Fahad, H. Ota, H. Shiraki, D. Kiriya, D.-H. Lien, G. A. Brooks, R. W. Davis, and A. Javey, Nature **529**, 509 (2016).

[8] T. D. Nguyen, N. Deshmukh, J. M. Nagarah, T. Kramer, P. K. Purohit, M. J. Berry, and M. C. McAlpine, Nature Nanotechnology **7**, 587 (2012).

[9] M. M. Waldrop, Nature **530**, 144 (2016).

[10] J. L. MacManus-Driscoll, M. P. Wells, C. Yun, J.-W. Lee, C.-B. Eom, and D. G. Schlom, APL Mater. **8**, 040904 (2020).

[11] S. Trolier-McKinstry and P. Muralt, J. Electroceram. **12**, 7 (2004).

[12] M. D. Nguyen, E. Houwman, M. Dekkers, D. Schlom, and G. Rijnders, APL Mater. **5**, 074201 (2017).

[13] A. Kursumovic, W.-W. Li, S. Cho, P. J. Curran, D. H. L. Tjhe, and J. L. MacManus-Driscoll, Nano Energy **71**, 104536 (2020).

[14] D. Damjanovic, Rep. Progr. Phys. **61**, 1267 (1998).

[15] D. Damjanovic, S. S. N. Bharadwaja, and N. Setter, Mat. Science and Eng. B **120**, 170 (2005).

[16] M. Acosta, N. Novak, V. Rojas, S. Patel, R. Vaish, J. Koruza, G. A. Rossetti, and J. Rödel, Appl. Phys. Rev. **4**, 041305 (2017).

[17] M. Tyunina, J. Phys.: Condens. Matter **18**, 5725 (2006).

[18] T. Nattermann, Y. Shapir, and I. Vilfan, Phys. Rev. B. **42**, 8577 (1990).

[19] A. A. Fedorenko, V. Mueller, and S. Stepanow, Phys. Rev. B **70**, 224104 (2004).

[20] T. Schenk, M. Hoffmann, M. Pesic, M. H. Park, C. Richter, U. Schroeder, and T. Mikolajick, Phys. Rev. Appl. **10**, 064004 (2018).

[21] R. Schmidt, W. Eerenstein, T. Winiecki, F. D. Morrison, and P. A. Midgley, Phys. Rev. B **75**, 245111 (2007).

[22] R. Schmidt, J. Ventura, E. Langenberg, N. M. Nemes, C. Munuera, M. Varela, M. Garcia-Hernandez, C. Leon, and J. Santamaria, Phys. Rev. B **86**, 035113 (2012).

[23] W. Liu and X. Ren, Phys. Rev. Lett. **103**, 257602 (2009).

[24] R. Waser, U. Böttger, and S. T. (Ed.), *Polar Oxides*, 1st ed. (Wiley, New York, 2005).

[25] M. H. Park, Y. H. Lee, T. Mikolajick, U. Schroeder, and C. S. Hwang, MRS Communications **8**, 795 (2018).

[26] H. Yan, F. Inam, G. Viola, H. Ning, H. Zhang, Q. Jiang, T. Zeng, Z. Gao, and M. J. Reece, J. Adv. Dielectrics **1**, 107 (2011).

[27] J. Müller, T. S. Böschke, D. Bräuhaus, U. Schröder, U. Böttger, J. Sundqvist, P. Kücher, T. Mikolajick, and L. Frey, Appl. Phys. Lett. **99**, 112901 (2011).

[28] S. L. Miller, J. R. Schwank, R. D. Nasby, and M. S. Rodgers, J. Appl. Phys. **70**, 2849 (1991).

[29] R. Resta, Ferroelectrics **136**, 51 (1992).

[30] R. Resta and D. Vanderbilt, Topics Appl. Physics **105**, 31 (2007).

[31] M. Dommermuth and N. Schopohl, J. Phys. Commun. **2**, 075012 (2018).

[32] D. A. Hall, Ferroelectrics **223**, 319 (1999).

[33] V. Mueller, H. Beige, and H. P. Abicht, Appl. Phys. Lett. **84**, 1341 (2004).

[34] N. Bassiri-Gharb and S. Trolier-McKinstry, J. Appl. Phys. **97**, 064106 (2005).

[35] L. Yang, H. Fang, L. Zheng, J. Du, L. Wang, X. Lu, W. Lü, R. Zhang, and W. Cao, Appl. Phys. Lett. **114**, 232901 (2019).

[36] D. Damjanovic, J. Appl. Phys. **82**, 1788 (1997).

[37] D. V. Taylor and D. Damjanovic, J. Appl. Phys. **82**, 4 (1997).

[38] N. Bassiri-Gharb, I. Fujii, E. Hong, S. Trolier-McKinstry, D. V. Taylor, and D. Damjanovic, J. Electroceram. **19**, 49 (2007).

[39] S. F. Cogan, Annu. Rev. Biomed. Eng. **10**, 275 (2008).

[40] A. Kral, M. F. Dorman, and B. S. Wilson, Annu. Rev. Neurosci. **42**, 47 (2019).

[41] S. Miocinovic, S. Somayajula, S. Chitnis, and J. Vitek, JAMA Neurol. **70**, 163 (2013).

[42] A. Stett, U. Egert, E. Guenther, F. Hofmann, T. Meyer, W. Nisch, and H. Haemmerle, Anal. Bioanal. Chem. **377**, 486 (2003).

[43] U. Frey, U. Egert, F. Heer, S. Hafizovic, and A. Hierlemann, Biosensors and Bioelectronics **24**, 2191 (2009).

[44] J. Maeng, B. Chakraborty, N. Geramifard, T. Kang, R. T. Rihani, A. Joshi-Imre, and S. F. Cogan, J. Biomed. Mater. Res. **108B**, 880 (2019).

[45] D. R. Merrill, M. Bikson, and J. G. R. Jefferys, J. Neurosci. Methods **141**, 171 (2005).

[46] P. Fromherz and A. Stett, Phys. Rev. Lett. **75**, 1670 (1995).

[47] P. Fromherz, A. Offenhäusser, T. Vetter, and J. Weis, Science **252**, 1290 (1991).

[48] G. Bertotti, D. Velychko, N. Dodel, S. Keil, D. Wolansky, B. Tillak, M. Schreiter, A. Grall, P. Jesinger, S. Röhler, M. Eickenscheidt, A. Stett, A. Möller, K.-H. Boven, G. Zeck, and R. Thewes, IEEE BioCAS Proceedings , 304 (2014).

[49] F. Wallrapp and P. Fromherz, J. Appl. Phys. **99**, 114103 (2006).

[50] I. Schoen and P. Fromherz, Biophysical Journal **92**, 1096 (2007).

[51] M. Eickenscheidt, M. Jenkner, R. Thewes, P. Fromherz, and G. Zeck, J. Neurophysiol. **107**, 2742 (2012).

[52] M. Dollt, M. Reh, M. Metzger, G. Heusel, M. Kriebel, V. Bucher, and G. Zeck, Front. Neurosci. **14**, 552876 (2020).

[53] A. Corna, T. Herrmann, and G. Zeck, J. Neural Eng. **15**, 045003 (2018).

[54] R. Gerhardt, J. Phys. Chem. Solids **55**, 1491 (1994).

[55] D. Su, Q. Meng, C. A. F. Vaz, M.-G. Han, Y. Segal, F. J. Walker, M. Sawicki, C. Broadbridge, and C. H. Ahn, Appl. Phys. Lett. **99**, 102902 (2011).

[56] T. Nattermann, V. Pokrovsky, and V. M. Vinokur, Phys. Rev. Lett. **87**, 197005 (2001).

[57] J. R. Macdonald and E. Barsoukov, *Impedance Spectroscopy*, 3rd ed. (Wiley, New York, 2018).

[58] C. Ma, B. Ma, S.-B. Mi, L. Liu, and J. Wu, Appl. Phys. Lett. **104**, 162902 (2014).

[59] F. Griggio, S. Jesse, A. Kumar, O. Ovchinnikov, T. N. Jackson, D. Damjanovic, S. V. Kalinin, and S. Trolier-McKinstry, Phys. Rev. Lett. **108**, 157604 (2012).

[60] X. Kang, J. Liu, H. Tian, B. Yang, Y. N. Li, and C. Yang, Sensors and Actuators B **225**, 267 (2016).

[61] Z. Chen, L. Ryzhik, and D. Palanker, Phys. Rev. Applied **13**, 014004 (2020).

[62] M. Balabajew and B. Roling, Electrochim. Acta **176**, 907 (2015).

[63] V. F. Lvovich, *Impedance Spectroscopy: Applications to Electrochemical and Dielectric Phenomena*, 1st ed. (Wiley, New Jersey, 2012).

[64] S. Miga, J. Dec, and W. Kleemann, Rev. Sci. Instrum. **78**, 033902 (2007).

[65] D. K. Freeman, D. K. Eddington, J. F. R. III, and S. I. Fried, J. Neurophysiol. **104**, 2778 (2010).

[66] J. Y. Jo, H. S. Han, J.-G. Yoon, T. K. Song, S.-H. Kim, and T. W. Noh, Phys. Rev. Lett. **99**, 267602 (2007).

[67] A. N. Kolmogorov, Bull. Acad. Sci. USSR Math. Ser. **3**, 355 (1937).

[68] M. Avrami, J. Chem. Phys. **7**, 1103 (1939).

[69] Y. Ishibashi and Y. Takagi, J. Phys. Soc. Jpn. **31**, 506 (1971).

[70] D. Damjanovic, Rep. Progr. Phys. **61**, 1267 (1998).

[71] S. Fichtner, N. Wolff, F. Lofink, L. Kienzle, and B. Wagner, J. Appl. Phys. **125**, 114103 (2019).

[72] A. Piorra, V. Hrkac, N. Wolff, C. Zamponi, V. Duppel, J. Hadermann, L. Kienle, and E. Quandt, J. Appl. Phys. **125**, 244103 (2019).

[73] S. Saremi, R. Xu, F. I. Allen, J. Maher, J. C. Agar, R. Gao, P. Hosemann, and L. W. Martin, Phys. Rev. Mat. **2**, 084414 (2018).

[74] S. Saremi, J. Kim, A. Ghosh, D. Meyers, and L. W. Martin, Phys. Rev. Lett. **123**, 207602 (2019).

[75] J. Kim, S. Saremi, M. Acharya, G. Velarde, E. Parsonnet, P. Donahue, A. Qualls, D. Garcia, and L. W. Martin, Science **369**, 81 (2020).

[76] E. K. H. Salje, Phase Transitions **86**, 2 (2013).

[77] Y. Wei, P. Nukala, M. Salverda, S. Matzen, H. J. Zhao, J. Momand, A. S. Everhardt, G. Agnus, G. R. Blake, P. Lecoeur, B. J. Kooi, J. Íñiguez, B. Dkhil, and B. Noheda, Nature Materials **17**, 1095 (2018).

[78] H. Mulaosmanovic, E. Chicca, M. Bertele, T. Mikolajick, and S. Slesazeck, Nanoscale **10**, 21755 (2018).

Appended publications

Publication I

Reproduced from M. Becker *et al.*, arXiv:2008.04786v2 [cond-mat.mtrl-sci] (2021)

Impedance spectroscopy of ferroelectrics: The domain wall pinning element

M. Becker,[1, 2, *] C. J. Burkhardt,[1] R. Kleiner,[2] and D. Koelle[2]

[1] *NMI Natural and Medical Sciences Institute at the University of Tübingen, Markwiesenstr. 55, 72770 Reutlingen, Germany*

[2] *Physikalisches Institut, Center for Quantum Science (CQ) and LISA$^+$, University of Tübingen, Auf der Morgenstelle 14, 72076 Tübingen, Germany*

(Dated: March 10, 2021)

We introduce an equivalent-circuit element based on the theory of interface pinning in random systems, to analyze the contribution of domain wall motion below the coercive field to the impedance of a ferroelectric, as a function of amplitude E_0 and frequency f of an applied ac electric field. We investigate capacitor stacks, containing ferroelectric $0.5(Ba_{0.7}Ca_{0.3})TiO_3$–$0.5Ba(Zr_{0.2}Ti_{0.8})O_3$ (BCZT) thin films, epitaxially grown by pulsed laser deposition on Nb-doped $SrTiO_3$ single crystal substrates and covered with Au electrodes. Impedance spectra from $f = 10\,\mathrm{Hz}$ to $1\,\mathrm{MHz}$ were collected at different E_0. Deconvolution of the spectra is achieved by fitting the measured impedance with an equivalent-circuit model of the capacitor stacks, and we extract the domain-wall-motion induced amplitude- and frequency-dependent dielectric response of the BCZT films from the obtained fit parameters. From an extended Rayleigh analysis, we quantify the coupling strength between dielectric nonlinearity and dielectric dispersion in the BCZT films and identify different domain-wall-motion regimes. Finally, we construct a schematic diagram of the different domain-wall-motion regimes and discuss the corresponding domain-wall dynamics.

arXiv:2008.04786v2 [cond-mat.mtrl-sci] 9 Mar 2021

I. INTRODUCTION

Domain wall motion in ferroelectric materials does not only influence their ferroelectric, but also their dielectric and piezoelectric properties [1]. In general, the complex dynamics of domain wall displacement in ferroelectrics results in a dependence of their dielectric (ε_{ij}) and piezoelectric (d_{ijk}) tensor components on the amplitude E_0 and frequency f of an applied ac electric field [1, 2].

Regarding perovskite-type ferroelectrics, field and frequency dependent dielectric and piezoelectric response has been mostly investigated in ceramics and thin films based on $PbZr_xTi_{1-x}O_3$ (PZT) [1–4]. It was found, that the field dependence of permittivity and piezoelectric coefficients at subswitching fields can often be described by the linear Rayleigh law, which results in a nonlinear and hysteretic dielectric polarization and piezolectric strain. Based on this, the linear field dependence of permittivity is also referred to as dielectric nonlinearity [4]. Moreover, the coupling of dielectric nonlinearity and frequency dispersion has been studied [2]. However, a unified theory which describes the field and frequency behavior of material properties, e.g. the complex relative permittivity $\varepsilon_r(E_0, f)$ of ferroelectrics, with the same set of equations is not available. Thus, the measurement of $\varepsilon_r(E_0, f)$ is crucial, since the permittivity is directly related to the microstructure of the material and essential for device modelling [1, 5]. This is especially true for thin film samples of new and thus less investigated lead-free ferroelectrics such as $K_{0.5}Na_{0.5}NbO_3$ (KNN) and $0.5(Ba_{0.7}Ca_{0.3})TiO_3$–$0.5Ba(Zr_{0.2}Ti_{0.8})O_3$ (BCZT) [6, 7].

Recently, a new method for the analysis of the field dependence of complex relative permittivity $\varepsilon_r(E_0)$ (i.e. Rayleigh analysis) was introduced [8]. This method is based on impedance spectroscopy and equivalent-circuit fitting, which allows one to discriminate different contributions to the permittivity, originating from electronically different components (electrodes, eletrode/ferroelectric interfaces and ferroelectric) of the analyzed thin film devices.

In thin film capacitor stacks, with a ferroelecric placed between two metallic electrodes, the dielectric properties can exhibit strong frequency dispersion depending on the resistivity of both, the ferroelectric film and the electrode layers [9], thus masking the true dielectric dispersion of the ferroelectric caused by pinning of domain walls on randomly distributed defects occuring in the ferroelectric layer inside the heterostructure [10, 11]. Moreover, the interfaces to the electrodes play a more crucial role in thin films as compared to thick ceramic samples [8, 12], which can lead to extrinsic dielectric relaxation processes [13], additionally masking the contributions from the ferroelectric.

The superiority of the Rayleigh analysis based on impedance spectroscopy over the conventional approach (i.e. without equivalent-circuit fitting) was demonstrated in Ref. 8 for the measurement of $\varepsilon_r(E_0)$ for a ferroelectric Si:HfO_2 thin film. However, the frequency dispersion $\varepsilon_r(f)$ is not accessible with the method described in Ref. 8.

In this work, we introduce an equivalent-circuit element with impedance Z_{DW} which is based on the theory of interface pinning in random systems [10] and models the frequency-dependent impedance response of a ferroelectric including the domain-wall-motion induced contribution. Moreover, we report on a method to extract the domain-wall-motion induced amplitude- and frequency-dependent dielectric response $\varepsilon_r(E_0, f)$ in thin film ferroelectrics, embedded in a thin film capacitor stack, from impedance spectroscopy measurements at different E_0

* maximilian.becker@nmi.de

and equivalent-circuit fits with the introduced element Z_{DW}. Finally, we present an extended Rayleigh analysis which allows one to quantify the coupling strength between dielectric nonlinearity and frequency dispersion and the identification of different domain-wall-motion regimes. Our approach will be demonstrated by applying it to thin film capacitor stacks containing the lead-free ferroelectric BCZT.

II. THEORY

A. Rayleigh behavior and interface pinning in random systems

Domain wall dynamics below the coercive field E_{C} of a ferroelectric can be considered as a superposition of center of mass motion and relaxational motion of internal modes, i.e. domain wall segments [11]. From theory it is known, that the interaction of domain walls with pinning centers, that form a random energy landscape, gives rise to the so called Rayleigh behavior and the corresponding Rayleigh law [14, 15]. Rayleigh behavior originates from the irreversible center of mass motion of domain walls and results in a linear dependence of permittivity and piezoelectric coefficients on the field amplitude E_0 above a specific threshold field E_{T} and below the coercive field E_{C}, which was also observed experimentally on ceramic and thin film samples [4, 16–18]. As a consequence of Rayleigh behavior, the dielectric polarization and piezoelectric strain responses of ferroelectrics become nonlinear in E_0 and hysteretic even at subswitching fields $E_{\mathrm{T}} < E_0 < E_{\mathrm{C}}$. In the following, we will solely discuss dielectric properties and disregard piezoelectric properties.

The Rayleigh law for the real and imaginary parts of the complex relative permittivity $\varepsilon_r = \varepsilon_r' - i\varepsilon_r''$ is given by [8, 18]

$$\begin{aligned} \varepsilon_r'(E_0) &= \varepsilon_{r,\mathrm{in}}' + \alpha' E_0 \quad , \\ \varepsilon_r''(E_0) &= \varepsilon_{r,\mathrm{in}}'' + \alpha'' E_0 \quad . \end{aligned} \tag{1}$$

Here $\varepsilon_{r,\mathrm{in}}'$ and $\varepsilon_{r,\mathrm{in}}''$ are real and imaginary parts of the reversible (initial) Rayleigh parameter $\varepsilon_{r,\mathrm{in}}$ due to lattice and reversible domain wall contributions, α' denotes the irreversible Rayleigh parameter (Rayleigh constant) and $\alpha'' = \frac{4}{3\pi}\alpha'$.

In the following, we will denote a general linear field dependene of $\varepsilon_r'(E_0)$ and $\varepsilon_r''(E_0)$ with positive slope as "Rayleigh-like behavior". In that sense, the Rayleigh law is a special case of Rayleigh-like behavior with the additional requirement $\alpha'' = \frac{4}{3\pi}\alpha'$.

The irreversible domain wall contribution to the real part of the permittivity is given by $\alpha' E_0$. It turns out, that α' is a direct and quantitative measure for the mobility of domain walls, and it is dependent on the concentration of pinning centers, film thickness and the density of domain walls [4]. However, the Rayleigh law Eq. (1) is rate-independent and no frequency dependence of material properties can be derived from it [2–4].

Theory predicts for domain wall pinning processes in random systems a logarithmic dependence of permittivity on frequency f, which is due to the relaxational contribution of internal modes [10, 11]

$$\begin{aligned} \varepsilon_r'(f) &\propto \left[\ln\left(\frac{1}{2\pi f t_0}\right)\right]^{\Theta} \quad , \\ \varepsilon_r''(f) &\propto \left[\ln\left(\frac{1}{2\pi f t_0}\right)\right]^{\Theta-1} \quad . \end{aligned} \tag{2}$$

Here, Θ is related to the roughness of the domain wall and t_0 denotes a microscopic time constant, which is related to the rate of transitions of domain wall segments between metastable states [10, 11].

In this pinned regime, the center of mass of the domain wall is captured in a potential valley, while domain wall segments can still jump between different metastable states with close energies. The potential valley of a random energy landscape can be described by [11]

$$U(\bar{r}) = \frac{C_n}{2\tau_1}\bar{r}^2 + \int_0^{\bar{r}} dr'\bar{g}(r') \quad , \tag{3}$$

with a constant C_n, the transverse spatial coordinate $\bar{r}$, a single relaxation time τ_1 and the random pinning force g. The first term in Eq. (3) describes the average (parabolic) shape of the well and the second term describes spatial fluctuations due to the residual part of the random pinning force g. This term is important, because it results in a distribution of relaxation times $\Psi_1(\tau)$ instead of the single relaxation time τ_1 [11]. As a consequence, the dielectric response of a ferroelectric due to domain wall pinning in a random energy landscape is not expected to exhibit a Debye-like dielectric relaxation with a single relaxation time and hence one dominant relaxation frequency.

In many ferroelectrics - including relaxors - it was found that $\Theta \sim 1$, which corresponds to a frequency-independent imaginary part of permittivity, and which is valid for systems with a broad distribution $\Psi_1(\tau)$ of relaxation times [2–4, 19–21]. In this case, the logarithmic frequency dependence of the complex relative permittivity can be well approximated by the expression [2, 3, 20, 21]

$$\begin{aligned} \varepsilon_r'(f) &= \varepsilon_{r,0}' + \Delta\varepsilon_r' \ln\left(\frac{1\,\mathrm{Hz}}{2\pi f}\right) \quad , \\ \varepsilon_r''(f) &= \varepsilon_{r,0}'' \quad , \end{aligned} \tag{4}$$

where $\varepsilon_{r,0}'$ and $\varepsilon_{r,0}''$ denote static contributions to the permittivity, and $\Delta\varepsilon_r'$ is the logarithmic dispersion strength. We note that in Eq. (4) we fixed the value of t_0 to 1s, which is also the common choice in the literature [4, 19–22]. We will use this convention throughout the remaining part of this paper.

It has been shown for systems with Rayleigh-like behavior and logarithmic frequency dispersion, that the frequency dependence of ε_r' in Eq. (4) is due to the logarithmic frequency dependence of both reversible ($\varepsilon_{r,\mathrm{in}}'$)

and irreversible (α') Rayleigh parameters defined in the Rayleigh law Eq. (1), which can then be expressed as [19]

$$\varepsilon'_{r,\mathrm{in}}(f) = \varepsilon'_{r,\mathrm{in},0} + \Delta\varepsilon'_{r,\mathrm{in}} \ln\left(\frac{1\,\mathrm{Hz}}{2\pi f}\right) \quad ,$$
$$\alpha'(f) = \alpha'_0 + \Delta\alpha' \ln\left(\frac{1\,\mathrm{Hz}}{2\pi f}\right) \quad . \tag{5}$$

The physical interpretation of the coefficients $\Delta\varepsilon'_{r,\mathrm{in}}$ and $\Delta\alpha'$ in Eq. (5) will be discussed later in Sec. IV. As a consequence, the Rayleigh relation for the real part of relative permittivity ε'_r in Eq. (1), can be written with frequency-dependent Rayleigh parameters given by Eq. (5), as

$$\varepsilon'_r(E_0, f) = \varepsilon'_{r,\mathrm{in}}(f) + \alpha'(f)E_0 \quad . \tag{6}$$

However, the Rayleigh law Eq. (1), comprises also the Rayleigh relation for the imaginary part of relative permittivity ε''_r and the relations are coupled by $\alpha'' = \frac{4}{3\pi}\alpha'$. The coupling relation predicts a logarithmic frequency dependence of α'' which results in a frequency dispersion of ε''_r, which is contradictory to the assumption of a frequency independent imaginary part given by Eq. (4), which implies a constant α''. Thus, the logarithmic frequency dispersion due to domain wall pinning in random systems and the Rayleigh law are only compatible at a fixed frequency. Taking account of a constant α'', we can implicitly define this frequency $f \equiv f_\mathrm{R}$ by

$$\lim_{f\to f_\mathrm{R}} \frac{\alpha'(f)}{\alpha''} \stackrel{!}{=} \frac{3\pi}{4} \quad . \tag{7}$$

At $f = f_\mathrm{R}$, the Rayleigh law is fulfilled for variable field amplitudes E_0 within the Rayleigh region. The frequency f_R will be called the "Rayleigh frequency" in the following.

The more general Rayleigh-like behavior exists in the frequency range where $\alpha'(f)$ is positive. At frequencies f within this Rayleigh-like frequency range, the center of mass of domain walls can move irreversibly via hopping between different minima of the energy landscape, since this is a basic assumption in the derivation of the Rayleigh law. Thus, the center of mass of the domain walls is not captured in a potential valley as in the pinned regime and we conclude that the Rayleigh-like frequency range corresponds to a regime with coexisting center of mass motion and relaxational motion of internal modes. In analogy to Ref. 11, we will denote this regime as the stochastic regime of complex relative permittivity.

B. Derivation of an equivalent-circuit element based on interface pinning in random systems

In an impedance spectroscopy experiment, the complex impedance $Z(f) = Z'(f) - iZ''(f)$ is measured as a function of frequency f, typically in the range of $f = 10 - 10^6$ Hz. The complex impedance is related to the complex relative permittivity by [23]

$$Z(f) = \frac{1}{i2\pi f C_0 \varepsilon_r(f)} \quad , \tag{8}$$

with the geometrical capacitance C_0. For a parallel-plate capacitor, $C_0 = \frac{\varepsilon_0 A}{d}$ with the vacuum permittivity ε_0, electrode area A and plate distance d. Separating real and imaginary parts in Eq. (8), yields

$$Z(f) = \frac{\varepsilon''_r(f) - i\varepsilon'_r(f)}{2\pi f C_0 \left\{\varepsilon'_r(f)^2 + \varepsilon''_r(f)^2\right\}} \quad . \tag{9}$$

By inserting the logarithmic frequency dependence Eq. (4) into Eq. (9), we obtain the equivalent-circuit element Z_DW, which models the impedance of a ferroelectric due to pinning of domain walls in a potential valley [c.f. Eq. (3)] of a random energy landscape

$$Z_\mathrm{DW}(f) = \frac{\varepsilon''_{r,0} - i\left[\varepsilon'_{r,0} + \Delta\varepsilon'_r \ln\left(\frac{1\,\mathrm{Hz}}{2\pi f}\right)\right]}{2\pi f C_0 \left\{\left[\varepsilon'_{r,0} + \Delta\varepsilon'_r \ln\left(\frac{1\,\mathrm{Hz}}{2\pi f}\right)\right]^2 + \varepsilon''^2_{r,0}\right\}}, \tag{10}$$

with $\varepsilon'_{r,0}$, $\varepsilon''_{r,0}$ and $\Delta\varepsilon'_r$ as free parameters. Consequently, Z_DW will be called the "domain wall pinning element" in the following.

Impedance spectroscopy allows one to extract the free parameters $\varepsilon'_{r,0}$, $\varepsilon''_{r,0}$ and $\Delta\varepsilon'_r$ by fitting the measured impedance over the full frequency range to the impedance of an appropriate equivalent-circuit model of the capacitor stack, including the ferroelectric. Since domain wall pinning occurs solely in the ferroelectric layer and not in the electrodes and interfaces, the impedance response of electrodes and interfaces do not exhibit the characteristic logarithmic frequency dispersion over the measured frequency range and hence can be discriminated by their different frequency dispersion from the domain wall pinning element which models the ferroelectric layer. Thus, the different contributions (from electrodes, interfaces and the ferroelectric layer) to the measured impedance of the capacitor stack are deconvoluted, by equivalent-circuit fitting with the domain wall pinning element.

Measurements at different excitation field amplitudes E_0 then allow one to determine the field dependence of the dispersion parameters $\varepsilon'_{r,0}(E_0)$, $\varepsilon''_{r,0}(E_0)$ and $\Delta\varepsilon'_r(E_0)$. Subsequently, the field- and frequency-dependent dielectric response $\varepsilon_r(E_0, f)$ of the ferroelectric is obtained by inserting the field-dependent dispersion parameters into Eq. (4). For comparison, the conventional approach for the analysis of complex relative permittivity measurements is described in appendix A.

Note that for systems in which the assumption of a broad distribution of relaxation times and/or $\Theta \sim 1$ is not fulfilled, similar equivalent-circuit elements can be obtained by inserting the corresponding frequency dispersion into Eq. (9).

III. EXPERIMENTAL

A ceramic BCZT target was used to grow 200-nm-thick epitaxial single crystalline films on (001)-oriented Nb-doped (0.5 wt%) $SrTiO_3$ (Nb:STO) single crystal by means of pulsed laser deposition (PLD). We used a 248 nm KrF excimer laser with an energy of 110 mJ and 5 Hz repetition rate. For the deposition on Nb:STO substrates, the temperature was fixed at 700 °C with an oxygen partial pressure $p_{O_2} = 0.1$ mbar. After deposition, the films were heated up to 800 °C and kept there for 15 minutes before cooling down to 700 °C. Subsequently, p_{O_2} was increased to 5 mbar and the films were cooled down to room temperature with a rate of 10 K/min.

The microstructure of the films was investigated by x-ray diffraction (XRD) to obtain the crystallographic orientation and to check for possible secondary phases. One sample was further analyzed by scanning transmission electron microscopy (STEM) to investigate possible crystal defects in BCZT, which may act as domain wall pinning-centers.

For electrical measurements, 3-mm diameter disc-shaped Au electrodes (∼100-nm-thick) were deposited on top of the BCZT films by electron beam evaporation through a shadow mask. Impedance spectra of the capacitor stack from $f = 10$ Hz to 1 MHz were collected at different excitation field amplitudes E_0 using a Solartron 1260 impedance analyzer together with a probe station. For each measurement, E_0 was successively increased from 2.5 to 25 kV/cm (applied root mean square voltage $V_{\mathrm{RMS}} = 0.05 - 0.5$ V) with a step-size of 1.25 kV/cm, which results in the measurement of the impedance under 19 different E_0.

IV. RESULTS AND DISCUSSION

In this section, we present XRD data and results from electrical measurements from one representative epitaxial BCZT device. The STEM results were obtained from a different epitaxial BCZT device which was fabricated with the same process parameters (see Sec. III).

A. XRD and STEM

Figure 1 shows the XRD $\theta - 2\theta$ diffraction pattern for a BCZT thin film deposited on a (001)-oriented Nb:$SrTiO_3$ (Nb:STO) single crystal. No traces of secondary phases are observable. The structural phase diagram of BCZT shows four possible crystallographic phases, i.e. cubic, tetragonal, orthorhombic and rhombohedral [24]. Due to the small variations in the lattice parameters of the possible phases, a rigorous specification of the crystallographic phase of the films is not accessible from the XRD data. Thus, we denote the film structure as pseudo-cubic, which represents the four possible phases. For simplicity, we use cubic metrics for the Miller indices and crystal directions. The film grown on a Nb:STO substrate is epitaxial and the full width half maximum (FWHM) of the rocking curve of the (002)-BCZT peak (inset in Figure 1) has a value of $\omega = 0.08\,°$, indicating high crystalline quality of the film. The results are in good agreement with BCZT thin films grown by PLD on undoped STO [25] and $SrRuO_3$ coated STO [26].

The epitaxial growth of BCZT on Nb:STO was also confirmed by STEM. Moreover, our STEM analysis revealed the occurrence of edge-type misfit dislocations at the epitaxial Nb:STO/BCZT interface, characterized by the Burgers vector $\boldsymbol{b} = a[100]$. Here, a denotes the lattice constant along the [100] direction within the BCZT unit cell (Fig. 2). These misfit dislocations act as possible domain wall pinning centers, which was already observed in similar epitaxial PZT heterostructures [27].

B. Impedance spectroscopy and equivalent-circuit analysis

Collected impedance spectroscopy data (for a selection of three different E_0) on the epitaxial device are shown in Fig. 3(a). A validation procedure to rule out artifacts in the measured impedance spectra is given in appendix B. The equivalent circuit depicted in Fig. 3(b) was used to fit the collected impedance spectra [28]. Here the series resistance R_0 corresponds to the resistance of the cables, measurement probes and the electrodes. The R_1C_1-Element represents the electrode-BCZT interfaces. The resistance R_2 and Z_{DW} model the ferroelectric film inside the capacitor stack. R_2 is attributed to losses due to possible leakage currents, whereas the losses due to domain wall motion are contained in Z_{DW}. Additionally, the dispersion parameters are contained in the domain wall pinning element. The element L_0 models the inductance of the cables used. Results of the fits can be seen in the Bode plot [29] shown in Fig. 3(a) where the real and the imaginary part of the impedance $Z = Z' - iZ''$

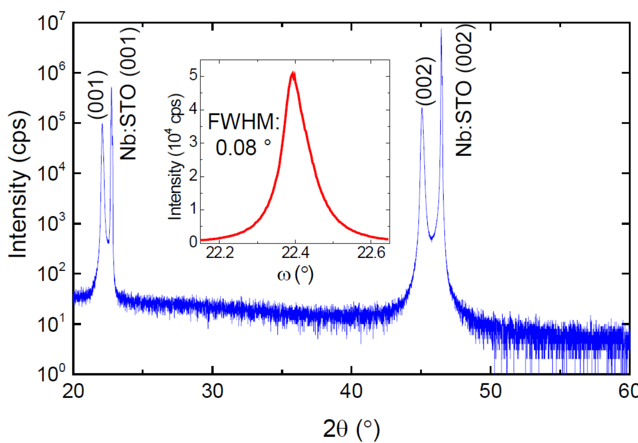

FIG. 1. XRD $\theta - 2\theta$ scan of BCZT thin film on Nb:STO. The inset shows the rocking curve of the (002) BCZT peak.

TABLE I. Fit parameters for the epitaxial BCZT capacitor stack at three different excitation field amplitudes E_0. The estimated standard errors for R_2 are below 1 kΩ.

E_0 (kV/cm)	R_0 (Ω)	R_1 (Ω)	C_1 (nF)	R_2 (MΩ)	$\varepsilon'_{r,0}$	$\Delta\varepsilon'_r$	$\varepsilon''_{r,0}$	(μH)
2.5	18 ± 1	2889 ± 4	150.5 ± 0.3	29	457.9 ± 0.2	7.27 ± 0.04	10.65 ± 0.03	4.8 ± 0.8
12.5	16 ± 1	2880 ± 3	151.8 ± 0.2	21	493.7 ± 0.1	8.41 ± 0.03	13.23 ± 0.02	5.3 ± 0.5
22.5	14 ± 3	2838 ± 7	155.1 ± 0.6	13	526.4 ± 0.4	11.41 ± 0.09	18.23 ± 0.07	5.3 ± 1.4

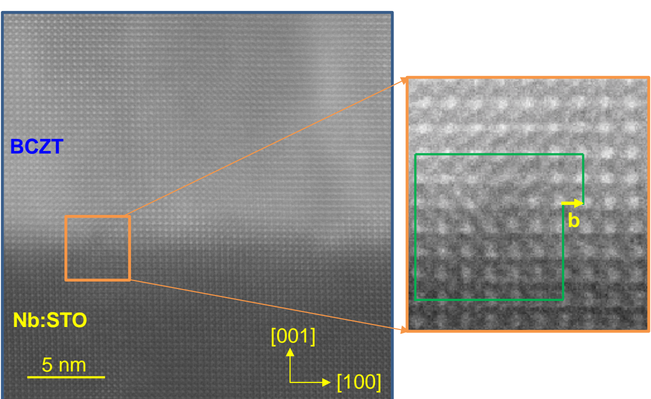

FIG. 2. Cross-section STEM image of Nb:STO/BCZT interface viewed along the [010] zone axis. The enlarged section shows an edge-type misfit dislocation with Burgers vector $\boldsymbol{b} = a[100]$.

are plotted vs frequency (for three values of E_0). An additional logarithmic Bode plot of the fits is given in appendix C. In all cases, the fits are in good agreement with the measured data, indicating that the utilized equivalent circuit is a suitable model for the thin film capacitors. Fit parameters obtained from equivalent-circuit fits at three different excitation field amplitudes are summarized in Table I. The standard errors are calculated from maximum likelihood estimation [30].

Subsequently, the complex relative permittivity $\varepsilon_r(f)$ of the BCZT film (i.e., without contributions from the electrodes and ferroelectric/electrode interfaces) was calculated from the obtained fit parameters according to Eq. (4) for each field amplitude E_0. The results for a selection of three different excitation field amplitudes are depicted in Fig. 4. We clearly observe [c.f. Fig. 4 and Table I] that $\varepsilon_r(f)$ and the parameters $\varepsilon'_{r,0}$, $\varepsilon''_{r,0}$ and $\Delta\varepsilon'_r$ depend on the field amplitude E_0, which indicates that dielectric nonlinearity and frequency dispersion are coupled in the BCZT films.

C. Extended Rayleigh analysis

From the equivalent-circuit fits, the field dependence of the dispersion parameters $\varepsilon'_{r,0}(E_0)$, $\varepsilon''_{r,0}(E_0)$ and $\Delta\varepsilon'_r(E_0)$ can be extracted and the results are depicted in Fig. 5.

We observe that all dispersion parameters exhibit a linear dependence on the field amplitude E_0, i.e. in the

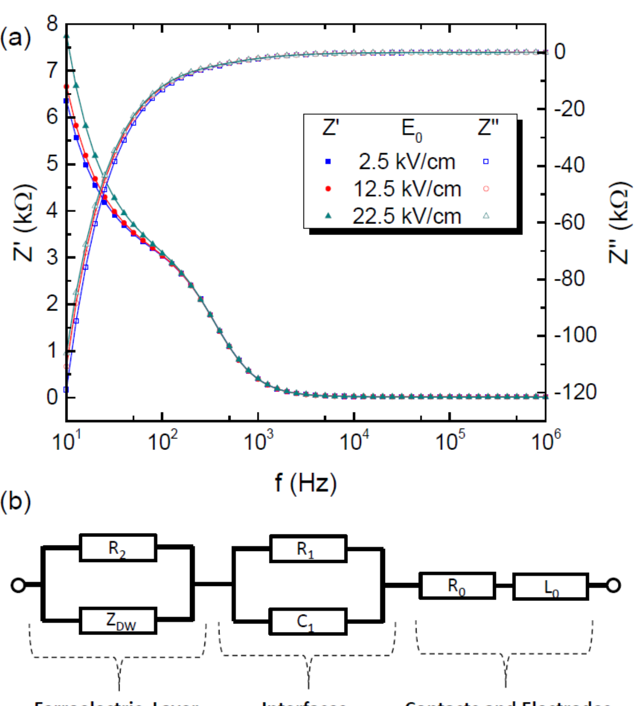

FIG. 3. (a) Bode plots $Z'(f)$ and $Z''(f)$ obtained by impedance spectroscopy (symbols) for a selection of different E_0 on epitaxial BCZT thin film capacitor. The equivalent circuit in (b) was used to fit the data (solid lines).

guise of the following linear equations

$$\begin{aligned} \varepsilon'_{r,0}(E_0) &= a'_0 + a' E_0 \quad , \\ \varepsilon''_{r,0}(E_0) &= a''_0 + a'' E_0 \quad , \\ \Delta\varepsilon'_r(E_0) &= b'_0 + b' E_0 \quad . \end{aligned} \tag{11}$$

To specify the coefficients in Eq. (11), we insert Eq. (11) into Eq. (4), which yields

$$\begin{aligned} \varepsilon'_r(E_0, f) &= [a'_0 + a' E_0] + [b'_0 + b' E_0] \ln\left(\frac{1\,\text{Hz}}{2\pi f}\right) \quad , \\ \varepsilon''_r(E_0, f) &= [a''_0 + a'' E_0] \quad . \end{aligned} \tag{12}$$

Comparing the real part $\varepsilon'_r(E_0, f)$ of Eq. (12) with Eqs. (5) and (6), gives rise to the identifications $a'_0 \equiv \varepsilon'_{r,\text{in},0}$, $b'_0 \equiv \Delta\varepsilon'_{r,\text{in}}$, $a' \equiv \alpha'_0$ and $b' \equiv \Delta\alpha'$. It should be noted, that similar identifications were previously demonstrated to be valid for a PZT-based ferroelectric ceramic [19]. However, the imaginary part of the material response was not considered in Ref. 19. Here, com-

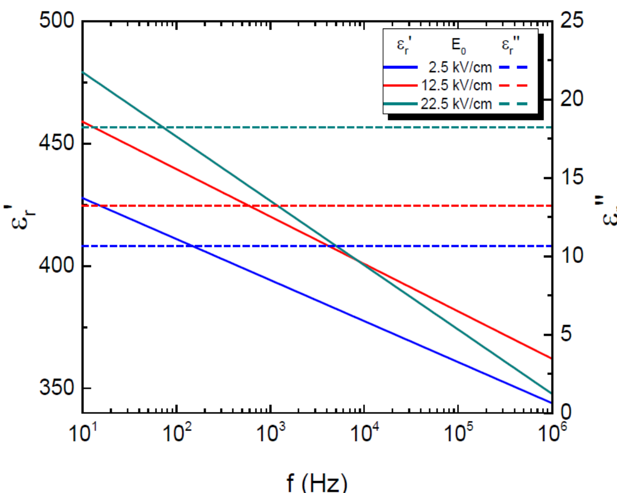

FIG. 4. Complex relative permittivity $\varepsilon_r(f)$ of the BCZT film for a selection of three different excitation field amplitudes E_0.

parison of the frequency-independent imaginary part in Eq. (12), with the imaginary part of the Rayleigh law Eq. (1) yields the additional identifications $a''_0 \equiv \varepsilon''_{r,\text{in}}$ and $a'' \equiv \alpha''$.

Altogether, the field dependence of the dispersion parameters Eq. (11) can then be written in the following form

$$\begin{aligned}\varepsilon'_{r,0}(E_0) &= \varepsilon'_{r,\text{in},0} + \alpha'_0 E_0 \quad , \\ \varepsilon''_{r,0}(E_0) &= \varepsilon''_{r,\text{in}} + \alpha'' E_0 \quad , \\ \Delta\varepsilon'_r(E_0) &= \Delta\varepsilon'_{r,\text{in}} + \Delta\alpha' E_0 \quad , \end{aligned} \tag{13}$$

where the coefficient $\Delta\varepsilon'_{r,\text{in}}$ is the zero-field contribution to the logarithmic dispersion strength and the field-

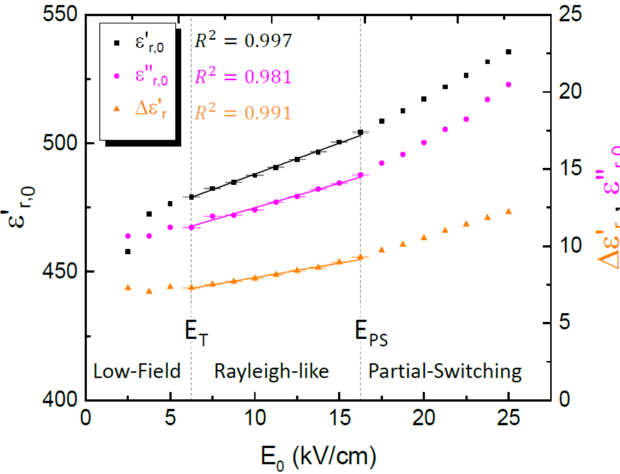

FIG. 5. Field dependence of the dispersion parameters $\varepsilon'_{r,0}(E_0)$, $\varepsilon''_{r,0}(E_0)$ and $\Delta\varepsilon'_r(E_0)$ of the BCZT film. The solid lines are linear fits in the region between the two vertical dashed lines, which mark the threshold field E_T and the partial switching field E_PS.

dependent contribution is given by $\Delta\alpha' E_0$.

Subsequently, linear fits according to Eq. (13) were carried out in the range $6.25\,\text{kV/cm} \leq E_0 \leq 16.25\,\text{kV/cm}$ as indicated by the vertical dashed lines in Fig. 5. The starting point for the linear fits at $E_0 = 6.25\,\text{kV/cm} \equiv E_\text{T}$ was determined by the criterion that all subsequent data points are required to have a higher value compared to their left neighbor. The endpoint for the linear fits was then chosen by the longest fitting range for which every linear fit has a correlation factor $R^2 \geq 0.980$, which is fulfilled for $E_0 = 16.25\,\text{kV/cm} \equiv E_\text{PS}$. At higher fields, all three curves in Fig. 5, show an upward curvature which we attribute to the partial switching of domains [18]. For the linear fits, the estimated standard errors from the previous equivalent-circuit fitting procedure were taken into account, which is also indicated by the error bars within the fitting range [c.f. Fig. 5]. The results of the fits according to Eq. (13) are summarized in Table II.

From the extracted fit parameters, the functional form of the frequency-dependent reversible and irreversible Rayleigh parameter of the BCZT thin film can be immediately obtained according to Eq. (5) and the results are depicted in Fig. 6. Here, the vertical dotted line at $f_\text{R} \sim 1$ kHz indicates the Rayleigh frequency for the BCZT thin film, which we calculated according to Eq. (7). As discussed in Sec. II, f_R is part of the Rayleigh-like frequency range, where the center of mass of the domain walls can move irreversibly via hopping between potential minima corresponding to the stochastic regime.

The dashed line at $f_0 \sim 63$ kHz marks the region where the irreversible Rayleigh parameter α' is zero and changes sign to negative values. This might indicate a transition from the stochastic regime to a pinned regime, in which the center of mass motion of the domain walls cannot follow the fast driving field, and thus the domain walls are captured in a potential valley. [11]. Similar experimental indications for the freezing of the irreversible center of mass motion of the domain walls at higher frequencies were reported previously [22].

By inserting the functional form of the field dependent frequency dispersion parameters [c.f. Fig. 5 and Table II] into Eq. (4), we finally obtain the functional form of the field and frequency dependent dielectric response in the epitaxial BCZT thin film, which is given by

$$\begin{aligned}\varepsilon'_r(E_0,f) &= \varepsilon'_{r,\text{in},0} + \alpha'_0 E_0 + [\Delta\varepsilon'_{r,\text{in}} + \Delta\alpha' E_0]\ln\left(\frac{1\,\text{Hz}}{2\pi f}\right) \\ \varepsilon''_r(E_0,f) &= \varepsilon''_{r,\text{in}} + \alpha'' E_0. \end{aligned} \tag{14}$$

Note that $\varepsilon''_{r,\text{in}}$ in Eq. (14) is not zero, which could be an indication for an internal bias or stress field [8].

The coupling between field dependence and frequency dispersion in the BCZT thin film arises explicitly in Eq. (14) as the product of E_0 and the f-dependent term. Thus, this gives rise to the identifiation of the coefficient $\Delta\alpha'$ as the coupling strength beetween dielectric nonlinearity and frequency dispersion, which is defined as the change of logarithmic frequency dispersion strength with field amplitude - or equivalent - as the change of

TABLE II. Extracted parameters from the linear fits according to Eq. (13). The estimated uncertainties from previous fitting steps were taken into account.

$\varepsilon'_{r,\mathrm{in},0}$	α'_0 (cm/kV)	$\varepsilon''_{r,\mathrm{in}}$	α'' (cm/kV)	$\Delta\varepsilon'_{r,\mathrm{in}}$	$\Delta\alpha'$ (cm/kV)
463.9 ± 0.1	2.41 ± 0.01	9.31 ± 0.02	0.318 ± 0.002	6.09 ± 0.03	0.187 ± 0.003

the irreversible Rayleigh parameter with the logarithm of frequency, i.e.

$$\Delta\alpha' \equiv \frac{\partial \alpha'(f)}{\partial \ln\left(\frac{1\,\mathrm{Hz}}{2\pi f}\right)} \equiv \frac{\partial \Delta\varepsilon'_r(E_0)}{\partial E_0} \quad , \tag{15}$$

which has a value of 0.187 cm/kV in the epitaxial BCZT thin film. In fact, the negative values of the irreversible Rayleigh parameter are a direct consequence of the coupling between frequency dispersion and dielectric nonlinearity in the BCZT thin film.

Altogether, our analysis yields the schematic diagram depicted in Fig. 7 for the different domain wall motion regimes in the epitaxial BCZT thin film. Note, that the diagram constructed in Fig. 7 is not a generic diagram for any epitaxial BCZT film. In fact, it is a schematic diagram of different domain-wall motion regimes, which can now be identified within the framework of the extended Rayleigh analysis.

At low field amplitudes $0 < E_0 < E_\mathrm{T}$, the center of mass of the domain walls cannot overcome the potential well Eq. (3) of the random energy landscape, however, domain wall segments can jump between metastable states with close energies, which corresponds to the non-coupled pinning regime. This observation has similarities to what has been found theoretically for disordered ferromagnets [31]. By increasing the field amplitude above the threshold field E_T, the center of mass of the domain walls can additionally jump between different potential minima, resulting in a coexistence of irreversible center of mass motion and relaxational motion of internal modes in the stochastic regime. Note that this coexistence is not simply additive, due to the coupling of dielectric nonlinearity and frequency dispersion. As a consequence of coupling, the irreversible Rayleigh parameter becomes zero at $f_0 \sim 63$ kHz and changes to negative values in the pinned coupling regime. Note that in this coupled-pinning regime, domain wall segments can still jump between metastable states, which is indicated by the logarithmic frequency dispersion observed in this regime. The domain wall dynamics in the coupled-pinning regime is not fully understood and remains as a task of a unified theory of dielectric nonlinearity and frequency dispersion, which is not yet available.

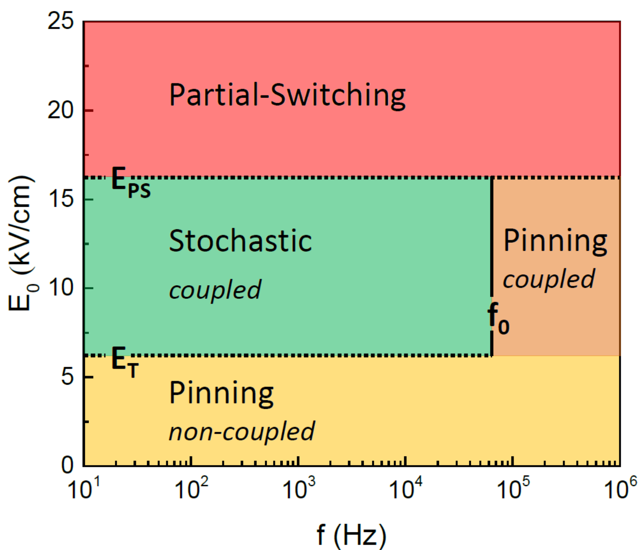

FIG. 7. Schematic diagram of the different domain wall motion regimes of the epitaxial BCZT thin film. The threshold field $E_\mathrm{T} = 6.25\,\mathrm{kV/cm}$ and the partial switching field $E_\mathrm{PS} = 16.25\,\mathrm{kV/cm}$ are obtained from the field dependence of the dispersion parameters [c. f. Fig. 5] and $f_0 \sim 63$ kHz is determined from the frequency dispersion of the irreversible Rayleigh parameter [c. f. Fig. 6].

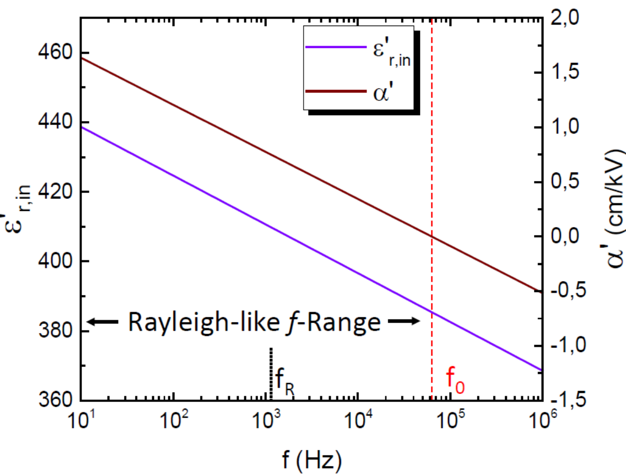

FIG. 6. Logarithmic frequency dispersion of reversible $\varepsilon'_{r,\mathrm{in}}(f)$ and irreversible $\alpha'(f)$ Rayleigh parameters of the BCZT film. The vertical dotted line at ~ 1 kHz marks the Rayleigh frequency f_R. The irreversible Rayleigh parameter changes to negative values at $f_0 \sim 63$ kHz, which is indicated by the vertical dashed line.

V. CONCLUSION

In conclusion, this work demonstrates several key aspects. We introduce the domain wall pinning element Z_{DW} based on the theory of interface pining in random systems, which includes the characteristic logarithmic frequency dispersion due to domain wall pinning in a random energy landscape and hence models the impedance response of a ferroelectric below the coercive field. Since domain wall pinning occurs solely in the ferroelectric and not in the electrodes and interfaces, the impedance response of electrodes and interfaces do not exhibit the characteristic logarithmic frequency dispersion and hence can be discriminated by their different frequency dispersion from the domain wall pinning element which models the ferroelectric. Thus, different contributions to the measured overall impedance response are deconvoluted by equivalent-circuit fitting with the domain wall pinning element. Moreover, we demonstrate the practical application of this new element to extract the field- and frequency-dependent dielectric response in an epitaxial lead-free ferroelectric BCZT thin film embedded in a capacitor stack and we reveal its superiority over the conventional approach. In addition, we perform an extended Rayleigh analysis which results in the quantification of the coupling strength and the explicit functional form $\varepsilon_r(E_0, f)$ of the coupled dielectric response in the BCZT film. Finally, we present a schematic diagram of the different domain wall motion regimes in the BCZT film and discuss the corresponding domain wall dynamics.

The present work is intended to serve as a guideline for future work on ferroelectric materials, which includes to reveal the effect of temperature and phase transitions [32], external bias fields [4], dopants [21], ion-bombardement [33, 34] and substrate clamping [22] on domain wall dynamics and related material properties. This may provide new insights into nonlinear contributions to the dielectric- and piezoelectric responses, which is also of practical importance for many microelectromechanical systems (MEMS) and may help to develop a unified theory of frequency dispersion and dielectric nonlinearity in ferroelectrics.

ACKNOWLEDGEMENTS

We gratefully acknowledge fruitful discussions with C. Warres (NMI), C. Hofer and J. C. Meyer and technical support by M. Turad and R. Löffler (LISA$^+$). This work was partially funded by the Bundesministerium für Bildung und Forschung (BMBF) under Grant No. 13GW0123E and partly funded by the Europäische Fonds für regionale Entwicklung (EFRE) under Grant No. 712303.

APPENDIX A: CONVENTIONAL APPROACH

For the conventional approach, the measured complex impedance $Z = Z' - iZ''$ of the capacitor stacks is converted into complex permittivity data of the capacitor stacks using the formalism described in Ref. 23, resulting in

$$\varepsilon'_{r,\mathrm{stack}}(f) = \frac{-Z''}{2\pi f \varepsilon_0 (Z'^2 + Z''^2)} \frac{d}{A} \quad ,$$
$$\varepsilon''_{r,\mathrm{stack}}(f) = \frac{Z'}{2\pi f \varepsilon_0 (Z'^2 + Z''^2)} \frac{d}{A} \quad . \tag{16}$$

The resulting $\varepsilon_{r,\mathrm{stack}}(f)$ plots are shown in Figure 8 for a selection of three different E_0. For comparison, also the extracted complex permittivity $\varepsilon_r(f)$ of the BCZT layer from the equivalent-circuit fits [c.f. Fig. 4 and Eq. (4)] is depicted. The capacitor stack exhibits a Debye-like dielectric relaxation at high frequencies ($\sim 10^5$ Hz), due to to resistive losses in the electrodes [9]. Moreover, the dielectric spectrum of the epitaxial thin film capacitor indicates an additional Debye-like relaxation process at lower frequencies (~ 100 Hz). We attribute this second relaxation process to an extrinsic electrode/film interface effect, which was previously reported to occur in other ferroelectric thin films grown on Nb:STO substrates [13]. This is also consistent with the theoretical discussion of the potential well Eq. (3) within a random energy landscape, which leads to a distribution of relaxation times in the BCZT layer and hence the BCZT layer is not expected to exhibit a Debye-like dielectric relaxation which corresponds to a single relaxation time and hence one dominant relaxation frequency f_r. The relaxation frequency can be calculated from the obtained interface fit parameters R_1 and C_1 according to the relation

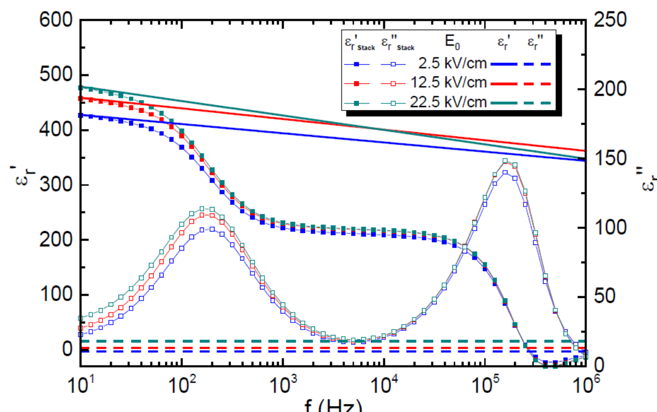

FIG. 8. Measured permittivities $\varepsilon'_{r,\mathrm{stack}}(f)$ (full symbols) and $\varepsilon''_{r,\mathrm{stack}}(f)$ (open symbols) of the BCZT capacitor stack for a selection of different excitation field amplitudes E_0. For clarity, the symbols are connected by thin lines which do not represent fits to the data. For comparison, the extracted permittivities of the BCZT layer from the equivalent-circuit fits [c.f. Fig. 4 and Eq. (4)] are also shown (solid and dashed thick lines).

$f_{\mathrm{r}} = 1/2\pi R_1 C_1$. The calculated relaxation frequencies are in agreement with the peaks in the imaginary part of permittvity of the capacitor stack [c.f. 8] at frequencies ($\sim 100\,\mathrm{Hz}$), which indicates the correct deconvolution of film and interface contributions by our equivalent-circuit fits. Moreover, for BCZT thin films grown on platinized Si substrates, the second Debye-like dielectric relaxation was absent [35]. Furthermore, we note that the slightly negative values of $\varepsilon'_{r,\mathrm{stack}}(f)$ at frequencies around 1 MHz are due to the inductance of the cables used [29].

It is clear, that the extraction of frequency dispersion of permittivity from [c.f. Eq. (16) and symbols in Fig. 8] does not reflect the true dielectric dispersion of the BCZT thin film, since there is no deconvolution of electronically distinct components forming the capacitor heterostructure. The same is true for the extraction of Rayleigh parameters, which has been recently demonstrated [8].

APPENDIX B: VALIDATION OF IMPEDANCE SPECTRA

Impedance spectra might be afflicted with artifacts. To rule out artifacts introduced by experimental set-up conditions in the measured impedance spectra, we use the two-pole Hilbert transform (Z-HIT) described in Ref. 36. This approach is beneficial compared to methods based on Kramers-Kronig (KK) relations [37, 38], since the KK relations are strictly defined within the frequency range between zero and infinity and hence, the extrapolation of the measured impedance data is a unavoidable task which may lead to erroneous results [36]. The Z-HIT avoids the necessity of an extrapolation of the frequency range and allows one to reconstruct the modulus of the impedance $|Z|$ vs f from the measured values of the less artifact-prone [8, 36] phase angle. The results of the Z-HIT for three different excitation field amplitudes E_0 are depicted in Fig. 9. In all cases, the reconstructed curves match fairly well with the measured data, which indicates that the measured impedance spectra are not afflicted with artifacts and the investigated system is stable, causal, (sufficiently) linear [8] and exhibits finite values over the entire frequency range.

APPENDIX C: LOGARITHMIC BODE PLOT

To further check the overall quality of the equivalent-circuit fits, the impedance modulus $|Z|$ and the phase angle are depicted in the logarithmic Bode plot in Fig. 10. In all cases, the fits are in good agreement with the measured data which indicates the validity of the equivalent-circuit model [c.f. Fig. 3(b)].

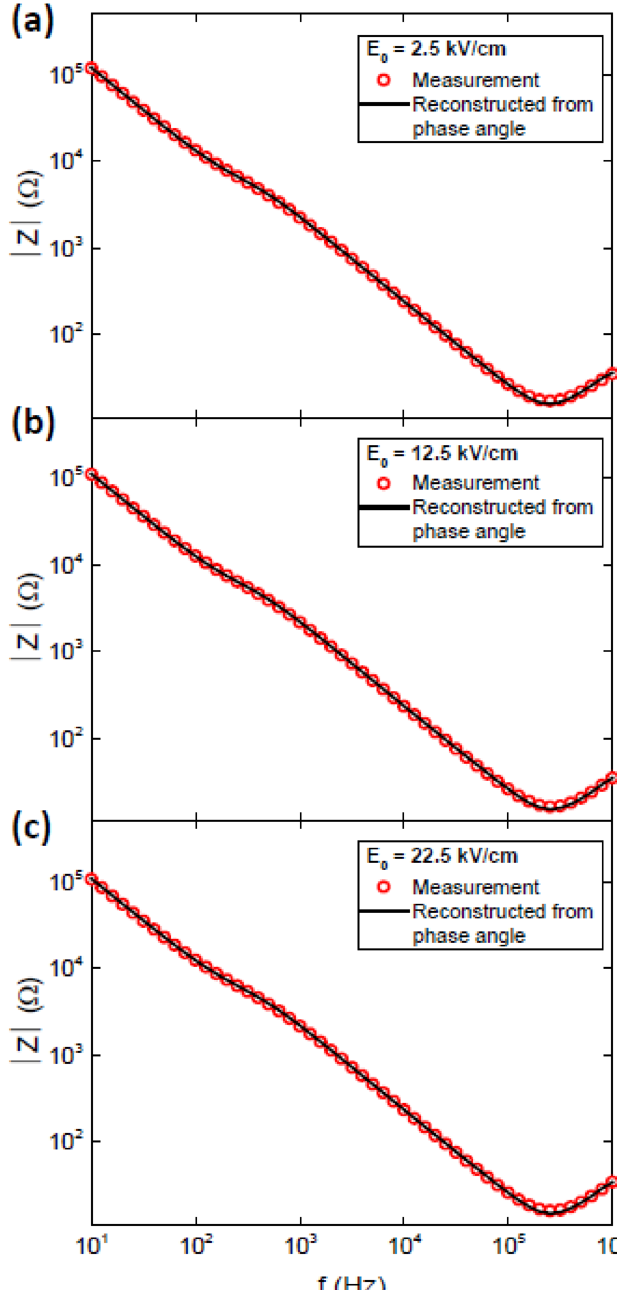

FIG. 9. Comparison of measured (symbols) and Z-HIT-reconstructed (black solid lines) impedance modulus $|Z|$ of the BCZT capacitor stack vs frequency f for (a) $E_0 = 2.5$ kV/cm, (b) $E_0 = 12.5$ kV/cm and (c) $E_0 = 22.5$ kV/cm.

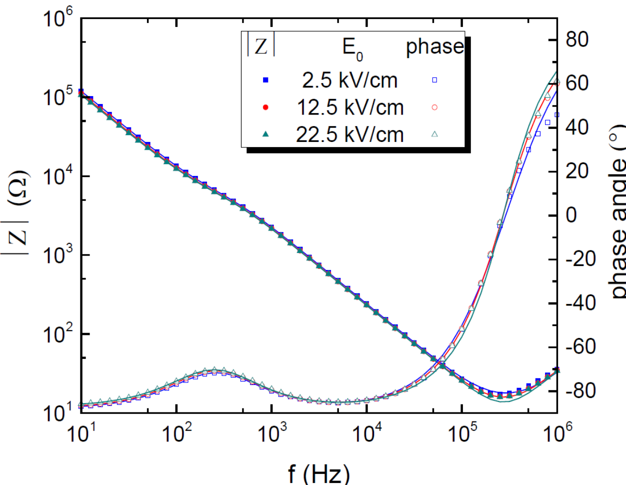

FIG. 10. Logarithmic Bode plot of impedance modulus $|Z|$ and phase angle obtained by impedance spectroscopy (symbols) and the corresponding equivalent-circuit fits (solid lines) for a selection of different E_0 on the epitaxial BCZT thin-film capacitor stack.

[1] D. Damjanovic, “Ferroelectric, dielectric and piezoelectric properties of ferroelectric thin films and ceramics,” Rep. Progr. Phys. **61**, 1267 (1998).

[2] D. Damjanovic, S. S. N. Bharadwaja, and N. Setter, “Toward a unified description of nonlinearity and frequency dispersion of piezoelectric and dielectric responses in Pb(Zr,Ti)O_3,” Mat. Science and Eng. B **120**, 170 (2005).

[3] N. Bassiri-Gharb and S. Trolier-McKinstry, “Dielectric nonlinearity of Pb($Yb_{1/2}Nb_{1/2}O_3$–$PbTiO_3$ thin films with (100) and (111) crystallographic orientation,” J. Appl. Phys. **97**, 064106 (2005).

[4] N. Bassiri-Gharb, I. Fujii, E. Hong, S. Trolier-McKinstry, D. V. Taylor, and D. Damjanovic, “Domain wall contributions to the properties of piezoelectric thin films,” J. Electroceram. **19**, 49 (2007).

[5] S. Trolier-McKinstry and P. Muralt, “Thin film piezoelectrics for MEMS,” J. Electroceram. **12**, 7 (2004).

[6] Y. Saito, H. Takao, T. Tani, T. Nonoyama, K. Takatori, T. Homma, T. Nagaya, and M. Nakamura, “Lead-free piezoceramics,” Nature **432**, 84 (2004).

[7] W. Liu and X. Ren, “Large piezoelectric effect in Pb-free ceramics,” Phys. Rev. Lett. **103**, 257602 (2009).

[8] T. Schenk, M. Hoffmann, M. Pesic, M. H. Park, C. Richter, U. Schroeder, and T. Mikolajick, “Physical approach to ferroelectric impedance spectroscopy: The Rayleigh element,” Phys. Rev. Appl. **10**, 064004 (2018).

[9] M. Tyunina, “Size effects and dielectric behaviour in ferroelectric heterostructures,” J. Phys.: Condens. Matter **18**, 5725 (2006).

[10] T. Nattermann, Y. Shapir, and I. Vilfan, “Interface pinning and dynamics in random systems,” Phys. Rev. B. **42**, 8577 (1990).

[11] A. A. Fedorenko, V. Mueller, and S. Stepanow, “Dielectric response due to stochastic motion of pinned domain walls,” Phys. Rev. B **70**, 224104 (2004).

[12] R. Schmidt, W. Eerenstein, T. Winiecki, F. D. Morrison, and P. A. Midgley, “Impedance spectroscopy of epitaxial multiferroic thin films,” Phys. Rev. B **75**, 245111 (2007).

[13] R. Schmidt, J. Ventura, E. Langenberg, N. M. Nemes, C. Munuera, M. Varela, M. Garcia-Hernandez, C. Leon, and J. Santamaria, “Magnetoimpedance spectroscopy of epitaxial multiferroic thin films,” Phys. Rev. B **86**, 035113 (2012).

[14] H. Kronmüller, “Statistical theory of Rayleigh's law,” Z. Angew. Phys. **30**, 1 (1970).

[15] O. Boser, “Statistical theory of hysteresis in ferroelectric materials,” J. Appl. Phys. **62**, 1344 (1987).

[16] D. Damjanovic, “Stress and frequency dependence of the direct piezoelectric effect in ferroelectric ceramics,” J. Appl. Phys. **82**, 1788 (1997).

[17] D. V. Taylor and D. Damjanovic, “Evidence of domain wall contribution to the dielectric permittivity in PZT thin films at sub-switching fields,” J. Appl. Phys. **82**, 4 (1997).

[18] D. A. Hall, “Rayleigh behaviour and the threshold field in ferroelectric ceramics,” Ferroelectrics **223**, 319 (1999).

[19] D. Damjanovic, “Logarithmic frequency dependence of the piezoelectric effect due to pinning of ferroelectric-ferroelastic domain walls,” Phys. Rev. B **55**, R649 (1997).

[20] V. Mueller, H. Beige, and H. P. Abicht, “Non-debye dielectric dispersion of barium titanate stannate in the relaxor and diffuse phase-transition state,” Appl. Phys. Lett. **84**, 1341 (2004).

[21] L. Yang, H. Fang, L. Zheng, J. Du, L. Wang, X. Lu, W. Lü, R. Zhang, and W. Cao, “Evaluation of reversible and irreversible domain wall motion in relaxor ferroelectrics: Influence of acceptor ions,” Appl. Phys. Lett. **114**, 232901 (2019).

[22] F. Griggio, S. Jesse, A. Kumar, O. Ovchinnikov, T. N. Jackson, D. Damjanovic, S. V. Kalinin, and S. Trolier-McKinstry, “Substrate clamping effects on irreversible domain wall dynamics in lead zirconate titanate thin films,” Phys. Rev. Lett. **108**, 157604 (2012).

[23] R. Gerhardt, “Impedance and dielectric spectroscopy revisited: Distinguishing localized relaxation from long-range conductivity,” J. Phys. Chem. Solids **55**, 1491 (1994).

[24] D. S. Keeble, F. Benabdallah, P. A. Thomas, M. Maglione, and J. Kreisel, “Revised structural phase diagram of ($Ba_{0.7}Ca_{0.3}TiO_3$)–($BaZr_{0.2}Ti_{0.8}O_3$),” Appl. Phys. Lett. **102**, 092903 (2013).

[25] N. D. Scarisoreanu, F. Craciun, A. Moldovan, V. Ion, R. Birjega, C. Ghica, R. F. Negrea, and M. Dinescu, “High permittivity (1-x)Ba($Zr_{0.2}Ti_{0.8}$)O_3–x($Ba_{0.7}Ca_{0.3}$)TiO_3 (x=0.45) epitaxial thin films with nanoscale phase fluctuations,” ACS Appl. Mater. Interfaces **7**, 23984 (2015).

[26] Q. Lin, D. Wang, and S. Li, “Strong effect of oxygen partial pressure on electrical properties of 0.5Ba($Zr_{0.2}Ti_{0.8}$)O_3–0.5($Ba_{0.7}Ca_{0.3}$)TiO_3 thin films,” J. Am. Ceram. Soc. **98**, 2094 (2015).

[27] D. Su, Q. Meng, C. A. F. Vaz, M.-G. Han, Y. Segal, F. J. Walker, M. Sawicki, C. Broadbridge, and C. H. Ahn, “Origin of 90° domain wall pinning in Pb($Zr_{0.2}Ti_{0.8}$)O_3 heteroepitaxial thin films,” Appl. Phys. Lett. **99**, 102902 (2011).

[28] A Wolfram Mathematica script to fit impedance data with an equivalent-circuit model containing the domain wall pinning element can be made available to interested readers upon reasonable request addressed to the corresponding author.

[29] J. R. Macdonald and E. Barsoukov, *Impedance Spectroscopy*, 3rd ed. (Wiley, New York, 2018).

[30] P. G. Hoel, *Introduction to Mathematical Statistics*, 3rd ed. (Wiley, New York, 1962).

[31] T. Nattermann, V. Pokrovsky, and V. M. Vinokur, “Hysteretic dynamics of domain walls at finite temperatures,” Phys. Rev. Lett. **87**, 197005 (2001).

[32] A. Piorra, V. Hrkac, N. Wolff, C. Zamponi, V. Duppel, J. Hadermann, L. Kienle, and E. Quandt, “($Ba_{0.85}Ca_{0.15}$)($Ti_{0.9}Zr_{0.1}O_3$) thin films prepared by PLD: Relaxor properties and complex microstrucure,” J. Appl. Phys. **125**, 244103 (2019).

[33] S. Saremi, R. Xu, F. I. Allen, J. Maher, J. C. Agar, R. Gao, P. Hosemann, and L. W. Martin, “Local control of defects and switching properties in ferroelectric thin films,” Phys. Rev. Materials **2**, 084414 (2018).

[34] S. Saremi, J. Kim, A. Ghosh, D. Meyers, and L. W. Martin, “Defect-induced (dis)order in relaxor ferroelectric thin films,” Phys. Rev. Lett. **123**, 207602 (2019).

[35] M. Becker, C. J. Burkhardt, B. Schröppel, R. Kleiner, and D. Koelle, "Rayleigh analysis and dielectric dispersion in polycrystalline $0.5(Ba_{0.7}Ca_{0.3})TiO_3$–$0.5Ba(Zr_{0.2}Ti_{0.8})O_3$ ferroelectric thin films by domain-wall pinning element modeling," J. Appl. Phys. **128**, 154103 (2020).

[36] C. A. Schiller, F. Richter, E. Gülzow, and N. Wagner, "Validation and evaluation of electrochemical impedance spectra of systems with states that change with time," Phys. Chem. Chem. Phys. **3**, 374 (2001).

[37] M. Urquidi-Macdonald, S. Real, and D. D. Macdonald, "Applications of Kramers-Kronig transforms in the analysis of electrochemical impedance data – III. Stability and linearity," Electrochim. Acta **35**, 1559 (1990).

[38] P. Agarwal, M. E. Orazem, and L. H. Garcia-Rubio, "Application of measurement models to impedance spectroscopy III. Evaluation of consistency with the Kramers-Kronig relations," J. Electrochem. Soc. **142**, 1885 (1995).

Publication II

Reproduced from M. Becker *et al.*, J. Appl. Phys. **128**, 154103 (2020), with the permission of AIP Publishing.

Journal of Applied Physics

Rayleigh analysis and dielectric dispersion in polycrystalline $0.5(Ba_{0.7}Ca_{0.3})TiO_3$–$0.5Ba(Zr_{0.2}Ti_{0.8})O_3$ ferroelectric thin films by domain-wall pinning element modeling

Cite as: J. Appl. Phys. **128**, 154103 (2020); https://doi.org/10.1063/5.0025109
Submitted: 13 August 2020 . Accepted: 09 October 2020 . Published Online: 21 October 2020

M. Becker, C. J. Burkhardt, B. Schröppel, R. Kleiner, and D. Koelle

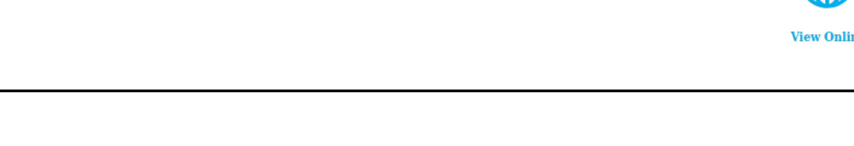

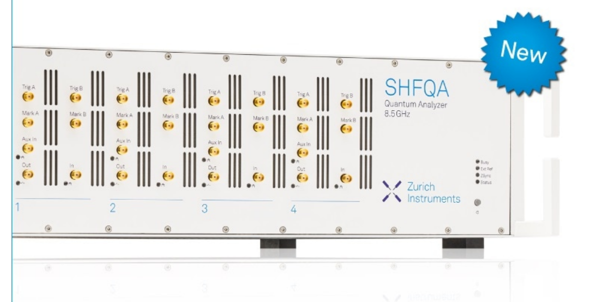

Your Qubits. Measured.
Meet the next generation of quantum analyzers
- Readout for up to 64 qubits
- Operation at up to 8.5 GHz, mixer-calibration-free
- Signal optimization with minimal latency

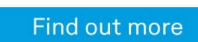

© 2020 Author(s).

Journal of Applied Physics | ARTICLE | scitation.org/journal/jap

Rayleigh analysis and dielectric dispersion in polycrystalline $0.5(Ba_{0.7}Ca_{0.3})TiO_3–0.5Ba(Zr_{0.2}Ti_{0.8})O_3$ ferroelectric thin films by domain-wall pinning element modeling

Cite as: J. Appl. Phys. **128**, 154103 (2020); doi: 10.1063/5.0025109
Submitted: 13 August 2020 · Accepted: 9 October 2020 ·
Published Online: 21 October 2020

View Online
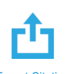
Export Citation

CrossMark

M. Becker,[1,2,a)] C. J. Burkhardt,[1] B. Schröppel,[1] R. Kleiner,[2] and D. Koelle[2]

AFFILIATIONS

[1] NMI Natural and Medical Sciences Institute at the University of Tübingen, Markwiesenstr. 55, 72770 Reutlingen, Germany
[2] Physikalisches Institut, Center for Quantum Science (CQ), and LISA+, University of Tübingen, Auf der Morgenstelle 14, 72076 Tübingen, Germany

[a)] **Author to whom correspondence should be addressed:** maximilian.becker@nmi.de

ABSTRACT

We use impedance spectroscopy to investigate the dielectric response in polycrystalline, lead-free $0.5(Ba_{0.7}Ca_{0.3})TiO_3–0.5Ba(Zr_{0.2}Ti_{0.8})O_3$ (BCZT) ferroelectric thin films as a function of amplitude E_0 and frequency f of an applied ac electric field. Impedance spectra from $f = 10$ Hz to 1 MHz were collected at different E_0 on polycrystalline BCZT capacitor stacks, grown by pulsed laser deposition on platinized Si substrates and covered with Au electrodes. Deconvolution of the spectra is achieved by fitting the measured impedance to the impedance of an equivalent-circuit model of the capacitor stacks, including a recently proposed domain-wall pinning element Z_{DW}. From an extended data analysis, we quantify the coupling strength between dielectric nonlinearity and frequency dispersion in the BCZT thin films, and we obtain a schematic diagram of the different domain-wall-motion regimes. Our results indicate that the presence of grain boundaries in BCZT reduces the coupling strength and suppresses the motion of internal domain-wall segments and also the irreversible center-of-mass motion of the domain walls.

Published under license by AIP Publishing. https://doi.org/10.1063/5.0025109

I. INTRODUCTION

Nanogenerators, piezoelectric biosensors, and other microelectromechanical systems (MEMS) are often based on ferroelectric thin films, which offer a number of advantages in MEMS devices.[1–6] Among them are the large piezoelectric coefficients available in ferroelectric films, which enable low-voltage operation of actuators and fabrication of high-sensitivity sensors. However, the piezoelectric coefficients are not the only relevant material parameters for MEMS applications of ferroelectric thin films. Similarly, their dielectric response is an important material property, and the real and imaginary parts of complex relative permittivity $\varepsilon_r = \varepsilon_r' - i\varepsilon_r''$ are included in various existing figures of merit (FOMs) for piezoelectric MEMS, which act as a benchmark for device performance. For example, the corresponding FOM for thin-film energy harvesting devices contains ε_r' and is given by[1,6]

$$\mathrm{FOM}_{\mathrm{EH}} = \frac{e_{31,f}^2}{\varepsilon_0 \varepsilon_r'}, \tag{1}$$

where $e_{31,f}$ denotes the effective transversal piezoelectric coefficient and ε_0 the vacuum permittivity. Moreover, the FOM for the intrinsic signal-to-noise ratio of piezoelectric sensors,

$$\mathrm{FOM}_{\mathrm{SNR}} = \frac{e_{31,f}}{\sqrt{\varepsilon_0 \varepsilon_r''}}, \tag{2}$$

includes the imaginary part ε_r'' of the complex relative permittivity.[1] Thus, the knowledge of the dielectric response $\varepsilon_r(E_0, f)$ to an applied ac electric field—with frequency f and amplitude

Published under license by AIP Publishing.

E_0—of ferroelectric thin films is crucial for device modeling and FOM enhancements. This is especially true for lead-free $BaTiO_3$-based ferroelectrics, which are promising alternative materials to replace $PbZr_xTi_{1-x}O_3$ (PZT) in MEMS devices; however, their FOMs for various MEMS applications are still worse than the corresponding FOMs for PZT thin films.[7]

In general, comprehensive and reliable measurements of the dielectric response in heterostructures containing ferroelectric thin films are challenging since electrodes and film–electrode interfaces can mask the dielectric response of the ferroelectric layer.[8–10] Very recently, a solution to this problem—based on an equivalent-circuit element Z_{DW}, which models the impedance of a ferroelectric due to domain-wall pinning—was proposed,[11] which allows one to extract $\varepsilon_r(E_0, f)$ from impedance spectroscopy measurements. Additionally, this approach enables one to evaluate the coupling strength between dielectric nonlinearity and frequency dispersion and to identify different domain-wall-motion regimes. The method was successfully applied to epitaxial lead-free $0.5(Ba_{0.7}Ca_{0.3})TiO_3$–$0.5Ba(Zr_{0.2}Ti_{0.8})O_3$ (BCZT) thin films deposited on (100)-oriented single crystalline Nb-doped $SrTiO_3$ substrates.[11]

However, in MEMS technology, many of the utilized ferroelectrics are polycrystalline thin films deposited on platinized Si wafers. Here, we report on the application of the novel domain-wall pinning element Z_{DW} to analyze the dielectric response $\varepsilon_r(E_0, f)$ in polycrystalline BCZT thin films deposited on platinized Si substrates.

II. EXPERIMENTAL

A ceramic BCZT target was used to grow 200-nm-thick polycrystalline films on (111)-textured $Pt/Ti/SiO_2/Si$ substrates by pulsed laser deposition. We used a 248 nm KrF excimer laser with an energy of 110 mJ and a repetition rate of 5 Hz. During deposition at an oxygen partial pressure $p_{O_2} = 0.1$ mbar, the temperature was fixed at 650 °C. After deposition, the films were heated to 680 °C in $p_{O_2} = 5$ mbar and kept there for 45 min before cooling down to room temperature with a rate of 10 K/min.

The microstructure of the BCZT films was investigated by x-ray diffraction (XRD) to obtain the crystallographic orientation and to check for possible secondary phases. One sample was further analyzed by scanning transmission electron microscopy (STEM) to investigate the grain morphology and to determine the film thickness.

For electrical measurements, 3 -mm-diameter disk-shaped Au electrodes, around 100-nm-thick, were deposited on top of the BCZT films by electron beam evaporation through a shadow mask. Impedance spectra from 10 Hz to 1 MHz were collected at different excitation-field amplitudes E_0 using a Solartron 1260 impedance analyzer together with a probe station. For each measurement, E_0 was successively increased from 5 to 90 kV/cm (applied root mean square voltage $V_{RMS} = 0.1$–1.8 V) with a step-size of 5 kV/cm.

III. RESULTS AND DISCUSSION

In this section, we present XRD data and results from electrical measurements from one representative polycrystalline BCZT device. The STEM results were obtained from a different

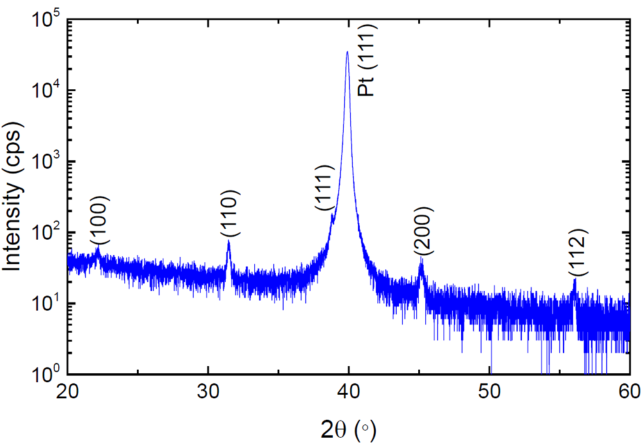

FIG. 1. XRD θ–2θ scan of BCZT thin film deposited on a (111)-textured $Pt/Ti/SiO_2/Si$ substrate.

polycrystalline BCZT device, which was fabricated with the same process parameters (see Sec. II).

Figure 1 shows the XRD θ–2θ diffraction pattern for a BCZT thin film deposited on a (111)-textured $Pt/Ti/SiO_2/Si$ substrate. No traces of secondary phases are observable. The structural phase diagram of BCZT shows four possible crystallographic phases, i.e., cubic, tetragonal, orthorhombic, and rhombohedral.[12] Due to the small variations in the lattice parameters of the possible phases, a rigorous specification of the crystallographic phase of the films is not accessible from the XRD data. Thus, we denote the film structure as pseudo-cubic, which represents the four possible phases. For simplicity, we use cubic metrics for the Miller indices. The film grown on a (111)-textured $Pt/Ti/SiO_2/Si$ substrate is polycrystalline with mixed orientation of the grains, which is similar to earlier results on BCZT thin films,[13] though the (111)-BCZT peak is less pronounced in our film.

From the cross-sectional STEM image depicted in Fig. 2, the morphology of the BCZT grains can be investigated. We observe columnar growth of the grains, which extends throughout the whole film thickness; i.e., there are no grain boundaries connected in series. Moreover, the BCZT film thickness is confirmed to be around 200 nm.

The collected impedance spectroscopy data on the polycrystalline BCZT capacitor stack (for three different E_0) are shown in Fig. 3(a). A validation procedure to rule out artifacts in the measured impedance spectra is given in Appendix A. The equivalent circuit depicted in Fig. 3(b) was used to fit the collected impedance spectra. Here, the series resistance R_0 corresponds to the resistance of the cables, measurement probes, and electrodes, and the R_1C_1 element represents the electrode–BCZT interfaces. The element L_0 models the inductance of the cables used.[14] The resistance R_2 and the domain-wall pinning element Z_{DW} model the ferroelectric film inside the capacitor stack. Note that the grains of the BCZT layer extend throughout the whole film thickness; i.e., there are no grain boundaries and grains connected in series [cf. Fig. 2], and hence,

Published under license by AIP Publishing.

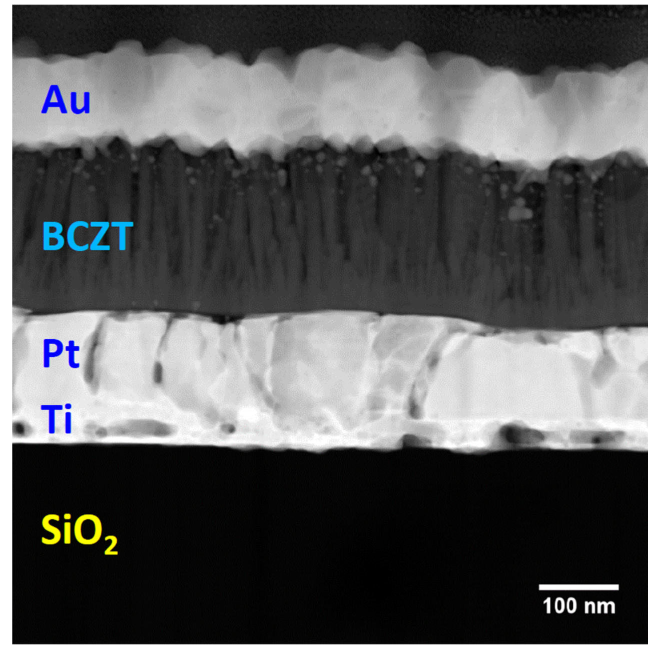

FIG. 2. Cross-sectional STEM image of a polycrystalline thin-film capacitor stack. The columnar grains in the BCZT film extend throughout the whole film thickness.

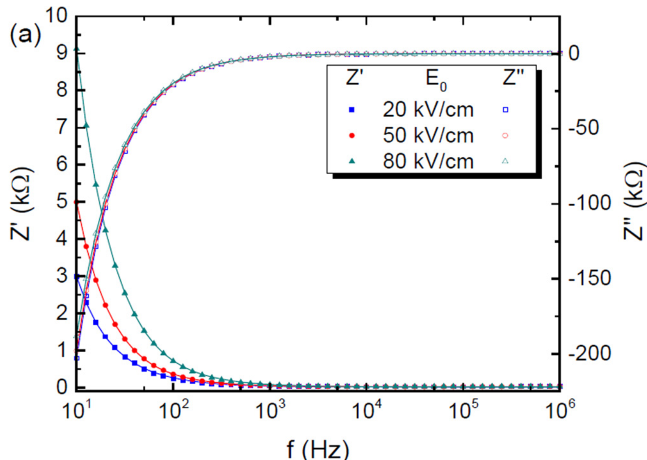

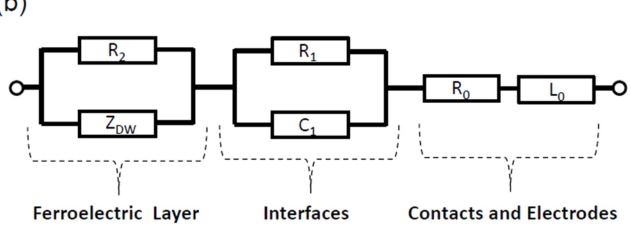

FIG. 3. (a) Bode plots $Z'(f)$ and $Z''(f)$ obtained by impedance spectroscopy (symbols) for different E_0 on the polycrystalline BCZT thin-film capacitor stack. The equivalent circuit in (b) was used to fit the data [solid lines in (a)].

their contribution cannot be separated by impedance spectroscopy,[15] which justifies modeling the BCZT layer as an R_2–Z_{DW} parallel circuit. Here, R_2 is attributed to losses due to possible leakage currents and Z_{DW} models the impedance of a ferroelectric due to domain-wall pinning and is given by[11]

$$Z_{DW}(f) = \frac{\varepsilon''_{r,0} - i\left[\varepsilon'_{r,0} + \Delta\varepsilon'_r \ln\left(\frac{1\,\text{Hz}}{2\pi f}\right)\right]}{2\pi f C_0\left\{\left[\varepsilon'_{r,0} + \Delta\varepsilon'_r \ln\left(\frac{1\,\text{Hz}}{2\pi f}\right)\right]^2 + \varepsilon''^2_{r,0}\right\}}, \tag{3}$$

with the geometrical capacitance C_0, which is for a parallel-plate capacitor configuration with plate distance d and electrode area A given by $C_0 = \varepsilon_0 A/d$, where ε_0 denotes the vacuum permittivity (here, $C_0 = 0.31$ nF). The fit parameters $\varepsilon'_{r,0}$, $\varepsilon''_{r,0}$, and $\Delta\varepsilon'_r$ describe the logarithmic frequency dispersion of the complex relative permittivity due to domain-wall pinning in a random energy landscape,[11,16,17]

$$\begin{aligned} \varepsilon'_r(f) &= \varepsilon'_{r,0} + \Delta\varepsilon'_r \ln\left(\frac{1\,\text{Hz}}{2\pi f}\right), \\ \varepsilon''_r(f) &= \varepsilon''_{r,0}, \end{aligned} \tag{4}$$

where $\varepsilon'_{r,0}$, $\varepsilon''_{r,0}$ denote static (i.e., frequency-independent) contributions to the dielectric response and $\Delta\varepsilon'_r$ is the logarithmic dispersion strength. It is important to note that the logarithmic frequency dispersion in Eq. (4) originates from the motion of internal modes (segments) of the domain walls and is quantified by the logarithmic dispersion strength $\Delta\varepsilon'_r$.[11,17] The motion of internal domain-wall segments has to be distinguished from the center-of-mass motion of the domain walls, and the superposition of both describes the domain-wall dynamics.[11,17]

Results of the fits can be seen in the Bode plot[14] shown in Fig. 3(a), where real and imaginary parts of the impedance $Z = Z' - iZ''$ are plotted vs frequency (for three values of E_0). In all cases, the fits are in good agreement with the measured data, indicating that the equivalent circuit used is a suitable model for the capacitor stacks. Note that the Bode plot of the impedance [cf. Fig. 3(a)] gives better insight into the frequency range below 1 kHz, where the impedance is dominated by the ferroelectric BCZT layer.[15] In addition, the Bode plot of the admittance $Y = 1/Z$—which highlights more the frequency range above 1 kHz—is given in Appendix B.

For field amplitudes $E_0 \leq 40$ kV/cm, the fitting procedure yields values for R_1 and C_1 in the range of $10^8\ \Omega$ and 10^9 F, respectively, and the other fit parameters remain unaffected by setting R_1 and C_1 to infinity. This corresponds to a vanishing interface contribution to the total impedance for excitation fields below $E_0 \leq 40$ kV/cm, which indicates that the Pt and Au electrodes are ideally polarizable and fully blocking in this field range. For higher fields, charge injection across the interface into the ferroelectric BCZT layer occurs, which results in finite values for the interface fit parameters R_1 and C_1 [cf. Table I]. Note that the electrode–film

Published under license by AIP Publishing.

TABLE I. Fit parameters for the polycrystalline BCZT capacitor stack at three different excitation-field amplitudes E_0.

E_0 (kV/cm)	R_0 (Ω)	R_1 (kΩ)	C_1 (μF)	R_2 (MΩ)	$\varepsilon_{r,0}'$	$\Delta\varepsilon_r'$	$\varepsilon_{r,0}''$	L_0 (μH)
20	18 ± 1	∞	∞	62.5 ± 1.9	258.1 ± 0.1	1.81 ± 0.01	2.86 ± 0.02	3.0 ± 0.8
50	22 ± 1	0.71 ± 0.03	11.6 ± 0.4	25.7 ± 0.4	266.2 ± 0.1	2.18 ± 0.03	3.76 ± 0.04	3.0 ± 0.5
80	19 ± 2	1.04 ± 0.05	6.5 ± 0.3	14.9 ± 0.3	284.0 ± 0.2	3.29 ± 0.06	8.46 ± 0.10	2.9 ± 1.1

interfaces with Pt and Au electrodes exhibit different blocking behavior than interfaces to conductive Nb-doped $SrTiO_3$ (Nb:STO) and Au electrodes investigated on an epitaxial BCZT capacitor stack, where charge injection into the BCZT layer was observed at significant lower field amplitudes down to 2.5 kV/cm .[11] We attribute this observation to different work functions of Pt and Nb:STO.[18] The work functions are 5.65 eV for Pt,[19] 3.9 eV for Nb:STO,[20] and 5.1 eV for Au,[19] which serves for both devices as a top electrode.

Fit parameters obtained from equivalent-circuit fits at three different excitation-field amplitudes are summarized in Table I. The standard errors are calculated from maximum likelihood estimation.[21]

Subsequently, the complex relative permittivity $\varepsilon_r(f)$ of the BCZT film was calculated from the obtained fit parameters according to Eq. (4) for each field amplitude E_0. The results for three different excitation-field amplitudes are depicted in Fig. 4(a). For comparison, the measured impedance of the entire capacitor stack is converted into permittivity data using the formalism described in Ref. 22, and the resulting $\varepsilon_{r,\text{stack}}(f)$ plots are shown in Fig. 4(b), together with the extracted permittivity of the BCZT layer. The permittivities $\varepsilon_r(f)$ and $\varepsilon_{r,\text{stack}}(f)$ are in good agreement for frequencies up to ~10 kHz (real part) and ~1 kHz (imaginary part). At higher frequencies (~10^5 Hz), the capacitor stack exhibits a Debye-like dielectric relaxation, which we attribute to resistive losses in the electrodes.[8] Note that this dielectric relaxation alters the dielectric spectrum of the capacitor stack by several orders of magnitude in this frequency range. For $E_0 = 80$ kV/cm, the real part of the permittivity of the capacitor stack is slightly lower (in the low-frequency range) compared to the permittivity of the BCZT layer, which is not the case for the depicted lowest field amplitude. We attribute this to charge injection at high fields, which results in a finite interfacial capacitance connected in series to the capacitance of the BCZT layer and hence lowers the capacitance of the stack.[23] Additionally, at $E_0 = 80$ kV/cm, the imaginary parts slightly deviate at the lowest frequencies (~10 Hz) due to the conductivity of the BCZT film.[8] Furthermore, we note that the slightly negative values of $\varepsilon'_{r,\text{stack}}(f)$ at frequencies around 1 MHz are due to the inductance of the cables used.[14] Obviously, the deconvolution of measured impedance spectra by appropriate equivalent-circuit fitting is mandatory to correctly extract the properties of the ferroelectric thin film.

From the obtained fit parameters, the field dependence of the dispersion parameters $\varepsilon'_{r,0}(E_0)$, $\varepsilon''_{r,0}(E_0)$, and $\Delta\varepsilon'_r(E_0)$ can be investigated, and the results are shown in Fig. 5. All dispersion parameters exhibit a linear dependence (with a positive slope) on the excitation-field amplitude E_0 within the threshold field E_T and the partial switching field E_{PS}. In analogy to the Rayleigh law[15,24,25]—which describes the linear dependence of complex relative permittivity on E_0—we denote the linear dependence of the dispersion parameters on E_0 with a positive slope as "Rayleigh-like behavior."[11]

Following the extended data analysis introduced in Ref. 11, the curves are fitted within the range 45 kV/cm ≤ E_0 ≤ 70 kV/cm as indicated by the dashed vertical lines [cf. Fig. 5] to the linear

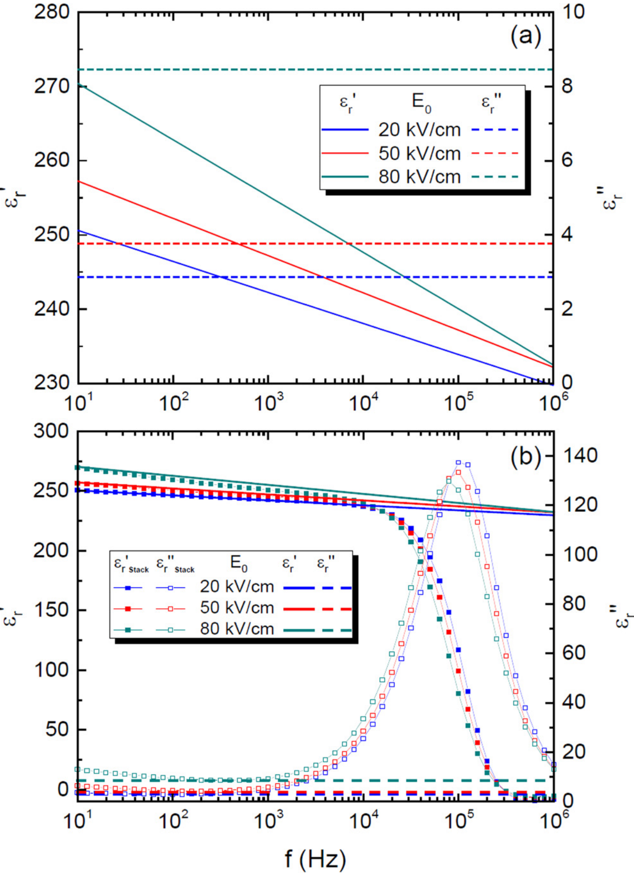

FIG. 4. (a) Extracted complex relative permittivity $\varepsilon_r(f)$ of the BCZT film for three different excitation-field amplitudes E_0. (b) Measured permittivities $\varepsilon'_{r,\text{stack}}(f)$ (full symbols) and $\varepsilon''_{r,\text{stack}}(f)$ (open symbols) of the entire capacitor stack for the same E_0 values. For clarity, the symbols are connected by thin lines, which do not represent fits to the data. For comparison, the extracted permittivities of the BCZT film are also shown (solid and dashed thick lines).

Published under license by AIP Publishing.

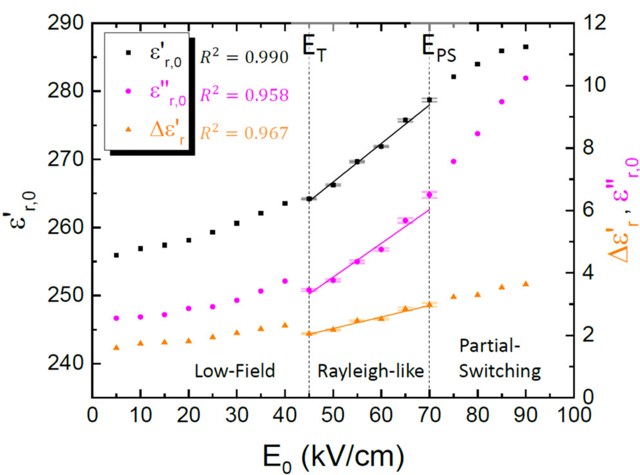

FIG. 5. Field dependence of the dispersion parameters $\varepsilon'_{r,0}(E_0)$, $\varepsilon''_{r,0}(E_0)$, and $\Delta\varepsilon'_r(E_0)$. The solid lines are linear fits in the region between the two vertical dashed lines, which mark the threshold field E_T and the partial switching field E_{PS}.

equations,

$$\begin{aligned} \varepsilon'_{r,0}(E_0) &= \varepsilon'_{r,\text{in},0} + \alpha'_0 E_0, \\ \varepsilon''_{r,0}(E_0) &= \varepsilon''_{r,\text{in}} + \alpha'' E_0, \\ \Delta\varepsilon'_r(E_0) &= \Delta\varepsilon'_{r,\text{in}} + \Delta\alpha' E_0. \end{aligned} \tag{5}$$

Here, the coefficients $\varepsilon'_{r,\text{in},0}$, $\varepsilon''_{r,\text{in}}$, α'_0, and α'' denote static contributions to the complex reversible (initial) Rayleigh parameter $\varepsilon_{r,\text{in}} = \varepsilon'_{r,\text{in}}(f) - i\varepsilon''_{r,\text{in}}$ and the complex irreversible Rayleigh parameter $\alpha = \alpha'(f) - i\alpha''$,[15,24,25] and $\Delta\varepsilon'_{r,\text{in}}$ and $\Delta\alpha'$ describe the logarithmic frequency dispersion strength of the Rayleigh parameters, given by[11,26]

$$\begin{aligned} \varepsilon'_{r,\text{in}}(f) &= \varepsilon'_{r,\text{in},0} + \Delta\varepsilon'_{r,\text{in}} \ln\left(\frac{1\,\text{Hz}}{2\pi f}\right), \\ \alpha'(f) &= \alpha'_0 + \Delta\alpha' \ln\left(\frac{1\,\text{Hz}}{2\pi f}\right). \end{aligned} \tag{6}$$

Note that $\Delta\alpha'$ corresponds to the coupling strength between the logarithmic frequency dispersion and the linear field dependence of permittivity.[11] Since a linear dependence of permittivity on the field amplitude E_0 results in a nonlinear dielectric polarization in E_0, this behavior is also referred to as dielectric nonlinearity.[25]

The starting point for the linear fits at $E_0 = 45\,\text{kV/cm} \equiv E_T$ was determined by the criterion that all subsequent data points are required to have a higher value compared to their left neighbor. The end point for the linear fits was then chosen by the longest fitting range for which every linear fit has a correlation factor $R^2 \geq 0.950$, which is fulfilled for $E_0 = 70\,\text{kV/cm} \equiv E_{PS}$. At higher fields, deviations from the linear behavior occur [cf. Fig. 5], which we attribute to the partial switching of domains.[24] For the linear fits, the estimated standard errors from the previous equivalent-circuit fitting procedure were taken into account, which is also indicated by the error bars within the fitting range [cf. Fig. 5]. The results of the fits according to Eq. (5) are summarized in Table II.

The Rayleigh constant α'_0—which is a quantitative measure for the mobility of the center-of-mass of the domain walls—is significantly lower as compared to what has been found for an epitaxial BCZT thin film of the same thickness.[11] This is attributed to the higher defect density in the polycrystalline BCZT film, i.e., the presence of grain boundaries.[27] However, we cannot rule out that also a variation in the domain-wall density[25] affects α'_0 for the two different films. Moreover, the coupling strength has a value of $\Delta\alpha' = 0.039\,\text{cm/kV}$, which is one order of magnitude lower as compared to the epitaxial BCZT film investigated in Ref. 11. Thus, we conclude that the reduced coupling strength originates from the presence of grain boundaries in the polycrystalline BCZT thin film. Additionally, the zero-field contribution $\Delta\varepsilon'_{r,\text{in}}$ to the logarithmic dispersion strength is reduced in the polycrystalline BCZT film, which indicates that the presence of grain boundaries also weakens the relaxational motion of internal modes of the domain walls.

Note that $\varepsilon''_{r,\text{in}}$ is not zero, which could be an indication for an internal bias or a stress field.[11,15] The internal bias field, induced by different work functions of the top and bottom electrode in a parallel-plate capacitor configuration, can be calculated according to Ref. 28, which yields a value of $-27.5\,\text{kV/cm}$. In contrast, the calculated internal bias field for the epitaxial capacitor stack in Ref. 11 has a value of 60 kV/cm. This suggests that the different signs of the calculated bias fields are reflected in the different signs of $\varepsilon''_{r,\text{in}}$ for the polycrystalline and the epitaxial device.

By inserting the fit parameters into Eq. (6), we obtain the frequency-dependent Rayleigh parameters for the polycrystalline BCZT film, and the results are depicted in Fig. 6. Here, the vertical dashed line at $f_R \sim 0.7\,\text{kHz}$ indicates the Rayleigh frequency[11] for the BCZT thin film. The Rayleigh frequency is part of the more general Rayleigh-like frequency range, which is characterized by positive values of the irreversible Rayleigh parameter $\alpha'(f)$. Within the Rayleigh-like frequency range, the center-of-mass of the domain walls can move irreversibly via hopping between different potential minima corresponding to the stochastic regime.[11] The second dashed line at $f_0 \sim 682\,\text{kHz}$ marks the region where the irreversible Rayleigh parameter $\alpha'(f)$ is zero and changes sign to negative values due to the coupling of dielectric nonlinearity and frequency dispersion. Note that the value of f_0 in the polycrystalline BCZT film is significantly higher compared to what has been found for the epitaxial counterpart in Ref. 11, which is due to the reduced coupling in the polycrystalline film. Interestingly, the value of the Rayleigh frequency f_R is similar in both films.

TABLE II. Extracted parameters from the linear fits according to Eq. (5). The estimated uncertainties from previous fitting steps were taken into account.

$\varepsilon_{r,\text{in},0}'$	α_0' (cm/kV)	$\varepsilon_{r,\text{in}}''$	α'' (cm/kV)	$\Delta\varepsilon_{r,\text{in}}'$	$\Delta\alpha'$ (cm/kV)
238.4 ± 0.4	0.565 ± 0.007	−1.54 ± 0.15	0.108 ± 0.003	0.37 ± 0.09	0.037 ± 0.002

Published under license by AIP Publishing.

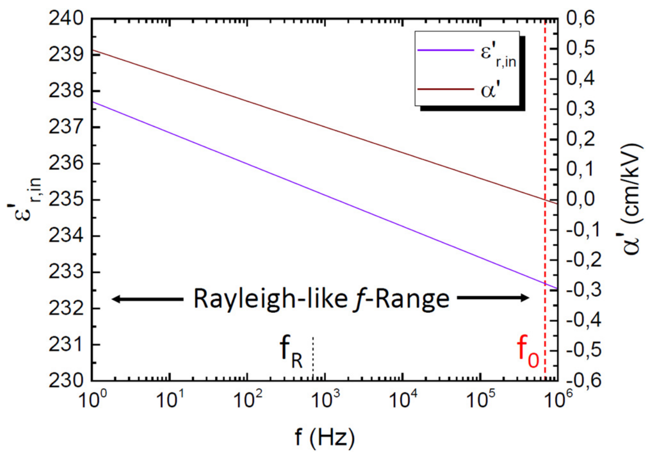

FIG. 6. Logarithmic frequency dispersion of reversible [$\varepsilon'_{r,in}(f)$] and irreversible [$\alpha'(f)$] Rayleigh parameters. The vertical dotted line at $f_R \sim 0.7$ kHz marks the Rayleigh frequency. The irreversible Rayleigh parameter changes to negative values at $f_0 \sim 682$ kHz, which is indicated by the vertical dashed line.

Finally, our analysis yields the schematic diagram depicted in Fig. 7 for the different domain-wall-motion regimes in the polycrystalline BCZT thin film. At field amplitudes $0 < E_0 < E_T$, the center of mass of the domain walls is pinned in a potential well of the random energy landscape; however, domain-wall segments can jump between metastable states with close energies, which corresponds to the non-coupled pinning regime.[11] By increasing the field amplitude above the threshold field $E_T = 45$ kV/cm, the center of mass of the domain walls can overcome the potential well and move irreversibly via hopping between different potential minima, resulting in a coexistence of irreversible center-of-mass motion and relaxational motion of internal domain-wall segments in the stochastic regime.[11] Note that the threshold field E_T in the polycrystalline thin film is significantly higher as compared to what has been reported for an epitaxial BCZT film of the same thickness,[11] which we attribute to the higher density of defects present in the polycrystalline film.[27] For field amplitudes above $E_{PS} = 70$ kV/cm, partial switching of the domains occurs. The irreversible Rayleigh parameter $\alpha'(f)$ becomes zero and changes to negative values at $f_0 \sim 682$ kHz, which originates from the coupling between dielectric nonlinearity and frequency dispersion.[11] This indicates a transition to the coupled pinning regime, where the center-of-mass of the domain walls cannot follow the fast driving field,[11,17,29] but domain-wall segments can still jump between metastable states.[11,17] However, the comprehensive domain-wall dynamics in the coupled pinning regime—which includes a negative irreversible Rayleigh parameter $\alpha'(f)$—is not precisely known, and more experimental and theoretical work is needed for an improved understanding.

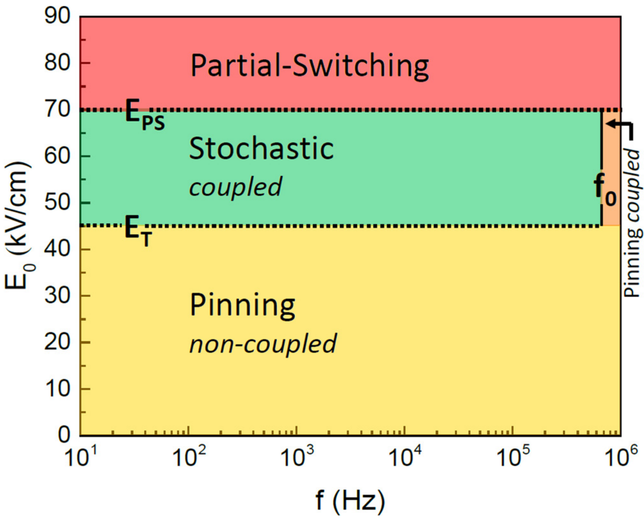

FIG. 7. Schematic diagram of the different domain-wall-motion regimes of the polycrystalline BCZT thin film. The threshold field $E_T = 45$ kV/cm and the partial switching field $E_{PS} = 70$ kV/cm are obtained from the field dependence of the dispersion parameters [cf. Fig. 5], and $f_0 \sim 682$ kHz is determined from the frequency dispersion of the irreversible Rayleigh parameter $\alpha'(f)$ [cf. Fig. 6].

IV. CONCLUSION

This work demonstrates the practical application of the novel domain-wall pinning element Z_{DW} to analyze the dielectric response and the domain-wall dynamics in polycrystalline BCZT thin films on platinized Si substrates. We report on the coupled dielectric response in the BCZT thin films, and we present a schematic diagram of the different domain-wall-motion regimes. Our results indicate that the presence of grain boundaries does not only reduce the value of the Rayleigh constant but also weakens the relaxational motion of internal domain-wall segments and the coupling strength between dielectric nonlinearity and frequency dispersion. Moreover, we reveal the superiority of the domain-wall pinning element Z_{DW} over the conventional approach to extract ferroelectric thin-film properties from impedance spectroscopy data.

Future work might be done by the controlled creation of point defects in ferroelectric films by focused He ion beam irradiation.[30,31] This may provide the possibility to tailor the permittivity and the underlying domain-wall dynamics in ferroelectric thin films, which is of practical importance for their application in various MEMS devices.

ACKNOWLEDGMENTS

We gratefully acknowledge technical support by M. Turad and R. Löffler (LISA$^+$). This work was partly funded by the Bundesministerium für Bildung und Forschung (BMBF) under Grant No. 13GW0123E and partly funded by the Europäische Fonds für regionale Entwicklung (EFRE) under Grant No. 712303.

APPENDIX A: VALIDATION OF IMPEDANCE SPECTRA

Impedance spectra might be afflicted with artifacts. To identify artifacts and reconstruct artifact-free (or less-artifact-afflicted)

Published under license by AIP Publishing.

spectra, approaches based on the Kramers–Kronig (KK) relations are used.[32,33] However, the KK relations are strictly defined within the frequency range between zero and infinity, whereas impedance measurements are performed in a finite frequency range. Thus, the extrapolation of the measured data is an unavoidable task and may lead to erroneous results, especially on the low-frequency side,[34] which is of central interest for the fits with the domain-wall pinning element. Therefore, we use here—in analogy to Ref. 15—the so-called Z-HIT (the two-pole Hilbert transform) as introduced in Ref. 34, which avoids the necessity of an extrapolation of the frequency range and allows one to reconstruct the modulus of impedance $|Z|$ vs f from the measured values of the less-artifact-prone[15,34] phase angle. The results of the Z-HIT for three different excitation-field amplitudes are depicted in Fig. 8. In all cases, the reconstructed curves match fairly well with the measured data, which indicates that the measured impedance spectra are not afflicted with artifacts and the investigated system is stable, causal, (sufficiently) linear[15] and exhibits finite values over the entire frequency range.

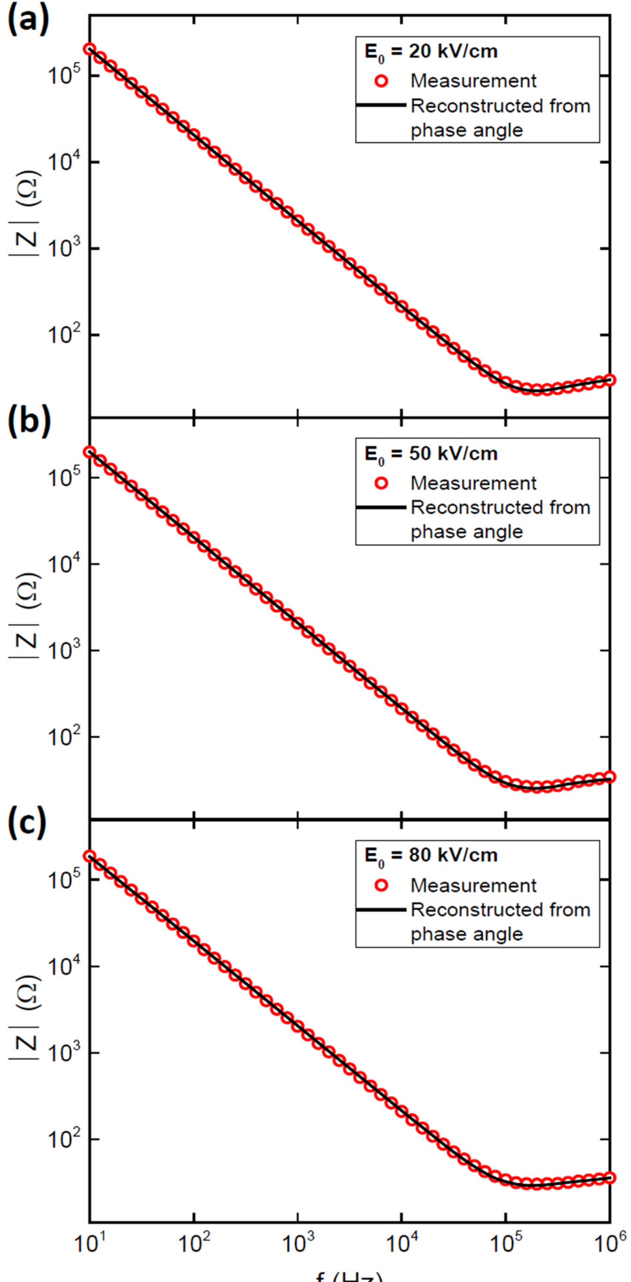

FIG. 8. Comparison of measured (symbols) and Z-HIT-reconstructed (black solid lines) impedance modulus $|Z|$ vs f for (a) $E_0 = 20\,\text{kV/cm}$, (b) $E_0 = 50\,\text{kV/cm}$, and (c) $E_0 = 80\,\text{kV/cm}$.

APPENDIX B: BODE PLOT OF THE ADMITTANCE

To better assess the quality of the equivalent-circuit fits in the frequency range above 1 kHz, real and imaginary parts of the admittance $Y = 1/Z$ are depicted in the Bode plot in Fig. 9. For frequencies up to $\sim 10^5$ Hz, the fits are in good agreement with the measured data. At higher frequencies, where the impedance is dominated by the (imperfect) electrodes[8] and possible interfacial contributions,[15] deviations increase. However, this frequency range is not of central interest for the fit with the domain-wall pinning element since the ferroelectric BCZT layer is more dominant at lower frequencies. This is also indicated by the good agreement in the lower frequency range between the measured permittivity of the capacitor stack and the permittivity of the BCZT layer extracted from equivalent-circuit fits with the domain-wall pinning element [cf. Fig. 4(b)].

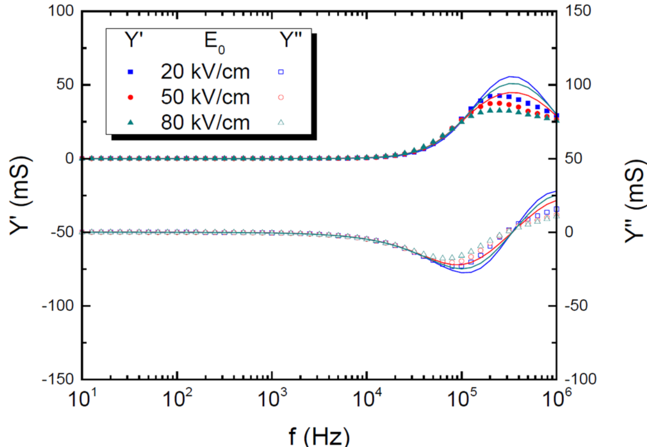

FIG. 9. Bode plots $Y'(f)$ and $Y''(f)$ obtained by impedance spectroscopy (symbols) and the corresponding equivalent-circuit fits (solid lines) for different E_0 on the polycrystalline BCZT thin-film capacitor stack.

Published under license by AIP Publishing.

DATA AVAILABILITY

The data that support the findings of this study are available from the corresponding author upon reasonable request.

REFERENCES

[1]S. Trolier-McKinstry and P. Muralt, "Thin film piezoelectrics for MEMS," J. Electroceram. **12**, 7 (2004).
[2]T. Xu, Z. Wang, J. Miao, L. Yu, and C. M. Li, "Micro-machined piezoelectric membrane-based immunosensor array," Biosens. Bioelectron. **24**, 638 (2008).
[3]T. D. Nguyen, N. Deshmukh, J. M. Nagarah, T. Kramer, P. K. Purohit, M. J. Berry, and M. C. McAlpine, "Piezoelectric nanoribbons for monitoring cellular deformations," Nat. Nanotechnol. **7**, 587 (2012).
[4]M. D. Nguyen, H. Nazeer, M. Dekkers, D. H. A. Blank, and G. Rijnders, "Optimized electrode coverage of membrane actuators based on epitaxial PZT thin films," Smart Mater. Struct. **22**, 085013 (2013).
[5]C. T. Q. Nguyen, M. D. Nguyen, M. Dekkers, E. Houwman, H. N. Vu, and G. Rijnders, "Process dependence of the piezoelectric response of membrane actuators based on $Pb(Zr_{0.45}Ti_{0.55})O_3$ thin films," Thin Solid Films **556**, 509 (2014).
[6]M. D. Nguyen, E. Houwman, M. Dekkers, D. Schlom, and G. Rijnders, "Enhancement of figure of merit for energy-harvesters based on free-standing epitaxial $Pb(Zr_{0.52}Ti_{0.48})_{0.99}Nb_{0.01}O_3$ thin-film cantilevers," APL Mater. **5**, 074201 (2017).
[7]M. Acosta, N. Novak, V. Rojas, S. Patel, R. Vaish, J. Koruza, G. A. Rossetti, and J. Rödel, "$BaTiO_3$-based piezoelectrics: Fundamentals, current status, and perspectives," Appl. Phys. Rev. **4**, 041305 (2017).
[8]M. Tyunina, "Size effects and dielectric behaviour in ferroelectric heterostructures," J. Phys.: Condens. Matter **18**, 5725 (2006).
[9]R. Schmidt, W. Eerenstein, T. Winiecki, F. D. Morrison, and P. A. Midgley, "Impedance spectroscopy of epitaxial multiferroic thin films," Phys. Rev. B **75**, 245111 (2007).
[10]R. Schmidt, J. Ventura, E. Langenberg, N. M. Nemes, C. Munuera, M. Varela, M. Garcia-Hernandez, C. Leon, and J. Santamaria, "Magnetoimpedance spectroscopy of epitaxial multiferroic thin films," Phys. Rev. B **86**, 035113 (2012).
[11]M. Becker, C. J. Burkhardt, R. Kleiner, and D. Koelle, "Field and frequency dependent dielectric response in ferroelectrics from impedance spectroscopy measurements: The domain wall pinning element," arXiv:2008.04786 (2020).
[12]D. S. Keeble, F. Benabdallah, P. A. Thomas, M. Maglione, and J. Kreisel, "Revised structural phase diagram of $(Ba_{0.7}Ca_{0.3}TiO_3)$–$(BaZr_{0.2}Ti_{0.8}O_3)$," Appl. Phys. Lett. **102**, 092903 (2013).
[13]A. Piorra, A. Petraru, H. Kohlstedt, M. Wuttig, and E. Quandt, "Piezoelectric properties of $0.5Ba(Zr_{0.2}Ti_{0.8})O_3$–$0.5(Ba_{0.7}Ca_{0.3})TiO_3$ ferroelectric lead-free laser deposited thin films," J. Appl. Phys. **109**, 104101 (2011).
[14]J. R. Macdonald and E. Barsoukov, *Impedance Spectroscopy*, 3rd ed. (Wiley, New York, 2018).
[15]T. Schenk, M. Hoffmann, M. Pesic, M. H. Park, C. Richter, U. Schroeder, and T. Mikolajick, "Physical approach to ferroelectric impedance spectroscopy: The Rayleigh element," Phys. Rev. Appl. **10**, 064004 (2018).
[16]T. Nattermann, Y. Shapir, and I. Vilfan, "Interface pinning and dynamics in random systems," Phys. Rev. B **42**, 8577 (1990).
[17]A. A. Fedorenko, V. Mueller, and S. Stepanow, "Dielectric response due to stochastic motion of pinned domain walls," Phys. Rev. B **70**, 224104 (2004).
[18]J. Wang, M. D. Nguyen, N. Gauquelin, J. Verbeeck, M. T. Do, G. Koster, G. Rijnders, and E. Houwman, "On the importance of the work function and electron carrier density of oxide electrodes for the functional properties of ferroelectric capacitors," Phys. Status Solidi RLL **14**, 1900520 (2020).
[19]C. Park, Y. Seo, J. Jung, and D.-W. Kim, "Electrode-dependent electrical properties of metal/Nb-doped $SrTiO_3$ junctions," J. Appl. Phys. **103**, 054106 (2008).
[20]W. Li, J. E. Kleibeuker, R. Wu, K. H. L. Zhang, C. Yun, and J. L. MacManus-Driscoll, "Insulating-to-conducting behavior and band profile across the $La_{0.9}Ba_{0.1}MnO_3$/Nb:$SrTiO_3$ epitaxial interface," Phys. Rev. B **96**, 165103 (2017).
[21]P. G. Hoel, *Introduction to Mathematical Statistics*, 3rd ed. (Wiley, New York, 1962).
[22]R. Gerhardt, "Impedance and dielectric spectroscopy revisited: Distinguishing localized relaxation from long-range conductivity," J. Phys. Chem. Solids **55**, 1491 (1994).
[23]L. J. Sinnamon, R. M. Bowman, and J. M. Gregg, "Investigation of dead-layer thickness in $SrRuO_3/Ba_{0.5}Sr_{0.5}$/Au thin-film capacitors," Appl. Phys. Lett. **78**, 1724 (2001).
[24]D. A. Hall, "Rayleigh behaviour and the threshold field in ferroelectric ceramics," Ferroelectrics **223**, 319 (1999).
[25]N. Bassiri-Gharb, I. Fujii, E. Hong, S. Trolier-McKinstry, D. V. Taylor, and D. Damjanovic, "Domain wall contributions to the properties of piezoelectric thin films," J. Electroceram. **19**, 49 (2007).
[26]D. Damjanovic, "Logarithmic frequency dependence of the piezoelectric effect due to pinning of ferroelectric-ferroelastic domain walls," Phys. Rev. B **55**, R649 (1997).
[27]C. Ma, B. Ma, S.-B. Mi, L. Liu, and J. Wu, "Enhanced dielectric nonlinearity in epitaxial $Pb_{0.92}La_{0.08}Zr_{0.52}Ti_{0.48}O_3$ thin films," Appl. Phys. Lett. **104**, 162902 (2014).
[28]M. Pesic, M. Hoffmann, C. Richter, T. Mikolajick, and U. Schroeder, "Nonvolatile random access memory and energy storage based on antiferroelectric like hysteresis in ZrO_2," Adv. Funct. Mater. **26**, 7486 (2016).
[29]F. Griggio, S. Jesse, A. Kumar, O. Ovchinnikov, T. N. Jackson, D. Damjanovic, S. V. Kalinin, and S. Trolier-McKinstry, "Substrate clamping effects on irreversible domain wall dynamics in lead zirconate titanate thin films," Phys. Rev. Lett. **108**, 157604 (2012).
[30]S. Saremi, R. Xu, F. I. Allen, J. Maher, J. C. Agar, R. Gao, P. Hosemann, and L. W. Martin, "Local control of defects and switching properties in ferroelectric thin films," Phys. Rev. Mat. **2**, 084414 (2018).
[31]S. Saremi, J. Kim, A. Ghosh, D. Meyers, and L. W. Martin, "Defect-induced (dis)order in relaxor ferroelectric thin films," Phys. Rev. Lett. **123**, 207602 (2019).
[32]M. Urquidi-Macdonald, S. Real, and D. D. Macdonald, "Applications of Kramers-Kronig transforms in the analysis of electrochemical impedance data—III. Stability and linearity," Electrochim. Acta **35**, 1559 (1990).
[33]P. Agarwal, M. E. Orazem, and L. H. Garcia-Rubio, "Application of measurement models to impedance spectroscopy III. Evaluation of consistency with the Kramers-Kronig relations," J. Electrochem. Soc. **142**, 1885 (1995).
[34]C. A. Schiller, F. Richter, E. Gülzow, and N. Wagner, "Validation and evaluation of electrochemical impedance spectra of systems with states that change with time," Phys. Chem. Chem. Phys. **3**, 374 (2001).

Published under license by AIP Publishing.

Publication III

Reproduced from J. Haas *et al.*, Sens. Mater. **32**, 2903 (2020); licensed under a Creative Commons Attribution (CC BY 4.0) license.

Sensors and Materials, Vol. 32, No. 9 (2020) 2903–2918
MYU Tokyo

S & M 2310

Sputtered Iridium Oxide as Electrode Material for Subretinal Stimulation

Jonas Haas,[1] Ralf Rudorf,[1] Maximilian Becker,[2] Renate Daschner,[1]
Anna Drzyzga,[1] Claus Burkhardt,[2] and Alfred Stett[1*]

[1]Retina Implant AG, Aspenhaustr. 25, 72770 Reutlingen, Germany
[2]NMI Natural and Medical Sciences Institute at the University of Tübingen,
Markwiesenstr. 55, 72770 Reutlingen, Germany

(Received April 14, 2020; accepted June 10, 2020)

Keywords: electrical stimulation, sputtered iridium oxide, neural prosthesis, retinal implant, microelectrodes

The efficiency and safety of neuronal stimulation with implants strongly depend on the electrode material. Microelectrodes composed of iridium oxide are becoming increasingly important as they exhibit excellent charge injection capacity (CIC) as well as charge storage capacity (CSC). We present the development of a robust process for the fabrication of sputtered iridium oxide films (SIROF). This process has been used for the "RETINA IMPLANT Alpha AMS" for several years of subretinal stimulation. In this paper, we describe the full experimental investigation of the electrode material. The electrochemical and morphological properties were investigated by cyclic voltammetry (CV), electrochemical impedance spectroscopy (EIS), voltage transient measurements, and focused ion beam-scanning electron microscopy (FIB-SEM). The implementation on the CMOS chip of the retinal prosthesis is presented. The deposition process window was investigated extensively. Major changes in process parameters lead to a difference in impedance of only 10% of the mean. Accelerated aging tests revealed a long-term stability of the electrodes of at least 10 years under conditions of use. The SIROF electrodes (diameter 30 µm) show low impedance (15.9 kΩ), excellent CSC (50.9 mC/cm^2), and high CIC (4.2 mC/cm^2). In summary, the robustness of the presented deposition process and the large process window enable the integration of high-quality SIROF microelectrodes in active implants and thus long-term stability in a wide range of safe electrical stimulation.

1. Introduction

Individuals who have lost their vision due to illness or other events now have the opportunity to regain a small portion of their visual functions with visual prostheses.(1) While cochlear implants have the longest and most successful history of neuronal prostheses,(2) retinal implants have also attracted interest and have undergone remarkable development in recent years.

*Corresponding author: e-mail: alfred.stett@okuvision.de
https://doi.org/10.18494/SAM.2020.2903

ISSN 0914-4935 © MYU K.K.
https://myukk.org/

All visual prostheses have one essential component in common: The stimulation electrodes provide the functional interface between the human body and the prosthesis. They pass the stimulating current into the surrounding neural tissue in order to evoke visual perception. Owing to their direct contact with retinal or brain tissue, they need to fulfill several requirements, such as biocompatibility as well as stability in biological environments over a long period of time. In addition, the electrochemical properties of the material should ensure the efficient and safe charge injection from the electrode into the tissue. Therefore, the material should offer low impedance to reduce power consumption,[3] high charge storage capacity (CSC), as well as high charge injection capacity (CIC).

Depending on the material, the charge injection mechanism can be capacitive or faradaic.[4] Faradaic electrodes, such as platinum or iridium oxide electrodes, typically transfer electrons across the electrode–electrolyte interface by reversible redox reactions at the interface and can provide a high amount of charge.[4] For efficient stimulation, the perceptual threshold of the adjoining neuronal cells has to be exceeded to initiate the signal cascade along the following neuronal cells and eventually trigger visual perception.[5] However, the stimulation strength should not exceed the electrochemical safety limit of the electrode material to prevent irreversible reactions, such as gas evolution, metal corrosion or dissolution, or the introduction of toxic reaction products that may lead to cell damage.[6,7] Thus, the maximum applied negative and positive voltages should not exceed the water window limiting the maximum CIC.

For cochlear implants, the American National Standard ANSI/AAMI CI86:2017 addresses the limit of safe stimulation. As for retinal implants, no such standard exists; thus, the cochlear standard can be taken as a guideline. By doing so, one has to consider the charge per electrode area, as well as per pulse phase. As already shown by Shannon in 1992,[8] the stimulation threshold between tissue damage and nondamage can be indicated by plotting the charge density (D) versus the charge per pulse (Q) in a double logarithmic plot. By inserting the histological evaluation of stimulation-induced tissue damage from a study of McCreery *et al.* in 1988,[6] we can express the threshold by Eq. (1).[8]

$$\log(D) = k - \log(Q) \tag{1}$$

The adjustable factor k is typically chosen to be between 1.5 and 2.0,[9] whereas ANSI/AAMI CI86:2017 recommends $k = 1.75$ for cochlear implants. Primarily, the Shannon equation is valid for macroelectrodes. However, even for microelectrodes with surface areas below 0.01 cm^2, the level of clinical stimulation remains within the safe area when using $k = 1.85$.[9]

Combining the electrochemical limit of the electrode material in terms of CIC with the safe region of stimulation determined by the Shannon equation [Eq. (1)] limits the range of stimulation for a specific electrode material. This is shown in Fig. 1 for some typical electrode materials. It becomes obvious that increasing the CIC expands the region of safe stimulation and thus allows not only the stimulation of cells with higher threshold, but also the use of smaller electrodes to increase the spatial selectivity. Small electrodes naturally have higher charge densities than large electrodes when injecting the same amount of charge.

Typical electrodes based on noble metals or titanium nitride show relatively low CIC[3,4] and are therefore unsuitable for safe stimulation with microelectrodes, especially when higher levels

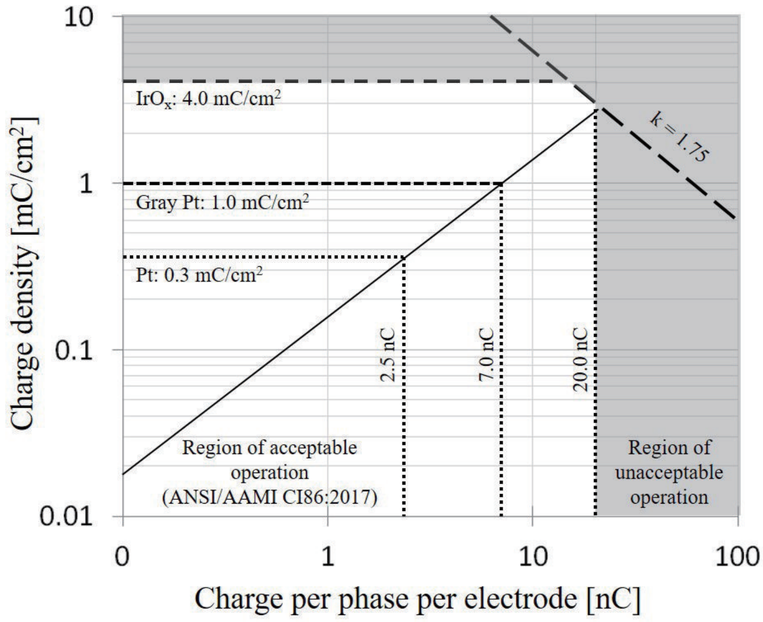

Fig. 1. Region of acceptable operation in terms of charge density versus charge per phase for electrical stimulation with microelectrodes. Safe CICs of various electrode materials are indicated by horizontal lines [platinum,(32) gray platinum,(33) IrO_x(3)]. For a microelectrode of 30 μm diameter, the corresponding maximum charges per phase are indicated by the vertical lines. The region of unacceptable operation for an IrO_x electrode (diameter 30 μm) is highlighted in gray.

of stimulation are required. In contrast, iridium oxide offers outstanding CIC and CSC as well as low impedance.(10,11)

Different routes for the fabrication of iridium oxide are known.(4,12) Sputtered iridium oxide films (SIROFs) are typically deposited by reactive sputtering from an iridium target. Thus, SIROFs can easily be implemented into the process routes of microsystem technologies and structured by standard lithography methods. Moreover, post-treatment of the as-prepared material in terms of electrochemical activation is not necessary, which is required for activated iridium oxide films (AIROFs). This is particularly advantageous for applications where the material is not easily accessible. For example, if the material is applied onto an application-specific integrated circuit (ASIC), the typical protocol for electrochemical activation(4) may not always be applicable.

In this work, we present the development and implementation of a SIROF material that has been used for the subretinal stimulation in humans using microelectrodes fabricated on the CMOS chip of the RETINA IMPLANT Alpha AMS.(13) This Conformité Européenne (CE)-marked medical device has been used for several years in clinical studies(14,15) and in every day life.(16) Starting with microelectrode arrays (MEAs) for developing the sputter process and investigating the electrochemical and morphological properties, the process is implemented into the fabrication routine of the retinal prosthesis. This work describes the full experimental examination of the electrode material by means of cyclic voltammetry (CV), electrochemical

impedance spectroscopy (EIS), and voltage transient measurements to estimate CIC. In addition, focused ion beam-scanning electron microscopy (FIB-SEM) is performed. The process window, i.e., the stability of the electrochemical properties, is shown by varying the parameters of the sputtering process. The implementation on the CMOS chip as used for the medical device is presented, and the long-term stability of the stimulation electrodes on the chip is tested in a laboratory environment using an accelerated aging test.

2. Materials and Methods

2.1 Sputter process

Deposition was performed in a DC magnetron sputtering system (von Ardenne LS 400 S, Dresden, Germany). Before the deposition, the substrate was cleaned by argon ion bombardment using a bias voltage of 500 V. A titanium adhesion layer was deposited at a chamber pressure of 5×10^{-3} mbar using a DC power of 350 W from a 4 inch titanium target (purity 99.8%) in argon atmosphere. Then, a certain pressure and power ramp were used to first deposit metallic iridium followed by iridium oxide sputtered from a 4 inch iridium target (purity 99.95%) in a reactive argon-oxygen atmosphere. Pressure was increased from 1×10^{-2} mbar without any oxygen to 5×10^{-2} mbar with an oxygen flow of 14 sccm. The applied DC power was decreased from 200 to 150 W. The process time was set to achieve an overall thickness of the electrode material of 650 nm, whereas the last, thickest, and most oxygen-rich layer is formed in the stack. These parameters represent the baseline process. To show the robustness of the sputter process, several process parameters (pressure, DC power, and thickness of the terminating IrO_x layer) were varied and the impact on the impedance was determined.

For the presented electrochemical investigations of the iridium oxide films, circular electrodes were deposited on MEAs, see Fig. 2(a). The fabrication of the stimulation electrodes on the CMOS chip of the RETINA IMPLANT Alpha AMS is schematically shown in Fig. 2(b). First, an 8-µm-thick AZ nLOF 2070 (Microchemicals, Ulm, Germany) lithography mask was used for the above-described sputter deposition of the electrode material followed by a lift-off process in TechniStrip NI555 (Microchemicals, Ulm, Germany). The stimulation electrodes were directly deposited on the contact holes of the CMOS chip. A protective polyimide layer of 5 µm thickness was spin-coated and patterned by reactive-ion etching (Oxford Plasmalab 800+, Abingdon, United Kingdom) to expose only the electrodes. The diameter of the electrodes on the MEA was chosen to be 30 µm corresponding to the diameter of the electrodes of the RETINA IMPLANT Alpha AMS.

Imaging of the electrode surface and cross section was carried out using a Zeiss Crossbeam 550 FIB-SEM system (Carl Zeiss Microscopy GmbH, Jena, Germany). To reduce the charging of the insulating MEA surface, the field emission electron column (Gemini 2) was operated at a beam energy of only 1.8 keV and frame averaging with drift compensation. To visualize the layer stack titanium-iridium-iridiumoxide, a cross section was prepared with the gallium FIB (Ionsculptor), first with a probe current of 30 nA @ 30 keV and final polishing with 700 pA.

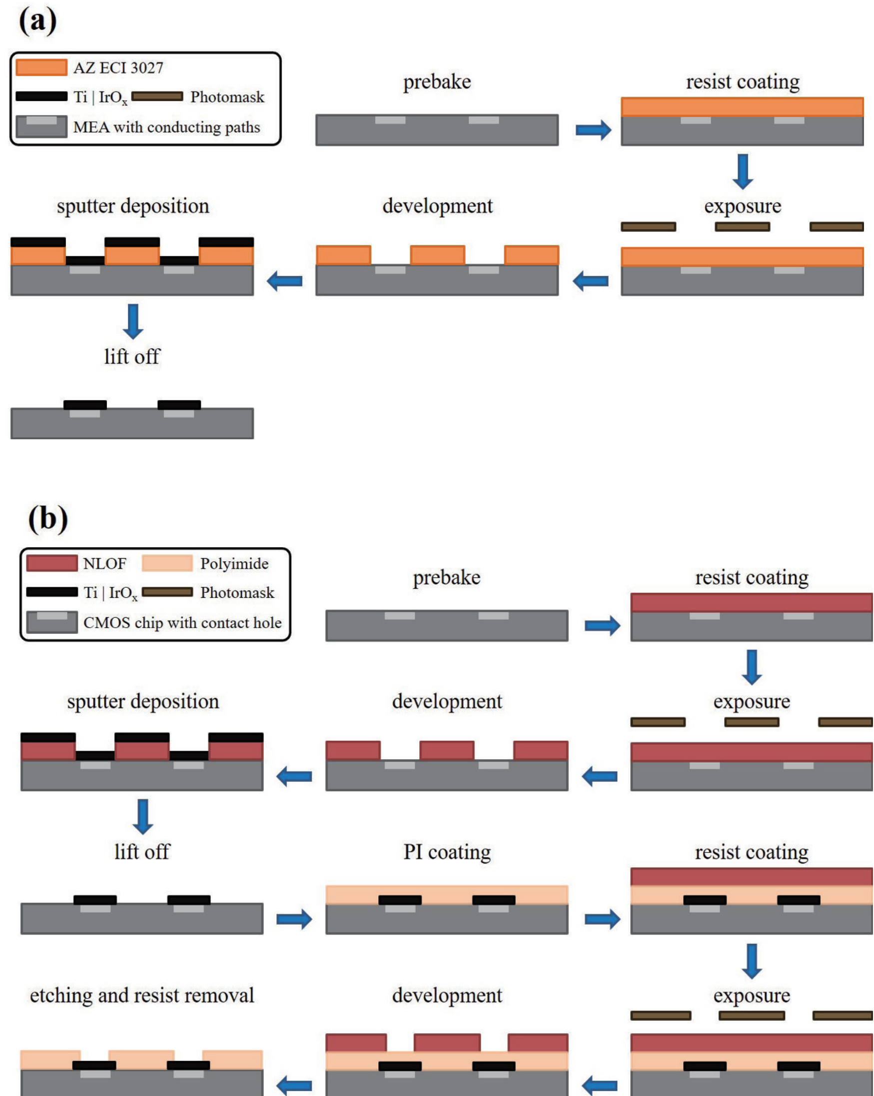

Fig. 2. (Color online) Schematic illustration of fabrication of iridium oxide electrodes on MEA for electrochemical and morphological examinations (a) and on CMOS chip as used for aging test and retinal prosthesis (b).

2.2 Electrochemical characterization

All electrochemical investigations were performed using the MEAs sputtered with the electrode material in accordance with the baseline process presented above. IR-drop-compensated CV was performed in phosphate-buffered saline (Gibco DPBS, pH 7.0–7.3, 8 g NaCl, 0.2 g KCl, 0.2 g KH_2PO_4, 2.16 g Na_2HPO_4*$(H_2O)_7$, each per l; Fresenius Kabi Deutschland GmbH, Bad Homburg, Germany; 66.7 Ω cm @ 21.7 °C) using a three-electrode configuration with the sputtered electrodes acting as working electrodes (multichannel potentiostat VMP3, Bio-Logic Science Instruments, Seyssinet-Pariset, France). A platinum mesh (Pt 99.95%, 1 × 1 cm^2, Labor-Platina, Pilisvörösvár, Hungary) was used as a counter electrode, and a Ag/AgCl electrode (InLab Reference, Mettler Toledo, Columbus, USA) was

used as a reference electrode. Measurements were performed from −600 to 700 mV at a sweep rate of 100 mVs^{-1}.

The same setup was used for EIS at an open-circuit voltage. The voltage amplitude was set to 5 mV in the frequency range from 0.1 Hz to 100 kHz with six points per decade. In addition, impedance was measured using the MEA-IT-System (Multi Channel Systems MCS GmbH, Reutlingen, Germany, Ag/AgCl reference electrode) by applying a sinusoidal test signal (100 mV, 1 kHz).

Voltage transient measurements were performed in DPBS (66.7 Ω cm @ 21.7 °C). As the RETINA IMPLANT Alpha AMS uses constant current pulses for stimulation, symmetric biphasic, cathodal-first pulses of 5, 10, 25, and 50 µA with a pulse duration of 2 ms were applied and the voltage drop at the electrodes was measured.

2.3 Long-term stability measurement

To prove the long-term stability of the sputtered iridium oxide as an electrode material, accelerated aging tests were performed. The material was deposited on the chip of the RETINA IMPLANT Alpha AMS as described above. The chip was operated in a laboratory environment at the maximum output voltage (±1.2 V) and submerged in DPBS at 60 °C. All electrodes were activated and were stimulating simultaneously. The output current was determined by measuring the voltage using a shunt resistance. Current was integrated over the pulse duration and divided by the number of pixels. Stimulation parameters typically used in clinical applications were used (2 ms each pulse width, 5 Hz stimulation frequency). The detailed setup and operation were described by Daschner *et al.*[13]

3. Results and Discussion

3.1 Robustness of sputtering process

The process stability was examined by varying one or more parameters while all other parameters were unchanged. The effects of the changes were characterized by measuring the impedance of the electrodes at 1 kHz. The process window tests included the following parameter changes:

1. Thickness variation: Increasing the thickness of the terminating iridium oxide by ~90% from 650 to 1250 nm decreased the impedance by 5% from 15.9 to 15.2 kΩ.
2. Pressure variation: The process pressure was increased by 20% from 5×10^{-2} to 6×10^{-2} mbar, resulting in an increase in the impedance by 2.5% to 16.3 kΩ.
3. Variations of pressure and thickness: The thickness of the terminating iridium oxide layer was increased by ~50% to 1000 nm and the process pressure was increased by 80% to 9×10^{-2} mbar, resulting in a decrease in the impedance by 7% to 14.8 kΩ.
4. Variations of thickness, pressure, and DC power: The thickness of the terminating iridium oxide layer was decreased by ~30% to 460 nm using a lower DC power of 50 W instead of 150 W, and the process pressure was increased to 9×10^{-2} mbar. This resulted in an increase in the impedance by ~10% to 17.4 kΩ.

5. DC pulse variation with short pulse duration: Instead of nonpulsed DC power, pulses with a frequency of 100 kHz and a duration of 0.4 μs were applied, resulting in an increase in the impedance by ~15% to 18.2 kΩ.
6. DC pulse variation with long pulse duration: Instead of nonpulsed DC power, pulses with a frequency of 100 kHz and a duration of 4 μs were applied, resulting in an increase in the impedance by ~10% to 17.6 kΩ.
7. Alloy-type transition between Ti and Ir: Instead of an abrupt transition between the adhesion layer and iridium, Ti-Ir alloys with increasing Ir content were sputtered, resulting in an increase in the impedance by ~5% to 16.6 kΩ.

All the parameter changes caused only small effects on the resulting impedance; thus, one can conclude that the baseline process already has well-selected parameters. Only the thickness increase of the IrO_X layer and pressure increase led to a small decrease in impedance. This can be explained by a larger inner volume because of the thicker material and the more cauliflower-like structure of IrO_X. No adjustment of the baseline process using these more advantageous parameters was made with regard to process time and stability in the sputtering system used. All other variations led to a small increase in impedance, but the overall differences in impedance were within 10% of the mean.

This proves the robustness of the baseline process and indicates a large process window, which is important for consistent quality in the fabrication of the electrode material and thus a consistent and safe stimulation with different implants. As a result, this deposition process is very well suited for the series production of active implantable medical devices, since even large deviations in the process parameters do not impair the quality of the electrode material.

3.2 Film morphology

The surface morphology of the sputtered iridium oxide electrode material after performing the electrochemical experiments is shown in Fig. 3(a). The bright area shows the deposited material in the electrode opening of the MEA. The rough surface indicates the increased surface area, which is desirable for stimulation.

The prepared cross section is shown in Fig. 3(b). The titanium adhesion layer (thickness, approx. 100 nm) cannot be distinguished from the titanium circuit path of the MEA itself. The Ir-IrO_X layer initially grows with a columnar morphology on the adhesion layer. Towards the top of the layer, the columnar morphology of the film changes into a cauliflower-like morphology.

The intended increase in the oxygen content can be seen in the results of energy-dispersive X-ray (EDX) spectroscopy shown in Fig. 4 (O Kα1). The same trend can be seen in the cross section, as the recorded signal becomes weaker (darker in the image) with increasing layer thickness. Thus, the cauliflower-like region corresponds to the highest oxygen content. As already reported in the literature, the electrochemical activation of the as-deposited iridium oxide electrode material by potential cycling leads to morphological changes of the activated region. Wessling *et al.*[17] indicated that the structural change is beneficial for charge injection as more redox centers can be reached by an ionic solution.

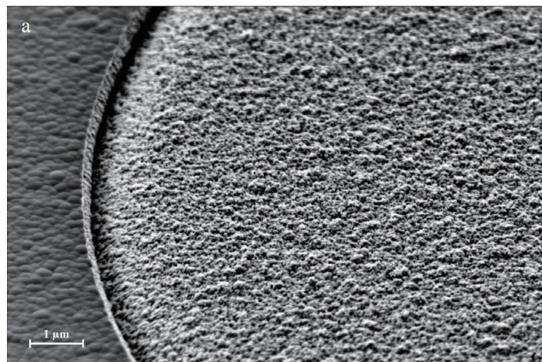

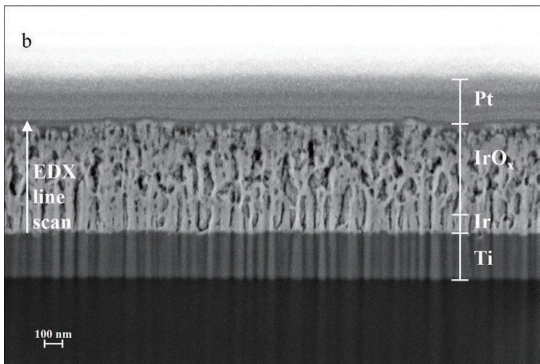

Fig. 3. SEM images of sputtered electrode material. (a) Rough surface of electrode material (bright area) deposited on MEA. (b) Cross section of electrode material prepared by FIB-SEM, showing the initially columnar and subsequently cauliflower-like structure of the electrode material. To protect the microstructure during the preparation of the cross section, a 200-nm-thick platinum protective top layer was deposited. The arrow indicates the direction of the performed EDX line scan across the Ir-IrO_x layer.

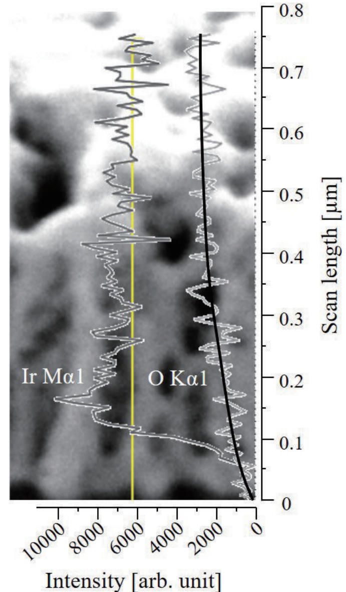

Fig. 4. (Color online) EDX spectroscopy of electrode cross section. The line scan along the Ir-IrO_x layer from bottom to top of the material is indicated by the yellow vertical line. For better illustration, a black trend line is plotted through the O Kα1 signal. An increase in oxygen content can be seen with increasing scan length.

3.3 Electrochemical properties

3.3.1 *CV* and *CSC*

The *CV* of the iridium oxide electrode material is shown for one electrode as an example in Fig. 5. The *CSC* is calculated by integrating the area under the curve according to Eq. (2),

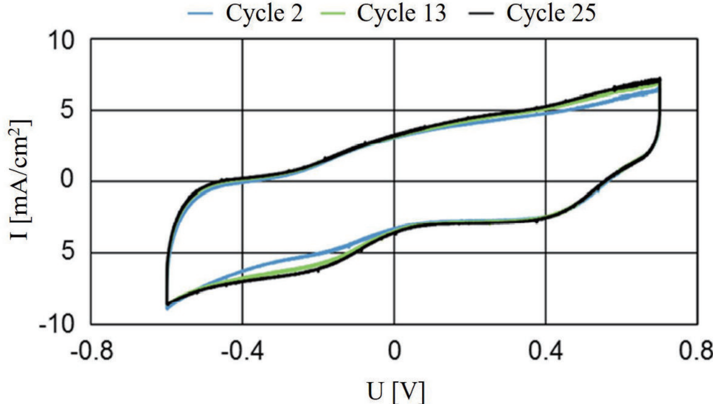

Fig. 5. (Color online) Cyclic voltammograms of SIROF electrode deposited on MEA during 2nd, 13th, and 25th cycles. Typical reduction and oxidation peaks for iridium oxide can be seen at −0.2 and 0.5 V, respectively. At these points, an increase in the area under the curve can be seen with increasing cycle number.

$$CSC = \int I v^{-1} dU, \tag{2}$$

with the current I, the potential U, and the sweep rate v for both positive (anodic, CSC_A) and negative voltage ramps (cathodic, CSC_C). Table 1 shows the calculated CSC values for eight electrodes.

As can easily be seen in the CV, the area under the curve increases with the number of cycles, typically next to the reduction and oxidation peaks (−0.2 and 0.5 V, respectively), which is due to the electrochemical activation of the iridium oxide material.[18] CSC_C increases to up to 50.9 mC/cm^2 after 25 cycles. Compared with the SIROF electrodes reported in the literature, the presented sputtering process results in similar CSC values at comparable sweep rates.[10–12,19–21] The high CSC can be attributed to the previously described morphology of the sputtered iridium oxide that represents a greatly increased and, in slow-sweep CV, accessible electrochemical surface.

Particularly when comparing the difference between pre- (i.e., cycle 2) and post-activations (i.e., cycle 25), the presented material is superior to a previously reported SIROF,[20] which initially exhibits only about 17% of the post-activated CSC_C. This is particularly advantageous when using the electrodes in a complex implant where no activation protocol can be performed before usage but still a high charge injection is required.

3.3.2 EIS

The EIS data are shown in Fig. 6(a). Here, the solid and dashed lines represent fits to the equivalent-circuit depicted in Fig. 6(b). The circuit is a complete model of the electrode–electrolyte interface[22] and includes the double-layer capacitance C_{DL}, the pseudo-capacitance C_P, the faradaic leakage resistance R_F, the charge transfer resistance R_{CT}, the Warburg

Table 1
CSC_C and CSC_A (mean and standard deviation) calculated from cyclic voltammograms for eight electrodes at the 2nd, 13th, and 25th cycles.

[mC/cm^2]	Cycle 2	Cycle 13	Cycle 25
CSC_A	35.0 ± 0.3	39.1 ± 0.3	40.5 ± 0.3
CSC_C	47.7 ± 0.5	49.6 ± 0.4	50.9 ± 0.4

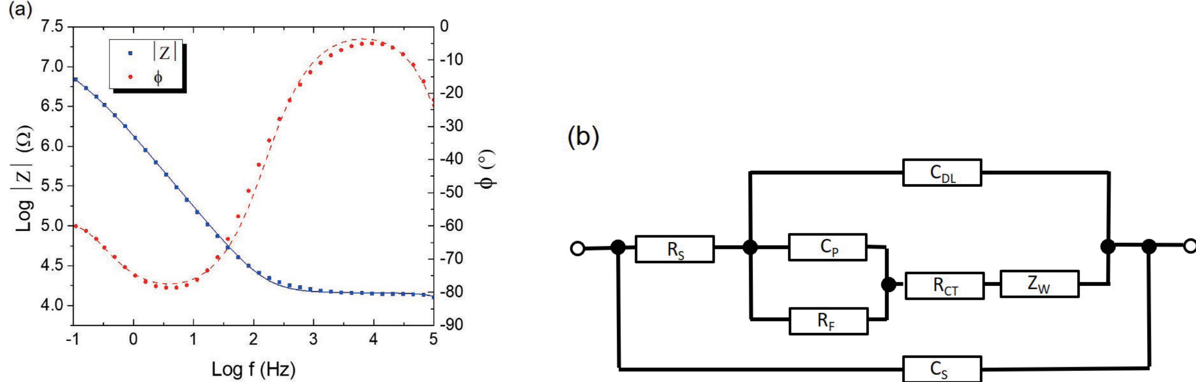

Fig. 6. (Color online) (a) Plot of impedance $|Z|(f)$ and phase $\phi(f)$ obtained by EIS (symbols) on SIROF microelectrode. (b) Equivalent circuit used for fitting the EIS data (solid and dashed line). R_S: series resistance, R_F: faradaic leakage resistance, C_P: pseudo-capacitance, R_{CT}: charge transfer resistance, Z_W: Warburg impedance, C_{DL}: double-layer capacitance, C_S: stray capacitance.

impedance Z_W, and the serial resistance R_S. Additionally, a parallel stray capacitance C_S was included, which is well-known to exist in three-electrode EIS measurements.[23] In our data, C_S causes the phase drop at high frequencies above 10 kHz.

The pseudo-capacitance C_P models the quasi-continuous, reversible faradaic reaction involving reduction and oxidation of Ir^{3+}/Ir^{4+} at the surface of the SIROF microelectrodes.[22,24] The Warburg impedance Z_W accounts for mass-transfer limitation by diffusion. Similarly to what has been used for other SIROF microelectrodes,[10] we used the Warburg element for finite-length diffusion with a reflecting boundary, as given by Eq. (3),[25]

$$Z_W(\omega) = R_D \frac{\coth\sqrt{i\omega T_D}}{\sqrt{i\omega T_D}}, \tag{3}$$

with the diffusion resistance R_D and the diffusion time constant T_D as free parameters. The double-layer capacitance C_{DL} and the pseudo-capacitance C_P are modelled by a constant phase element (CPE) respectively, which has the impedance given by Eq. (4).[25]

$$Z_{CPE}(\omega) = 1/Q(i\omega)^n \tag{4}$$

Here, Q and n are phenomenological parameters. The CPEs are used to model the non-ideal capacitive behavior of the double-layer capacitance C_{DL} and the pseudocapacitance C_P. For $n = 1$, the impedance in Eq. (4) simplifies to that of a linear capacitor.

The fit, see Fig. 6(a), is in good agreement with the measured EIS data over the full frequency range, indicating that the equivalent circuit shown in Fig. 6(b) is a valid description of the SIROF microelectrodes. The extracted fit parameters are shown in Table 2.

The values of the double-layer capacitance C_{DL} and the pseudo-capacitance C_P can be estimated from the fit parameters of the corresponding CPEs by using a standard procedure,[25] which yields $C_{DL} \approx 71$ nF and $C_{P0} \approx 208$ nF. As expected for SIROF microelectrodes, the pseudo-capacitance is significantly higher compared with the double-layer capacitance.[22,24] The resulting capacitive current flow at a sweep rate of 0.1 V/s through a parallel circuit of C_{DL} and C_P has a value of 3.94 mA/cm^2, which is in agreement with the measured CV data (see Fig. 5).

As mentioned earlier, impedance was additionally measured at 1 kHz using a commercial setup for impedance testing. Thereby, the impedance was determined to be 15.9 kΩ averaged over 59 electrodes on one MEA with a standard deviation of 320 Ω, which is in good agreement with EIS data at 1 kHz. The measurement was performed immediately after the deposition without prior potential cycling, which again showed the excellent properties of the as-deposited material. The determined impedance is similar to that of comparable materials described previously in the literature.[3,12,20]

3.3.3 Voltage transients and CIC

Voltage transient measurements were performed by applying four different currents (5, 10, 25, and 50 µA). The measurements are shown in Fig. 7. For each current, the maximum cathodal potential excursion (E_{mc}) is determined by subtracting the access voltage (V_a) from the maximum negative potential measured, i.e., the driving voltage (V_d).

To estimate the CIC, E_{mc} is interpolated as a function of the injected charge per electrode area for the data points close or above the voltage limit of the water window using a linear

Table 2
Extracted parameters from the equivalent-circuit fit to the measured EIS data depicted in Fig. 6. The stray capacitance C_S in the equivalent-circuit model was set to 50 pF. R_S: series resistance, R_F: faradaic leakage resistance; R_{CT}: charge transfer resistance, Q_{DL}, n_{DL}, Q_P, n_P: see text, C_{DL}: double-layer capacitance, C_P: pseudo-capacitance, R_D: diffusion resistance, T_D: diffusion time constant.

R_S (kΩ)	14.36 ± 2.00
R_F (MΩ)	71.9 ± 0.0
R_{CT} (MΩ)	11.3 ± 0.0
Q_{DL} ($\Omega^{-1}s^n$) × 10^{-9}	135.8 ± 0.2
n_{DL}	0.906 ± 0.002
C_{DL} (nF)	≈ 71
Q_P ($\Omega^{-1}s^n$) × 10^{-9}	191.2 ± 2.2
n_P	0.883 ± 0.008
C_P (nF)	≈ 208
R_D (Ω)	2616 ± 1
T_D (s)	0.015 ± 0.008

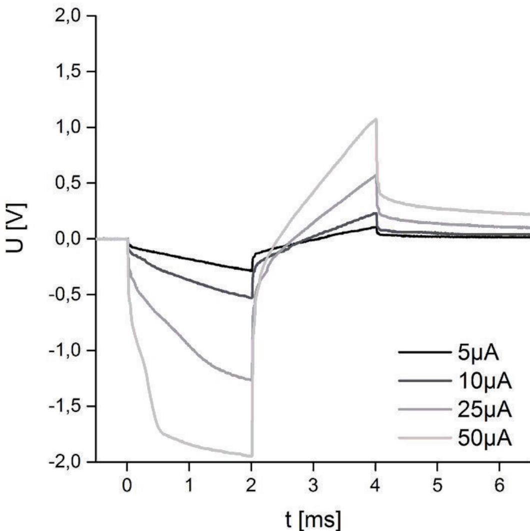

Fig. 7. Measurement of voltage transient by applying four different currents. At higher currents, the curve indicates that the water window is exceeded.

regression (see Fig. 8). This linear relationship was previously observed by Wang *et al.* in 2009.[21] Limiting the safe region of charge injection, the water window limit (−0.6 V) determines the maximum potential excursion (E_{mc}) that is allowed. Thus, the CIC for the presented iridium oxide electrode material was estimated to be about 4.2 mC/cm^2. Compared with previously published, comparable SIROFs, the CIC of the presented material is one of the highest in the literature.[3,4,7,10,21,26,27] This ensures the safe and efficient stimulation of neural tissues in a wide range of acceptable operations (Fig. 1). However, for the assessment of the safety of the use of implanted electrodes for electrical stimulation, it must be considered that the electrochemical properties of the electrodes differ *in vitro* and *in vivo*. The environment of an implanted electrode has a higher ionic resistance than the fluid used in laboratory testing. In addition, protein and cell adhesion may possess a diffusion limitation. As a result, the access resistance is higher *in vivo* and the CIC is lower *in vitro*, as comparative investigations with TiN,[28] Pt,[29] and IrO_x[30] electrodes have shown.

3.4 Long-term stability

The charge delivery of the electrode material during a long-term measurement carried out with the CMOS chip of the retinal prosthesis in a laboratory environment is shown in Fig. 9. The CMOS chip with the electrode material is operated using the same stimulation parameters as it is in the implant in the human body. The delivered charge is recorded during the lifetime of the test object.

In the first approximately 50 h of operation, a marked increase in the delivered charge per pixel can be observed. This is both to the complete wetting of the cauliflower-like structure of the electrode (Fig. 3) and the activation of SIROF electrodes.

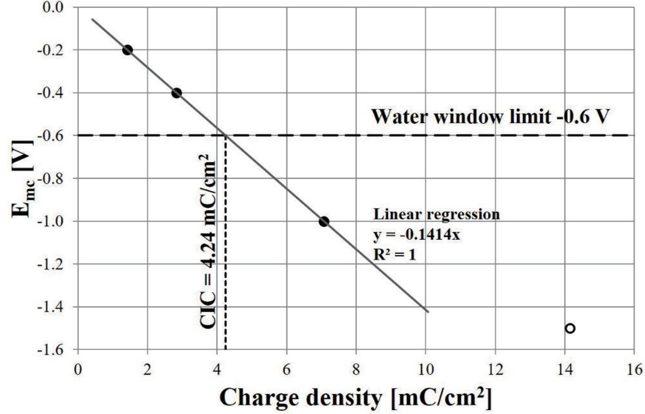

Fig. 8. Linear regression of estimated maximum potential excursion as a function of injected charge density. Only points above or close to the voltage limit (−0.6 V) are considered for the regression (filled symbol). The data point corresponding to the highest current value of 50 µA (empty symbol) shows a clear deviation from the linear relationship and was therefore excluded from the regression.

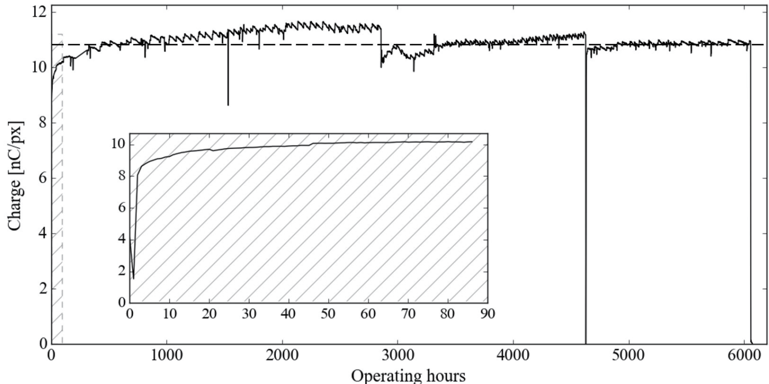

Fig. 9. Typical example of long-term measurement of charge per pixel delivered by the CMOS chip of the Retina Implant Alpha AMS in a laboratory environment at 60 °C. After activation, a stable charge injection can be observed over 6000 h of continuous operation (horizontal dashed line). Inset: Charge delivery during the first 90 h of operation.

The following small, almost linear increase is due to the evaporation of water out of the electrolyte and the associated increase in the ion concentration and conductivity of the electrolytic solution. The abrupt jump downward of the charge after an operation time of about 2800 h and 4700 h in the example shown in Fig. 9 is due to the filling-up with water and the related adjusted electrolyte concentration to compensate for water evaporation.

Neglecting these two effects, the electrode material delivers an almost constant charge over about 6000 h of continuous operation. This indicates the long-term stability of the iridium oxide electrodes in saline environments. In this example, the long-term test ended abruptly after about 6150 h owing to bondpad and PCB corrosion of the test object.

To determine the durability of the electrodes under conditions of use, a conversion factor between 60 °C (test condition) and 37 °C (body temperature) is assumed, which was determined for the RETINA IMPLANT Alpha AMS from tests in a laboratory environment and confirmed with clinical data in earlier work.[31] Since also here, the reason for failure was not the stimulation electrodes, it is legitimate to assume the same factor for the SIROF material. In fact, it even describes the minimum expected runtime. With the factor 4.92,[31] a runtime of approximately 30000 h of continuous operation at body temperature can be assumed. Conversion to the actual application in patients (8 h of operating time per day) show that the minimum expected lifetime of the IrO_x microelectrodes is at least 10 years under conditions of intended use.

4. Conclusions

We have presented the fabrication of the SIROF, which has been used clinically as the stimulation electrode material for several years now in the subretinal implant RETINA IMPLANT Alpha AMS. Both the development of the material on the MEA level and the implementation of the fabrication on the CMOS chip into the process routine of the retinal prosthesis are described.

The material is fully experimentally examined for its suitability as an electrode material. Therefore, the morphological and electrochemical properties of the electrode materials are investigated by FIB-SEM, CV, EIS, and voltage transient measurements. The presented SIROF shows low impedance as well as high CSC and CIC, which can be attributed to the film morphology. Variations of specific process parameters show only a small deviation of the impedance, indicating a very stable process with a large process window. This ensures the fabrication of high-quality films and thus safe and consistently strong stimulation by the retinal prosthesis in a wide range of acceptable operations in accordance with the American National Standard ANSI/AAMI CI86:2017. The electrode material exhibits long-term stability and stable charge injection in a laboratory environment over several months of continuous operation at an elevated temperature. By converting to body temperature and the actual operating time by patients, we found that the presented material allows stimulation for at least 10 years under conditions of intended use. All these properties taken together make the presented SIROF an excellent material predestined for the efficient and safe stimulation of neural tissues by microelectrodes imbedded in active implantable devices.

Acknowledgments

The authors would like to thank the Natural and Medical Sciences Institute at the University of Tübingen, Reutlingen, Germany, particularly Kai Fuchsberger and Thoralf Herrmann, for their work on CV, EIS, and voltage transient measurements.

References

1 E. Bloch, Y. Luo, and L. da Cruz: Ther. Adv. Ophthalmol. **11** (2019) 2515841418817501. https://doi.org/10.1177/2515841418817501
2 B. S. Wilson and M. F. Dorman: J. Rehab. Res. Dev. **45** (2008) 695. https://doi.org/10.1682/jrrd.2007.10.0173
3 J. D. Weiland, D. J. Anderson, and M. S. Humayun: IEEE Trans. Biomed. Eng. **49** (2002) 1574. https://doi.org/10.1109/TBME.2002.805487
4 S. F. Cogan: Annu. Rev. Biomed. Eng. **10** (2008) 275. https://doi.org/10.1146/annurev.bioeng.10.061807.160518
5 E. Zrenner, K. U. Bartz-Schmidt, H. Benav, D. Besch, A. Bruckmann, V. P. Gabel, F. Gekeler, U. Greppmaier, A. Harscher, S. Kibbel, J. Koch, A. Kusnyerik, T. Peters, K. Stingl, H. Sachs, A. Stett, P. Szurman, B. Wilhelm, and R. Wilke: Proc. R. Soc. B **278** (2011) 1489. https://doi.org/10.1098/rspb.2010.1747
6 D. B. McCreery, W. F. Agnew, T. G. Yuen, and L. A. Bullara: Ann. Biomed. Eng. **16** (1988) 463. https://doi.org/10.1007/BF02368010
7 S. Negi, R. Bhandari, L. Rieth, R. Van Wagenen, and F. Solzbacher: J. Neurosci. Methods **186** (2010) 8. https://doi.org/10.1016/j.jneumeth.2009.10.016
8 R. V. Shannon: IEEE Trans. Biomed. Eng. **39** (1992) 424. https://doi.org/10.1109/10.126616
9 S. F. Cogan, K. A. Ludwig, C. G. Welle, and P. Takmakov: J. Neural Eng. **13** (2016) 021001. https://doi.org/10.1088/1741-2560/13/2/021001
10 X. Kang, J. Liu, H. Tian, B. Yang, Y. NuLi, and C. Yang: Sens. Actuators, B **225** (2016) 267. https://doi.org/10.1016/j.snb.2015.11.050
11 C.-Y. Wu, P.-H. Kuo, P.-K. Lin, P.-C. Chen, W.-J. Sung, J. Ohta, T. Tokuda, and T. Noda: Sens. Mater. **30** (2018) 193. https://doi.org/10.18494/sam.2018.1664
12 X. Kang, J. Liu, H. Tian, B. Yang, Y. NuLi, and C. Yang: J. Micromech. Microeng. **24** (2014) 025015. https://doi.org/10.1088/0960-1317/24/2/025015
13 R. Daschner, A. Rothermel, R. Rudorf, S. Rudorf, and A. Stett: Sens. Mater. **30** (2018) 179. https://doi.org/https://doi.org/10.18494/SAM.2018.1726
14 T. L. Edwards, C. L. Cottriall, K. Xue, M. P. Simunovic, J. D. Ramsden, E. Zrenner, and R. E. MacLaren: Ophthalmology **125** (2018) 432. https://doi.org/10.1016/j.ophtha.2017.09.019
15 K. Stingl, R. Schippert, K. U. Bartz-Schmidt, D. Besch, C. L. Cottriall, T. L. Edwards, F. Gekeler, U. Greppmaier, K. Kiel, A. Koitschev, L. Kühlewein, R. E. MacLaren, J. D. Ramsden, J. Roider, A. Rothermel, H. Sachs, G. S. Schröder, J. Tode, N. Troelenberg, and E. Zrenner: Front. Neurosci. **11** (2017) 445. https://doi.org/10.3389/fnins.2017.00445
16 J. Cehajic Kapetanovic, N. Troelenberg, T. L. Edwards, K. Xue, J. D. Ramsden, A. Stett, E. Zrenner, and R. E. MacLaren: Acta Ophthalmol. (2020). https://doi.org/10.1111/aos.14443
17 B. R. Wessling, A. Besmehn, W. Mokwa, and U. Schnakenberg: J. Electrochem. Soc. **154** (2007) F83. https://doi.org/10.1149/1.2713691
18 S. F. Cogan, T. D. Plante, and J. Ehrlich: Conf. Proc. IEEE Eng. Med. Biol. Soc. **6** (2004) 4153. https://doi.org/10.1109/IEMBS.2004.1404158
19 S. F. Cogan, J. Ehrlich, T. D. Plante, M. D. Gingerich, and D. B. Shire: IEEE Trans. Biomed. Eng. **57** (2010) 2313. https://doi.org/10.1109/TBME.2010.2050690
20 X. Kang, J.-Q. Liu, H.-C. Tian, B. Yang, Y. NuLi, and C.-S. Yang: Conf. Proc. IEEE Eng. Med. Biol. Soc. (2014) 478. https://doi.org/10.1109/EMBC.2014.6943632
21 K. Wang, C. C. Liu, and D. M. Durand: IEEE Trans. Biomed. Eng. **56** (2009) 6. https://doi.org/10.1109/TBME.2008.926691
22 Z. Chen, L. Ryzhik, and D. Palanker: Phys. Rev. Appl. **13** (2020) 014004. https://doi.org/10.1103/PhysRevApplied.13.014004
23 M. Balabajew and B. Roling: Electrochim. Acta **176** (2015) 907. https://doi.org/10.1016/j.electacta.2015.07.074
24 A. van Ooyen, V. G. Zagolla, C. Ulrich, and U. Schnakenberg: Procedia Chem. **1** (2009) 269. https://doi.org/10.1016/j.proche.2009.07.067
25 V. F. Lvovich, Impedance Spectroscopy: Applications to Electrochemical and Dielectric Phenomena (Wiley, Hoboken, New Jersey, 2012). https://doi.org/10.1002/9781118164075
26 A. Ghazavi, J. Maeng, M. Black, S. Salvi, and S. F. Cogan: J. Neural. Eng. **17** (2020) 016022. https://doi.org/10.1088/1741-2552/ab52ab
27 J. Maeng, B. Chakraborty, N. Geramifard, T. Kang, R. T. Rihani, A. Joshi-Imre, and S. F. Cogan: J. Biomed. Mater. Res. Part B **108** (2020) 880. https://doi.org/10.1002/jbm.b.34442
28 S. Meijs, C. Sorensen, S. Sorensen, K. Rechendorff, M. Fjorback, and N. J. Rijkhoff: J. Neural Eng. **13** (2016) 026011. https://doi.org/10.1088/1741-2560/13/2/026011

29 R. T. Leung, M. N. Shivdasani, D. A. X. Nayagam, and R. K. Shepherd: IEEE Trans. Biomed. Eng. **62** (2015) 849. https://doi.org/10.1109/TBME.2014.2366514

30 S. F. Cogan: 2006 Int. Conf. IEEE Engineering in Medicine and Biology Soc. **2006** (2006) 882. https://doi.org/10.1109/iembs.2006.259654

31 R. Daschner, U. Greppmaier, M. Kokelmann, S. Rudorf, R. Rudorf, S. Schleehauf, and W. G. Wrobel: Biomed. Microdevices **19** (2017) 7. https://doi.org/10.1007/s10544-017-0147-6

32 S. B. Brummer, L. S. Robblee, and F. T. Hambrecht: Ann. N.Y. Acad. Sci. **405** (1983) 159. https://doi.org/10.1111/j.1749-6632.1983.tb31628.x

33 D. D. Zhou and R. J. Greenberg: Microelectronic Visual Prostheses: In Implantable Neural Prostheses (Springer, New York, 2009) p. 1. https://doi.org/10.1007/978-0-387-77261-5_1

Publication IV

Reproduced from Maximilian T. Becker AIP Advances **11**, 065106 (2021); licensed under a Creative Commons Attribution (CC BY 4.0) license.

AIP Advances

Charge injection capacity of ferroelectric microelectrodes for bioelectronic applications

Cite as: AIP Advances **11**, 065106 (2021); https://doi.org/10.1063/5.0049202
Submitted: 16 April 2021 . Accepted: 14 May 2021 . Published Online: 02 June 2021

Maximilian T. Becker

ARTICLES YOU MAY BE INTERESTED IN

Rayleigh analysis and dielectric dispersion in polycrystalline $0.5(Ba_{0.7}Ca_{0.3})TiO_3$–$0.5Ba(Zr_{0.2}Ti_{0.8})O_3$ ferroelectric thin films by domain-wall pinning element modeling
Journal of Applied Physics **128**, 154103 (2020); https://doi.org/10.1063/5.0025109

Next generation ferroelectric materials for semiconductor process integration and their applications
Journal of Applied Physics **129**, 100901 (2021); https://doi.org/10.1063/5.0037617

Fully epitaxial ferroelectric ScAlN grown by molecular beam epitaxy
Applied Physics Letters **118**, 223504 (2021); https://doi.org/10.1063/5.0054539

© 2021 Author(s).

Charge injection capacity of ferroelectric microelectrodes for bioelectronic applications

Cite as: AIP Advances 11, 065106 (2021); doi: 10.1063/5.0049202
Submitted: 16 April 2021 • Accepted: 14 May 2021 •
Published Online: 2 June 2021

View Online

Export Citation

CrossMark

Maximilian T. Becker[a)]

AFFILIATIONS

NMI Natural and Medical Sciences Institute, Markwiesenstr. 55, 72770 Reutlingen, Germany and Physikalisches Institut, Center for Quantum Science (CQ) and LISA+, University of Tübingen, Auf der Morgenstelle 14, 72076 Tübingen, Germany

[a)]Author to whom correspondence should be addressed: mtb57@cam.ac.uk

ABSTRACT

We analyze the extracellular stimulation current and the charge injection capacity (CIC) of microelectrodes coated with an insulating layer to prevent toxic electrochemical effects in bioelectronic applications. We show for a microelectrode coated with an insulating ferroelectric layer that the ferroelectric polarization current contributes to the extracellular stimulation current. Depending on the remanent polarization P_r of the ferroelectric, the polarization current in the switching regime can increase the CIC by up to two orders of magnitude as compared to the commonly used extracellular capacitive stimulation with microelectrodes that are coated with a dielectric layer.

© 2021 Author(s). All article content, except where otherwise noted, is licensed under a Creative Commons Attribution (CC BY) license (http://creativecommons.org/licenses/by/4.0/). https://doi.org/10.1063/5.0049202

Extracellular electrical stimulation of neurons and recording of neural activity are the basic principles for many *in vivo* applications such as implantable neuroprosthetic devices.[1] Among them are cochlear implants, retinal implants, deep brain stimulation for the treatment of Parkinson's disease, and brain-machine interfaces.[2–7] Moreover, extracellular electrical stimulation and recording are also key elements for *in vitro* applications, e.g., drug testing and the study of neural networks by microelectrode arrays (MEAs).[8,9]

Typically, electrically active implants and MEAs utilize conductive (metallic) microelectrodes with <100 μm diameter to provide the electro-neural interface for extracellular recording and stimulation.[1] In general, the main advantage of conductive microelectrodes is their high charge injection capacity (CIC), which is defined as the amount of injected charge density across the electrode–electrolyte interface during the leading stimulation phase of an extracellular current.[1] Note that the stimulation efficacy of a microelectrode is commonly quantified by the CIC.[1] Nonetheless, also the time curve of an extracellular current provided by a microelectrode can have an impact on their stimulation efficacy,[10] which should be kept in mind. Exemplary materials for the fabrication of conductive microelectrodes are Pt for high-density MEA applications[9] and IrO_2, which is utilized, e.g., in state-of-the-art retinal prostheses[4,11] and which can provide a CIC typically in the range of 1–5 mC/cm^2.[1,11,12]

The major disadvantage of conductive microelectrodes is the difficulty in avoiding electrochemical reactions (Faradaic processes) at the electrode–electrolyte interface, which induce corrosion of electrodes and cell or tissue damage[13] and hence detrimentally affect the safety and long-term-stability of implantable neuroprosthetic devices. A possible solution to prevent toxic electrochemical effects is the utilization of microelectrodes coated with a (thin) dielectric material. This approach was crucial for the first realization of a silicon–neuron junction, where *p*-doped areas of the utilized silicon chip were covered with a 10-nm-thick dielectric layer of SiO_2 to prevent Faradaic processes and to stimulate the attached neuron by purely capacitive currents across the dielectric–electrolyte interface.[14]

Modern capacitive biochips for extracellular electrical stimulation are fabricated in complementary metal–oxide–semiconductor (CMOS) technology and include field-effect transistors to record electrical signals from individual neurons,[15] which enables bidirectional communication between neurons and active silicon chips.[16] However, despite extensive research on dielectric coatings to enhance the purely capacitive stimulation with microelectrodes, their CIC is still in the range of ~1–5 μC/cm^2,[16–20] which is approximately three orders of magnitude lower than the CIC of generic conductive microelectrodes. Since the stimulation-threshold for the injected charge density depends on the geometric area of the microelectrode,[21] the CIC of capacitive microelectrodes is too low to achieve efficient extracellular stimulation with small microelectrodes (diameter ~30 μm), which requires a CIC in the range of

© Author(s) 2021

0.1–0.9 mC/cm^2,[21] although a tight tissue–electrode contact can lower the stimulation-threshold.[19] As a consequence, implantable neuroprosthetic devices utilize conductive metal-based microelectrodes although the absence of toxic electrochemical effects is highly desired in active electrical implants. In this paper, we introduce an approach to significantly increase the CIC of insulated microelectrodes for efficient and long-term stable bioelectronic interfacing of electrogenic cells or tissue.

In general, extracellular electrical stimulation is achieved by the flow of ionic current between a microelectrode in close proximity to the target excitable cell or tissue and a counter electrode immersed in the electrolyte, which contains the cell or tissue.[1] The ionic current flow in proximity to the cell or tissue causes depolarization of the cell membrane, which evokes an action potential above a specific threshold. A schematic experimental setup for the extracellular electrical stimulation of electrogenic cells or tissue with insulated microelectrodes in a parallel-plate configuration with an insulator thickness d is depicted in Fig. 1. Here, an applied voltage signal $U(t)$ generates an electric field $\mathbf{E}(t)$ across the insulating layer, which results in the occurrence of bound polarization charges at the surface of the insulator. As a consequence, a flow of free charges in the electrolyte is generated to screen the bound polarization charges, and this ionic current corresponds to the extracellular stimulation current. A simple stimulation signal is a voltage step $U(t) = U_0\Theta(t)$, where Θ denotes the Heaviside function. Other generic voltage signals for extracellular stimulation are rectangular voltage pulses with stimulation time $T_{\text{stim}} \sim 1$ ms, which are utilized in retinal implants[3] or deep brain stimulation.[6]

In the following, we will analyze the experimental setup for extracellular electrical stimulation with insulated microelectrodes (cf. Fig. 1) within the framework of macroscopic electrodynamics.[22] We make the assumption that every vector quantity $\mathbf{V}$ is fully described by its component V normal to the plane of the insulating layer and all other components vanish. The focus of our analysis will be the insulating layer depicted in Fig. 1, which is described by the electric displacement field $\mathbf{D}$ defined as[22]

$$\mathbf{D} = \varepsilon_0\mathbf{E} + \mathbf{P}, \tag{1}$$

with ε_0 being the vacuum permittivity and $\mathbf{P}$ being the electrical polarization. We assume that the insulating layer has an infinite Ohmic resistance, which requires the absence of free charges, i.e., $\nabla \cdot \mathbf{D} = 0$. We now consider Ampère's law, which is part of the macroscopic Maxwell equations and is given by[22]

$$\nabla \times \mathbf{H} = \mathbf{J} + \frac{\partial \mathbf{D}}{\partial t}, \tag{2}$$

with $\mathbf{H}$ being the magnetic field strength, $\mathbf{J}$ being the conduction current density, and $\partial\mathbf{D}/\partial t$ being the time derivative, which corresponds to the density of Maxwell's displacement current. Due to the insulation of the conductive microelectrode (cf. Fig. 1), electrochemical (Faradaic) charge transport is suppressed, which results in a vanishing conduction current density $\mathbf{J}$, as shown in Eq. (2). Thus, the extracellular stimulation current density $\mathbf{J}_{\text{stim}}$ provided by an insulated microelectrode corresponds to the displacement current density, i.e., $\mathbf{J}_{\text{stim}} = \partial\mathbf{D}/\partial t$, and by definition, the CIC can be calculated according to

$$\begin{aligned}\text{CIC} &= \left|\int_0^{T_{\text{stim}}} J_{\text{stim}}\,dt\right| \\ &= \left|\int_0^{T_{\text{stim}}} \frac{\partial D}{\partial E}\frac{\partial E}{\partial t}\,dt\right| \\ &= \left|\int_{\text{E}(0)}^{\text{E}(\text{T}_{\text{stim}})} \frac{\partial D}{\partial E}\,dE\right| \\ &= |D_{\max} - D_{\text{init}}|,\end{aligned} \tag{3}$$

with $D_{\max} \equiv D[E(T_{\text{stim}})]$ being the maximum displacement field and $D_{\text{init}} \equiv D[E(0)]$ being the initial displacement field. It follows from Eq. (3) that the CIC for an insulated microelectrode can be quantified from the knowledge of the D vs E—or equivalently the D vs U—relationship of the insulator.

The common extracellular capacitive stimulation utilizes an insulating layer, which consists of a material with solely dielectric properties. In linear approximation, the electrical polarization of a dielectric material is given by[22]

$$\mathbf{P}(\mathbf{E}) = \varepsilon_0(\varepsilon_r - 1)\mathbf{E} \equiv \mathbf{P}^{(\text{DE})}, \tag{4}$$

where ε_r denotes the relative permittivity of the material. Inserting Eq. (4) in Eq. (1) yields the linear relationship

$$\mathbf{D}(\mathbf{E}) = \varepsilon_0\varepsilon_r\mathbf{E}. \tag{5}$$

By introducing the specific capacitance $C_s \equiv \varepsilon_0\varepsilon_r/d$, the resulting capacitive stimulation current density in response to a time-varying electric field $E(t) = U(t)/d$ is then given by

$$J_{\text{stim}} = C_s\frac{\partial}{\partial t}U(t). \tag{6}$$

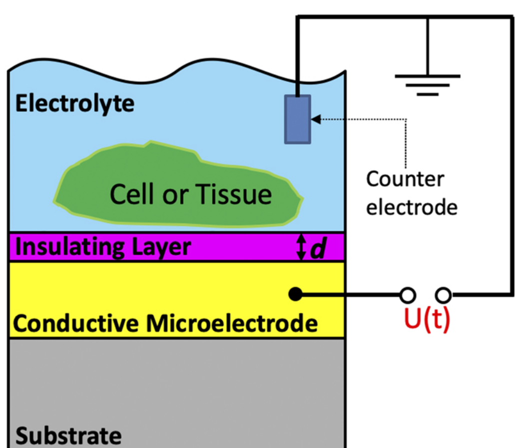

FIG. 1. Schematic experimental setup for extracellular electrical stimulation of electrogenic cells or tissue with a conductive microelectrode coated with an insulating layer of thickness d (parallel-plate configuration) to prevent Faradaic processes at the electrode–electrolyte interface.

© Author(s) 2021

Thus, previous attempts to enhance the CIC of capacitive microelectrodes were based on the approach to increase the specific capacitance of the dielectric layer.

We now consider a material with ferroelectric properties. Ferroelectrics are characterized by the existence of a (spontaneous) ferroelectric polarization $\mathbf{P}^{(\mathrm{FE})}$, which can be reoriented by an applied electric field, i.e., $\mathbf{P}^{(\mathrm{FE})} = \mathbf{P}^{(\mathrm{FE})}(\mathbf{E})$.[23] The finite value of the ferroelectric polarization at zero electric field is called the remanent polarization P_r. By applying an electric field above the coercive field E_C of the ferroelectric, the remanent polarization can be switched between the bistable states $\pm P_\mathrm{r}$, which is the basis for nonvolatile ferroelectric memory applications.[24] Here, the discovery of ferroelectricity in HfO_2-based thin films represents a real breakthrough due to the full CMOS compatibility of this material class and outstanding ferroelectric properties at the nanoscale.[24–26] Moreover, conventional dielectric HfO_2 layers have been previously utilized in capacitive biochips,[17,18,20] which demonstrates their biocompatibility. Note that materials with ferroelectric properties also exhibit dielectric properties but not vice versa. Thus, the electrical polarization of a material with ferroelectric properties is given by $\mathbf{P} = \mathbf{P}^{(\mathrm{DE})} + \mathbf{P}^{(\mathrm{FE})}$. As a consequence, it follows from Eq. (1) that

$$\mathbf{D}(\mathbf{E}) = \varepsilon_0 \varepsilon_r \mathbf{E} + \mathbf{P}^{(\mathrm{FE})}(\mathbf{E}), \tag{7}$$

and the resulting ferroelectric displacement current density for extracellular stimulation J_stim in response to a time-varying electric field $E(t) = U(t)/d$ is then given by

$$J_\mathrm{stim} = C_s \frac{\partial}{\partial t} U(t) + \frac{\partial}{\partial t} P^{(\mathrm{FE})}(U(t)), \tag{8}$$

which exhibits the ferroelectric polarization current $\partial P^{(\mathrm{FE})}/\partial t$ as an additional contribution as compared to the purely capacitive stimulation current density [Eq. (6)].

Depending on the applied electric field strength $E(t) = U(t)/d$, we can identify two different regimes of the ferroelectric polarization current that are separated by the coercive field E_C of the ferroelectric, i.e.,

$$\frac{\partial}{\partial t} P^{(\mathrm{FE})}(E(t)) \equiv \begin{cases} J^{(\mathrm{SSW})}(t), & E < E_\mathrm{C} \\ J^{(\mathrm{SW})}(t), & E > E_\mathrm{C}, \end{cases} \tag{9}$$

where $J^{(\mathrm{SSW})}(t)$ corresponds to the subswitching regime and $J^{(\mathrm{SW})}(t)$ corresponds to the switching regime of the ferroelectric. For subswitching fields above a specific threshold field E_T, the linear approximation equation (4) is no longer valid for a ferroelectric material due to the irreversible motion of ferroelectric domain walls, which results in a nonlinear P vs E relationship described by the Rayleigh law.[27] As a consequence, the ferroelectric displacement current density equation (8) in response to a harmonic ac electric field can contain higher harmonics due to the contribution from irreversible domain wall motion contained in $J^{(\mathrm{SSW})}(t)$,[28] which might be interesting for extracellular stimulation with low-frequency sinusoidal voltage signals.[29] Experimentally, the subswitching regime of a ferroelectric can be analyzed in detail by impedance spectroscopy and equivalent-circuit fitting with the recently introduced domain wall pinning element Z_DW.[30]

In the following, we will focus our discussion on the ferroelectric switching regime $E > E_\mathrm{C}$. The corresponding switching dynamics are a very complex problem, and there exist several models to explain the time-dependence of ferroelectric polarization reversal.[31] The traditional approach for explaining the switching dynamics is using the Kolmogorov–Avrami–Ishibashi (KAI) model,[32–34] which is based on the classical statistical theory of nucleation and predicts the relationship for the time-dependent change in ferroelectric polarization $\Delta P^{(\mathrm{FE})}(t)$ during switching between the bistable states $\pm P_\mathrm{r}$,[31]

$$\Delta P^{(\mathrm{FE})}(t) = 2P_\mathrm{r}\{1 - \exp[-(t/t_0)^n]\}, \tag{10}$$

with n being the effective dimension and the characteristic switching time t_0 as free parameters. For thin films, the effective dimension is $n = 2$,[31] and the time-dependence of the magnitude of the corresponding switching current density $J^{(\mathrm{SW})}(t)$ is then given by

$$|J^{(\mathrm{SW})}(t)| = 4P_\mathrm{r}(t/t_0^2)\exp[-(t/t_0)^2]. \tag{11}$$

We now reconsider the schematic experimental setup for extracellular stimulation depicted in Fig. 1 with the specification that the conductive microelectrode with radius r and geometrical surface area $A = \pi r^2$ is insulated with a ferroelectric layer, which corresponds to the electrolyte–ferroelectric–conductor (EFC) configuration shown in Fig. 2(a). To analyze the CIC and the time-dependence of the stimulation current density provided by the EFC configuration in the switching regime $J_\mathrm{stim}^\mathrm{EFC}(t)$, we describe the EFC configuration by the equivalent-circuit depicted in Fig. 2(b). Here, the Ohmic resistance models the electrolyte and the electrodes, and the capacitance $C = \varepsilon_0 \varepsilon_r A/d$ in combination with the KAI-model models the ferroelectric layer of the EFC configuration. The Ohmic resistance

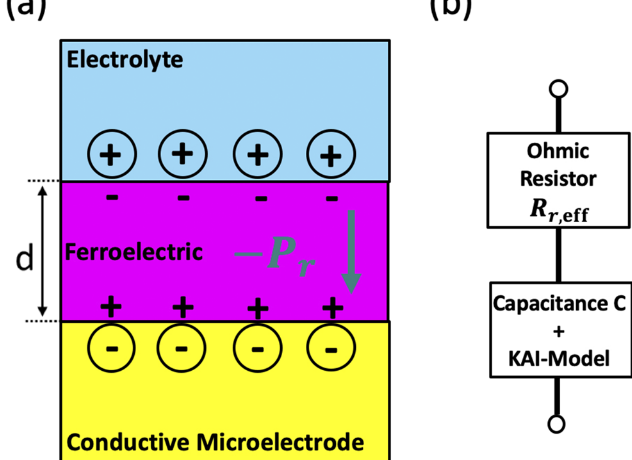

FIG. 2. (a) Electrolyte–ferroelectric–conductor (EFC) configuration in the polarization state $-P_\mathrm{r}$. In equilibrium, free charges in the electrolyte and in the conductive microelectrode screen the bound polarization charges at the surface of the ferroelectric. (b) The equivalent circuit model of the EFC configuration, which consists of an Ohmic resistor to model the resistance of the electrolyte and the electrodes and a capacitance in combination with the KAI model, which represents the ferroelectric layer.

© Author(s) 2021

can be approximated by the effective resistance $R_{r,\text{eff}}$ for a circular microelectrode with radius r and an adjacent electrolyte with specific resistance ρ according to Ref. 35,

$$R_{r,\text{eff}} = \frac{\rho}{\pi r}. \quad (12)$$

The stimulation current density $J^{\text{EFC}}_{\text{stim}}(t)$ provided by the EFC configuration (cf. Fig. 2) in response to an applied voltage pulse with height U_0, which induces polarization reversal from the initial state $-P_r$ to the final state $+P_r$, is then given by

$$J^{\text{EFC}}_{\text{stim}}(t) = \frac{U_0}{r\rho} \exp\left[\frac{-t}{R_{\text{r,eff}}C}\right] + 4P_r(t/t_0^2)\exp[-(t/t_0)^2], \quad (13)$$

where the first term in Eq. (13) is the capacitive transient $J^{(C)}(t)$. Note that ferroelectric polarization reversal in the EFC configuration has been demonstrated for various ferroelectric materials.[36–38] Moreover, it has been shown in Ref. 36 that the screening charge density at the electrolyte–ferroelectric interface (Helmholtz plane) is equivalent to the remanent polarization P_r of the ferroelectric measured in a conventional metal–ferroelectric–metal (MFM) configuration. This allows one to utilize values of P_r obtained from measurements on MFM-capacitors to calculate properties of EFC-microelectrodes. Nonetheless, we note that the switching dynamics might be not necessarily equal for a ferroelectric in EFC and MFM configurations, which should be kept in mind.

To simulate the extracellular stimulation current response of an insulated microelectrode in the EFC configuration (cf. Fig. 2) during polarization reversal, we utilize Eq. (13) with the specifications summarized in Table I. The applied voltage pulse with height $U_0 = 1$ V depicted in Fig. 3(a) generates an electric field above the coercive field of the ferroelectric layer (cf. Table I), and the resulting current response $J^{\text{EFC}}_{\text{stim}}(t)$ in the switching regime is shown in Fig. 3(b). Here, the capacitive transient $J^{(C)}(t)$ is superimposed by the bell-shaped switching current density $J^{(SW)}(t)$, and the resulting CIC for complete switching during the stimulation time (i.e., $T_{\text{stim}} > t_0$) can be calculated according to Eq. (3), which can be specified for an insulating ferroelectric material, resulting in (Ref. 27)

$$\text{CIC} = C_s U_0 + 2P_r. \quad (14)$$

We observe from Eq. (14) that the CIC of ferroelectric microelectrodes exhibits the additional contribution $2P_r$ compared to the CIC of microelectrodes with a dielectric coating for extracellular capacitive stimulation.[14] The additional contribution originates from the

TABLE I. Specifications to simulate the extracellular stimulation current response equation (13) of an insulated microelectrode (50 μm in diameter) in the EFC configuration (cf. Fig. 2) in the switching regime. The listed ferroelectric material properties correspond to a 9.5-nm-thick $Hf_{0.5}Zr_{0.5}O_2$ layer.[25] The resistivity ρ of the electrolyte corresponds to the value of phosphate-buffered saline at room temperature.[11]

d (nm)	P_r (μC/cm^2)	E_C (MV/cm)	t_0 (μs)	ε_r	r (μm)	ρ (Ω cm)	U_0 (V)
9.5	16	1	10	40	25	66.7	1

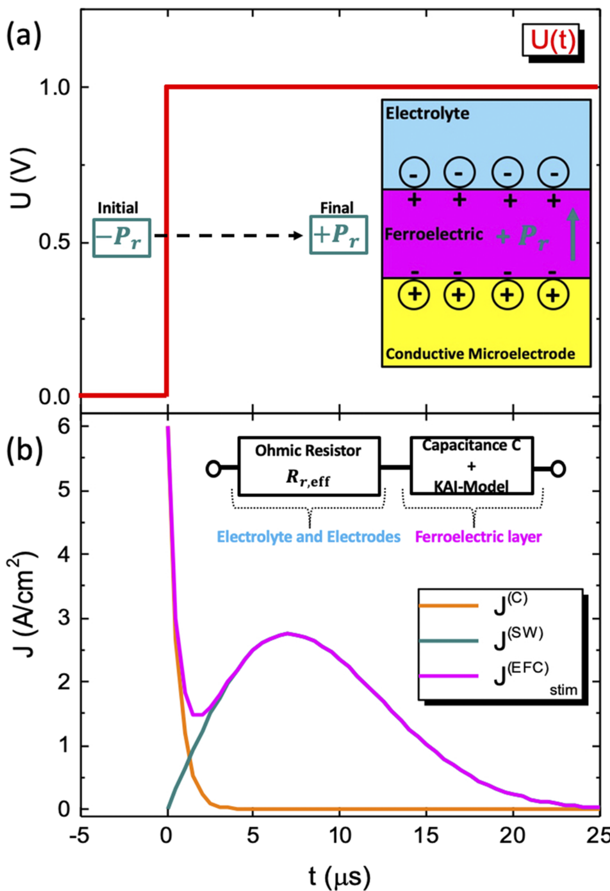

FIG. 3. (a) Voltage pulse with height $U_0 = 1$ V applied to the EFC configuration (cf. inset and Fig. 2) to switch the remanent polarization from the initial state $-P_r$ to the final state $+P_r$. (b) Simulated extracellular current response during polarization reversal of the EFC configuration according to Eq. (13) with the specifications summarized in Table I.

ferroelectric polarization, which is the foundation for the occurrence of the ferroelectric hysteresis loop, i.e., the nonlinear and hysteretic relationship of D vs E.[39] To illustrate this further, Fig. 4 shows the ferroelectric hysteresis loop D vs E of the EFC configuration (cf. Fig. 3), simulated with the model described in Ref. 40, by taking the ferroelectric properties summarized in Table I as model parameters. Here, the initial displacement field D_{init} corresponds to the polarization state $-P_r$. By applying a voltage pulse with height $U_0 = 1$ V, the ferroelectric reaches the maximum displacement field D_{max} at $E = U_0/d$. At zero field, i.e., after the voltage pulse, the ferroelectric remains in the final state $+P_r$. As a consequence, repetitive stimulation with a CIC according to Eq. (14) requires a subsequent voltage pulse of opposite polarity to reorient the remanent polarization P_r back to its initial state. This is not necessary for antiferroelectric materials or ferroelectrics in the paraelectric phase, where the remanent polarization is zero and which might be interesting alternatives for stimulation with solely unipolar voltage signals.

For a ferroelectric microelectrode with the specifications listed in Table I, Eq. (14) yields a CIC of 35.7 μC/cm^2, which is

© Author(s) 2021

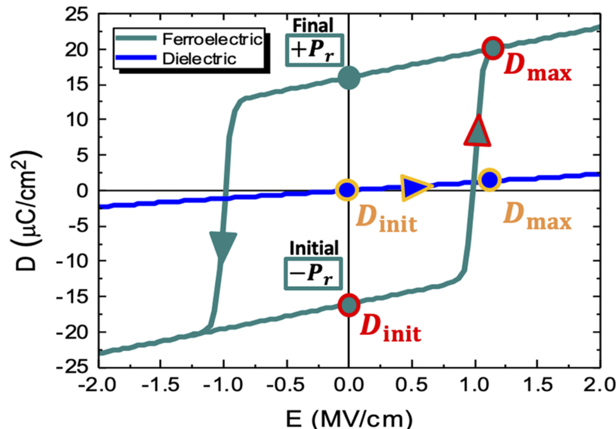

FIG. 4. Simulated ferroelectric hysteresis loop D vs E for the EFC configuration (cf. Fig. 3 and Table I). By applying a voltage pulse with height $U_0 = 1$ V, the ferroelectric reaches the maximum displacement field D_{max} at $E = U_0/d$. At zero field, the ferroelectric remains in the final state $+P_r$. For comparison, the linear D vs E relationship equation (5) for a dielectric coating of the same thickness and with $\varepsilon_r = 13$, e.g., dielectric HfO_2,[17,18] is also shown.

dominated by the contribution of $2P_r$ (see also Eq. (3) and Fig. 4). Therefore, another interesting CMOS compatible material class is $Al_{1-x}Sc_xN$, which exhibits ferroelectric properties with P_r up to 110 $\mu C/cm^2$,[41] resulting in a CIC above 200 $\mu C/cm^2$, which is in the range of previously reported stimulation-thresholds for small conductive microelectrodes (30 μm in diameter)[21] and which is approximately two orders of magnitude above the CIC of state-of-the-art capacitive microelectrodes.[16–20] Note that the CIC of ferroelectric microelectrodes might be further increased by the fabrication of 3D structures.[24] Furthermore, ferroelectric microelectrodes can also be useful in the emerging field of flexible organic bioelectronics[42] by utilizing the material class of ferroelectric polymers[43] as insulating electrode coatings.

In conclusion, our results pave the way for utilizing ferroelectrics for bioelectronic interfacing of electrogenic cells or tissue. The resulting ferroelectric–neural interface is a promising approach for extracellular electrical stimulation without toxic electrochemical effects, which is crucial for implantable neuroprosthetic devices such as retinal-implants or brain-machine interfaces. Clearly, substantial future work is needed to develop stimulus protocols for specific neuronal classes and for different ferroelectric materials with different remanent polarization and switching dynamics. Note in this context that the occurrence of a voltage drop in a ferroelectric capacitor has been recently observed, which can be explained by retarded nucleation of ferroelectric domains caused by charge inflow.[44] This observation could be interesting for electrical stimulation with (constant) current pulses instead of voltage pulses. Additional possibilities for future studies on ferroelectric–neural interfaces are extracellular electrical recordings by utilizing the ferroelectric layer as the gate oxide of a ferroelectric field-effect transistor (FeFET), whose polarization state is sensitive to extracellular potentials generated by adjacent neurons. This might result in the coupling of artificial neurons based on FeFETs[45] with biological neurons for future neuromorphic computing applications.

The author thanks Claus Burkhardt and Dieter Koelle for very fruitful discussions. This work received financial support from the State Ministry of Baden-Wuerttemberg for Economic Affairs, Labour and Tourism.

DATA AVAILABILITY

The data that support the findings of this study are available within the article.

REFERENCES

[1] S. F. Cogan, "Neural stimulation and recording electrodes," Annu. Rev. Biomed. Eng. **10**, 275 (2008).

[2] A. Kral, M. F. Dorman, and B. S. Wilson, "Neuronal development of hearing and language: Cochlear implants and critical periods," Annu. Rev. Neurosci. **42**, 47 (2019).

[3] E. Zrenner, K. U. Bartz-Schmidt, H. Benav, D. Besch, A. Bruckmann, V.-P. Gabel, F. Gekeler, U. Greppmaier, A. Harscher, S. Kibbel, J. Koch, A. Kusnyerik, T. Peters, K. Stingl, H. Sachs, A. Stett, P. Szurman, B. Wilhelm, and R. Wilke, "Subretinal electronic chips allow blind patients to read letters and combine them to words," Proc. R. Soc. B **278**, 1489 (2011).

[4] K. Mathieson, J. Loudin, G. Goetz, P. Huie, L. Wang, T. I. Kamins, L. Galambos, R. Smith, J. S. Harris, A. Sher, and D. Palanker, "Photovoltaic retinal prosthesis with high pixel density," Nat. Photonics **6**, 391 (2012).

[5] L. Yue, V. Wuyyuru, A. Gonzalez-Calle, J. D. Dorn, and M. S. Humayun, "Retina–electrode interface properties and vision restoration by two generations of retinal prostheses in one patient—one in each eye," J. Neural Eng. **17**, 026020 (2020).

[6] S. Miocinovic, S. Somayajula, S. Chitnis, and J. L. Vitek, "History, applications, and mechanisms of deep brain stimulation," JAMA Neurol. **70**, 163 (2013).

[7] E. Musk and Neuralink, "An integrated brain-machine interface platform with thousands of channels," J. Med. Internet Res. **21**, e16194 (2019).

[8] A. Stett, U. Egert, E. Guenther, F. Hofmann, T. Meyer, W. Nisch, and H. Haemmerle, "Biological application of microelectrode arrays in drug discovery and basic research," Anal. Bioanal. Chem. **377**, 486 (2003).

[9] U. Frey, U. Egert, F. Heer, S. Hafizovic, and A. Hierlemann, "Microelectronic system for high-resolution mapping of extracellular electric fields applied to brain slices," Biosens. Bioelectron. **24**, 2191 (2009).

[10] R. Samba, T. Herrmann, and G. Zeck, "PEDOT–CNT coated electrodes stimulate retinal neurons at low voltage amplitudes and low charge densities," J. Neural Eng. **12**, 016014 (2015).

[11] J. Haas, R. Rudorf, M. Becker, R. Daschner, A. Drzyzga, C. Burkhardt, and A. Stett, "Sputtered iridium oxide as electrode material for subretinal stimulation," Sens. Mater. **32**, 2903 (2020).

[12] J. Maeng, B. Chakraborty, N. Geramifard, T. Kang, R. T. Rihani, A. Joshi-Imre, and S. F. Cogan, "High-charge-capacity sputtered iridium oxide neural stimulation electrodes deposited using water vapor as a reactive plasma constituent," J. Biomed. Mater. Res., Part B **108**, 880 (2019).

[13] D. R. Merrill, M. Bikson, and J. G. R. Jefferys, "Electrical stimulation of excitable tissue: Design of efficacious and safe protocols," J. Neurosci. Methods **141**, 171 (2005).

[14] P. Fromherz and A. Stett, "Silicon-neuron junction: Capacitive stimulation of an individual neuron on a silicon chip," Phys. Rev. Lett. **75**, 1670 (1995).

[15] P. Fromherz, A. Offenhäusser, T. Vetter, and J. Weis, "A neuron-silicon junction: A retzius cell of the leech on an insulated-gate field-effect transistor," Science **252**, 1290 (1991).

[16] G. Bertotti, D. Velychko, N. Dodel, S. Keil, D. Wolansky, B. Tillak, M. Schreiter, A. Grall, P. Jesinger, S. Röhler, M. Eickenscheidt, A. Stett, A. Möller, K.-H. Boven, G. Zeck, and R. Thewes, "A CMOS-based sensor array for in-vitro neural tissue interfacing with 4225 recording sites and 1024 stimulation sites," in *2014 IEEE Biomedical Circuits and Systems Conference (BioCAS) Proceedings* (IEEE, 2014).

[17] F. Wallrapp and P. Fromherz, "TiO_2 and HfO_2 in electrolyte-oxide-silicon configuration for applications in bioelectronics," J. Appl. Phys. **99**, 114103 (2006).

© Author(s) 2021

[18] I. Schoen and P. Fromherz, "The mechanism of extracellular stimulation of nerve cells on an electrolyte-oxide-semiconductor capacitor," Biophys. J. **92**, 1096 (2007).
[19] M. Eickenscheidt, M. Jenkner, R. Thewes, P. Fromherz, and G. Zeck, "Electrical stimulation of retinal neurons in epiretinal and subretinal configuration using a multicapacitor array," J. Neurophysiol. **107**, 2742 (2012).
[20] M. Dollt, M. Reh, M. Metzger, G. Heusel, M. Kriebel, V. Bucher, and G. Zeck, "Low-temperature atomic layer deposited oxide on titanium nitride electrodes enables culture and physiological recording of electrogenic cells," Front. Neurosci. **14**, 552876 (2020).
[21] A. Corna, T. Herrmann, and G. Zeck, "Electrode-size dependent thresholds in subretinal neuroprosthetic stimulation," J. Neural Eng. **15**, 045003 (2018).
[22] S. Brandt and H. D. Dahmen, *Elektrodynamik*, 4th ed. (Springer, Berlin, 2005).
[23] *Polar Oxides*, 1st ed., edited by R. Waser, U. Böttger, and S. Tiedke (Wiley, New York, 2005).
[24] M. H. Park, Y. H. Lee, T. Mikolajick, U. Schroeder, and C. S. Hwang, "Review and perspective on ferroelectric HfO_2-based thin films for memory applications," MRS Commun. **8**, 795 (2018).
[25] J. Müller, T. S. Böscke, D. Bräuhaus, U. Schröder, U. Böttger, J. Sundqvist, P. Kücher, T. Mikolajick, and L. Frey, "Ferroelectric $Zr_{0.5}Hf_{0.5}O_2$ thin films for nonvolatile memory applications," Appl. Phys. Lett. **99**, 112901 (2011).
[26] Y. Wei, P. Nukala, M. Salverda, S. Matzen, H. J. Zhao, J. Momand, A. S. Everhardt, G. Agnus, G. R. Blake, P. Lecoeur, B. J. Kooi, J. Íñiguez, B. Dkhil, and B. Noheda, "A rhombohedral ferroelectric phase in epitaxially strained $Hf_{0.5}Zr_{0.5}O_2$ thin films," Nat. Mater. **17**, 1095 (2018).
[27] D. Damjanovic, "Ferroelectric, dielectric and piezoelectric properties of ferroelectric thin films and ceramics," Rep. Prog. Phys. **61**, 1267 (1998).
[28] S. Miga, J. Dec, and W. Kleemann, "Computer-controlled susceptometer for investigating the linear and nonlinear dielectric response," Rev. Sci. Instrum. **78**, 033902 (2007).
[29] D. K. Freeman, D. K. Eddington, J. F. Rizzo III, and S. I. Fried, "Selective activation of neuronal targets with sinusoidal electric stimulation," J. Neurophysiol. **104**, 2778 (2010).
[30] M. Becker, C. J. Burkhardt, B. Schröppel, R. Kleiner, and D. Koelle, "Rayleigh analysis and dielectric dispersion in polycrystalline $0.5(Ba_{0.7}Ca_{0.3})TiO_3$–$0.5Ba(Zr_{0.2}Ti_{0.8})O_3$ ferroelectric thin films by domain-wall pinning element modeling," J. Appl. Phys. **128**, 154103 (2020).
[31] J. Y. Jo, H. S. Han, J.-G. Yoon, T. K. Song, S.-H. Kim, and T. W. Noh, "Domain switching kinetics in disordered ferroelectric thin films," Phys. Rev. Lett. **99**, 267602 (2007).
[32] A. N. Kolmogorov, "On the statistical theory of the crystallization of metals," Bull. Acad. Sci. USSR Math. Ser. **3**, 355 (1937), https://scholar.google.com/scholar?cluster=14462095218264478213 & hl=en & as_sdt=2005 & sciodt=0,5.
[33] M. Avrami, "Kinetics of phase change. I General theory," J. Chem. Phys. **7**, 1103 (1939).
[34] Y. Ishibashi and Y. Takagi, "Note on ferroelectric domain switching," J. Phys. Soc. Jpn. **31**, 506 (1971).
[35] Z. Chen, L. Ryzhik, and D. Palanker, "Current distribution on capacitive electrode-electrolyte interfaces," Phys. Rev. Appl. **13**, 014004 (2020).
[36] R. J. Ferris, S. Lin, M. Therezien, B. B. Yellen, and S. Zauscher, "Electric double layer formed by polarized ferroelectric thin films," ACS Appl. Mater. Interfaces **5**, 2610 (2013).
[37] S. Fabiano, X. Crispin, and M. Berggren, "Ferroelectric polarization induces electric double layer bistability in electrolyte-gated field-effect transistors," ACS Appl. Mater. Interfaces **6**, 438 (2014).
[38] H. Toss, S. Lönnqvist, D. Nilsson, A. Sawatdee, J. Nissa, S. Fabiano, M. Berggren, G. Kratz, and D. T. Simon, "Ferroelectric surfaces for cell release," Synth. Met. **228**, 99 (2017).
[39] H. Yan, F. Inam, G. Viola, H. Ning, H. Zhang, Q. Jiang, T. Zeng, Z. Gao, and M. J. Reece, "The contribution of electrical conductivity, dielectric permittivity and domain switching in ferroelectric hysteresis loops," J. Adv. Dielectr. **01**, 107 (2011).
[40] S. L. Miller, J. R. Schwank, R. D. Nasby, and M. S. Rodgers, "Modeling ferroelectric capacitor switching with asymmetric nonperiodic input signals and arbitrary initial conditions," J. Appl. Phys. **70**, 2849 (1991).
[41] S. Fichtner, N. Wolff, F. Lofink, L. Kienle, and B. Wagner, "AlScN: A III–V semiconductor based ferroelectric," J. Appl. Phys. **125**, 114103 (2019).
[42] T. Someya, Z. Bao, and G. G. Malliaras, "The rise of plastic bioelectronics," Nature **540**, 379 (2016).
[43] H. Li, R. Wang, S.-T. Han, and Y. Zhou, "Ferroelectric polymers for non-volatile memory devices: A review," Polym. Int. **69**, 533 (2020).
[44] Y. J. Kim, H. W. Park, S. D. Hyun, H. J. Kim, K. D. Kim, Y. H. Lee, T. Moon, Y. B. Lee, M. H. Park, and C. S. Hwang, "Voltage drop in a ferroelectric single layer capacitor by retarded domain nucleation," Nano Lett. **17**, 7796 (2017).
[45] H. Mulaosmanovic, E. Chicca, M. Bertele, T. Mikolajick, and S. Slesazeck, "Mimicking biological neurons with a nanoscale ferroelectric transistor," Nanoscale **10**, 21755 (2018).

© Author(s) 2021